ABSTRACT

Title of dissertation: UNDERSTANDING THE CHAOTIC SADDLE WITH FOCUS ON A 9-VARIABLE MODEL OF PLANAR COUETTE FLOW

Joseph D. Skufca, Doctor of Philosophy, 2005

Dissertation directed by: Distinguished University Professor James A. Yorke
Department of Mathematics and Physics

We study the transition between laminar and turbulent states in a Galerkin representation of a parallel shear flow, where a stable laminar flow and a transient turbulent flow state coexist. We find trajectories on the chaotic saddle in a model of plane Couette flow, and then use those trajectories to calculate the spectrum of Lyapunov exponents and the dimension of the system. We are able to estimate the fractal dimension of the both the saddle set and its stable manifolds. At moderate values of Reynolds number, these dimension estimates indicate that the stable set is nearly dense in many regions of phase. We find that the regions of initial conditions where the transient lifetimes show strong heterogeneity and appear sensitively dependendent on the initial conditions are separated from the regions with a smooth variation of lifetimes by an previously undescribed invariant structure, which we call the edge of chaos. We describe a technique to identify and follow the edge of chaos and provide evidence that it is a smooth manifold. For some values of Reynolds numbers we find that the edge of chaos coincides with the stable manifold of a periodic orbit, whereas in other ranges of the parameter, the edge is the stable set of a higher-dimensional chaotic object. We provide evidence that this invariant edge structure may be a typical attribute of high dimensional transient chaos.

UNDERSTANDING A CHAOTIC SADDLE WITH FOCUS ON A 9-VARIABLE MODEL OF PLANAR COUETTE FLOW

by

Joseph D. Skufca

Dissertation submitted to the Faculty of the Graduate School of the
University of Maryland, College Park in partial fulfillment
of the requirements for the degree of
Doctor of Philosophy
2005

Advisory Commmittee:

Professor James Yorke, Chair/Advisor
Dr. Bruno Eckhardt
Professor Brian Hunt
Professor Edward Ott
Professor Kenneth Berg

ACKNOWLEDGMENTS

Although my name is listed as the author of this work, it is clear to me that there were many people who have contributed to its completion. I take this opportunity to recognize some of those who have provided the most significant assistance.

My biggest debt of gratitude is owed to my wife, Susan. My work on this dissertation shifted a significant load to her shoulders as we continue to raise four beautiful children. Despite her burdens, I received only encouragement from her. I owe her much.

My children were very patient in allowing me to play "student" during the many times that I should have been playing "Daddy." I never heard one complaint. I want them to know that I appreciate their sacrifices. My son Joey deserves special recognition, as he spent many hours providing "Help Desk" services — loading software, keeping the computers running, installing, upgrading, troubleshooting, and more.

I would like to thank my advisor, Professor James Yorke. Whenever I would come to his office for a meeting, he was always happy and enthusiastic, with genuine excitement about what we were doing. Each visit served to reinvigorate me as we marched down this long struggle. In addition to his teaching me about being a mathematician and a researcher, he provided a great example of true mentorship. I will forever be grateful for this opportunity to work with him.

During the final year of my research, Professor Bruno Eckhardt was a continuous participant in my discussions with my advisor. In research, he treated me as a true collaborator, and I thank him for that respect. But in a personal sense, he treated me as if I were one of *his* students; with a tone of care, concern, and gentle prodding, he was often asking about my dissertation. I have benefited greatly from the interaction.

The faculty at the University of Maryland works well as a team, and my advisor was able to call on several of his colleagues to assist in my education. Professor Helena Nusse attended

several of my meetings with my advisor, and she provided some insightful recommendations on my research. Professors Edward Ott and Brian Hunt, in addition to agreeing to serve on my thesis committee, provided key guidance on the theoretical work that I was developing.

My first steps toward pursuit of a PhD were helped by the gentle pushing of several colleagues at The United States Naval Academy. Professor Mark Meyerson and Commander Ray Putt facilitated my entry into the program. Additionally, Professors Bob Artigiani and Reza Malek-Madani have served as my mentors since my days as a midshipman and have provided some very key enthusiasm to this overall project.

Professor Erik Bollt has been a great friend and advisor during my entire post-graduate education. We spent many hours on the phone, with him listening carefully to my descriptions of what I was doing, asking great questions, and providing extremely useful feedback. I will never be able to repay the time, but I am immensely thankful for his help.

TABLE OF CONTENTS

LIST OF TABLES

LIST OF FIGURES

Chapter 1

Introduction

> *Philosophy is written in this grand book — the universe — which stands continuously open to our gaze. But the book cannot be understood unless one first learns to comprehend the language and interpret the characters in which it is written. It is written in the language of mathematics, and its characters are triangles, circles, and other geometrical figures, without which it is humanly impossible to understand a single word of it; without these one is wandering about in a dark labyrinth.*
>
> (Galileo Galilei, as quoted by Machamer in *The Cambridge Companion to Galileo.*

1.1 Background.

Osborne Reynolds, a British mathematician and scientist, was the first to identify that flow could be categorized into two broad regimes [1], which are now called "laminar" and "turbulent." His experiments in pipe-flow are considered to be seminal achievements. In addition to the purely laminar flow regime (for small fluid velocities) and fully developed turbulence (at high fluid velocities), Reynolds identified that there was an intermediate regime of non-dimensionalized velocities where the system exhibits both behaviors, with laminar flow interrupted by intermittent regions of transient turbulence. The transition from laminar flow to turbulence in parallel shear flows is still not completely understood, and characterizing this transition remains one of the significant problems in fluid dynamics [2].

Plane Couette flow describes the motion of a viscous fluid between two parallel plates (see Fig 1.1), with the plates moving relative to one another at constant velocity. It is named in honor of Maurice Frédéric Alfred Couette, a French physicist of the late 19th century, who made the first successful measurements of viscosity.

In the laminar flow condition, the fluid will have a linear velocity profile across the width

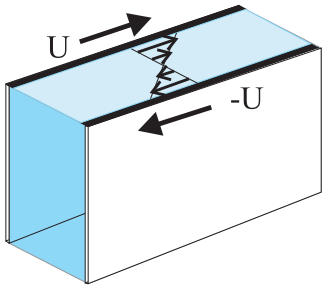

Figure 1.1: **Plane Couette channel.** Fluid is constrained by two parallel walls which move in opposite directions at constant velocity (U).

of the channel. Plane Couette flow has a transition to turbulence that is similar in character to that of pipe flow in that the transition is dominated by transient behavior. Mathematically, the two flows share a common characteristic in that the laminar flow condition remains linearly stable for all Reynolds numbers [3]. Experiments and numerics show that near onset, the turbulence is transient, sometimes persisting for a very long time and then suddenly decaying to the laminar profile [4, 5, 6, 7, 3, 8, 9]. The transients are sensitively dependent upon initial conditions, which, in experiment, may imply that the specific response to a perturbation may be "unpredictable." Some researchers have proposed that the sensitive dependence, as well as an exponential distribution of transient lifetimes, indicate the presence of a chaotic saddle (non-attracting chaotic invariant set) in the dynamics [3, 4]. The primary goal of this thesis is to apply dynamical systems analysis techniques to improve the understanding of the transition to turbulence in plane Couette flow by studying the chaotic saddle.

Because characterization of the transition boundary requires extensive numerical simulations, we chose to develop our ideas using the 9-d Galerkin projection of [10], which was derived from the 19-variable model studied in [5] by restricting the dynamics to an invariant symmetry subspace. The general structure of this and other models is that of ordinary differential equations with linear damping, quadratic coupling and a constant forcing,

$$\dot{x}_i = -\frac{d_i}{Re}x_i + \sum_{j,k} a_{i;j,k}x_j x_k + f_i. \tag{1.1}$$

Besides the Reynolds number, which controls the damping, there are two geometric parameters

determining the widths and length of the flow domain. Following [5], we take the periodic cell length to be 2π and a cell height of π, where unit length is defined as the width of the flow channel. While (1.1) provides then general structure of these models, the choice of modes and additional symmetry assumptions will generate a specific model. The equations of motions used in this study are provides as Appendix A. Although this model is too small to be considered a *simulation* of plane Couette flow, it is sufficient to capture certain qualitative aspects of the actual flow. By using this small model, we are able to perform a more detailed analysis of some of the underlying dynamical systems issues that we hope will provide insight and direction to further studies and experiments on these problems in fluid dynamics.

1.2 Structure of this Thesis — Chapters Two through Seven.

- Chapter 2 provides an overview of our primary results regarding the chaotic saddle in our model, to include measurements of the spectrum of Lyapunov exponents and the fractal dimension of the chaotic saddle. To our knowledge, these results reflect the first time such quantities have been calculated for chaotic saddles in high dimensional dynamical systems.

- Chapter 3 introduces a system characteristic that we call *the edge of chaos*, an invariant structure that separates the laminar flow region from the transient turbulence. Although a similar structure has been observed in some two dimensional systems, these structures have not previously been identified in higher dimensional systems.

- Chapter 4 provides a more thorough study of the chaotic saddle, as well as more detailed results concerning the characteristic decay time associated with the transient behavior.

- Chapter 5 provides an in depth study of the *edge*, to include a description of techniques for analysis of the *edge*. Additionally, the chapter provides supplementary material to illuminate some of the fundamental dynamical principles that lead to development of an *edge* in a system with transient chaos.

- Chapter 6 develops a new analysis tool for chaotic transients that computes the lifetime of a

chaotic transient by directly measuring that portion of the transient that is chaotic. We apply this technique to a system where the standard approach to measuring transient lifetime are simply not tractable. Additionally, we highlight how this tool may be employed to provide additional insight into systems of transient chaos.

- Chapter 7 provides a short roadmap to additional areas of related study.
- The appendix provides supplementary material, primarily proofs and longer derivations.

The chapters two through six of this thesis were written as stand-alone articles, intended for eventual publication in peer-reviewed journals. Each can be read as an independent work. Consequently, there is some repetition, especially of introductory material. We hope that a reader who digests this work cover to cover is not distracted by this necessary repetition.

1.3 The *Lifetime* function.

A standard technique in the study of transient behavior is to consider the *duration* of a transient. For an autonomous system, this duration can be treated as a scalar function of points in phase space. For each point $\boldsymbol{y}$, we consider its trajectory under the flow of the dynamical system, $\phi^t(\boldsymbol{y})$. If some characteristic of the trajectory is transient, then we can find the first time, $t = t^*$ for which $\phi^{t^*}(\boldsymbol{y})$ no longer has that characteristic, and assign $L(\boldsymbol{y}) = t^*$ as the *lifetime* of $\boldsymbol{y}$. We then use the lifetime function as a tool to explore the transient characteristics of the system.

In this dissertation, we will use two very different approaches to defining the *lifetime* function:

1. For our model of plane Couette flow, the laminar state is the only attractor that we are able to identify in the system, and every numerical trajectory asymptotically approaches the origin. One method for defining lifetime would be to place a small ball around the origin, and define the lifetime as the time it takes a trajectory to reach that ball. That method is used in both Chapters 3 and 5. In addition to being simple to describe and understand, it provides the most computationally efficient method for computing accurate lifetimes.

2. As an alternative, in Chapters 2 and 4, we elect to determine the transient lifetime based on the idea that while a trajectory is near the chaotic saddle, it shows sensitive dependence on initial conditions, and two nearby trajectories will *diverge* at an exponential rate. However, eventually, the trajectory will approach the stable origin. In some neighborhood of the origin, all nearby trajectories must *converge.* The lifetime of the chaotic transient is based on detecting this change in character. Chapter 6 contains a detailed explanation of this method. This second approach is somewhat non-standard and is slightly less efficient that the more simple approach described in item 1. However, Chapter 6 describes why this new approach is necessary for some problems. Additionally, although the technique requires slightly more computation, it can provide additional insight into the behavior of the system. In Chapters 2 and 4, we use this insight to provide a clearer description of how long transients depart the vicinity of the saddle.

Most of the results using the analysis of transient lifetime does not depend upon which of these definitions is used, and it is likely that other definitions could prove useful for other analysis approaches or other problems involving transient chaos. Section E.2 (Appendix) provides a specific list of characteristics that we believe are required qualities of a suitable lifetime function.

1.4 A Note on Numerical Accuracy

Much of the work in this thesis is based on numerical integration of ordinary differential equations. The systems under study in this thesis satisfy all the conditions necessary to infer that unique solutions exist for all forward time. Because we focus on chaotic trajectories over very long time spans, it is computationally intractable to try to establish an integration scheme that maintains a specified error tolerance over the entire integration. However, the basis of most of the work is not dependent upon highly accurate approximations to a trajectory. Rather, the qualitative behavior of the system is of primary concern. Consequently, we assume that numerical trajectories can capture the qualitative behavior of the system even if they do not reflect true trajectories.

All integration is performed using a fixed step Runge-Kutta fourth order method. In essence,

we are approximating the continuous time system (the flow of a differential equation) by a "nearby" approximation as a discrete time system. Since our finite dimensional model (a system of ODE's) is *already* a gross approximation to an infinite dimensional system (a PDE representation via the Navier-Stokes equation), the additional error associated with our numerical integration method is not significant when we limit our study to the qualitative behavior of the finite dimensional model.

Chapter 2

The chaotic saddle in a model of plane Couette flow

In plane Couette flow (PCF) of a viscous fluid, the laminar flow is linearly stable for all Reynolds numbers. However, when the laminar flow is perturbed, the flow may become turbulent for some transient period. Experiments indicate that the system response to these perturbations in sensitively dependent upon both the perturbation and the Reynolds number [8]. These experimental results, as well as direct numerical simulations, have led some researchers to propose that the transient turbulence is connected to a low dimensional chaotic saddle [3, 4]. Galerkin method has been used to provide low dimensional models of PCF to more efficiently explore parameter space [5, 11, 6, 12, 10]. In particular, Eckhardt and Mersmann [5] developed a 19-variable model to explore the fractal structure of what they believed to be a chaotic saddle. Schmiegel [10] assumed additional symmetries in that model to reduce to a 9-variable system that continued to show chaotic transients that depend sensitively on perturbation and Reynolds number.

In general, the investigation of these Galerkin models has focused on finding periodic orbits, bifurcation structures, and statistical analysis of system characteristics based on sampling. In order to refine the statistical results and develop a greater understanding of the chaotic structures, one would like to find long numerical trajectories along the chaotic saddle. Such trajectories cannot typically be discovered by sampling phase space because the saddle is too unstable. Even the longest sample trajectories are not suitable for calculating asymptotic values such as Lyapunov exponents. The *Stagger-and-Step method* [13] provides a robust tool for resolving the chaotic saddle in higher dimensional systems. Applying a slightly modified version of that algorithm to the Eckhardt/Schmiegel 9-variable model of PCF, we generate arbitrarily long numerical trajectories along the chaotic saddle of the system and resolve satisfactory approximations of the Lyapunov exponents. Applying the techniques of [14], we compute dimension values for the saddle and its stable set as a function of Reynolds number. Additionally, by using a *lifetime* function based on

finite time Lyapunov exponents, we are able to provide a more refined description of the escape path from the chaotic saddle.

In this chapter:

1. We promulgate results obtained from this 9-variable model of PCF which we believe to be the first quantifiable measures of the chaotic saddle which underlies the transient turbulence in the system [3]. We find that while the saddle itself is $\approx$ 5-dimensional, its stable set is nearly full dimension.

2. We describe the typical path through which chaotic transients depart the vicinity of the chaotic saddle. We believe this technique to have broader applicability to problems that require increased resolution of the terminal phase of chaotic transients.

We represent the Schmiegel model of PCF by

$$\dot{\boldsymbol{x}} = Q(\boldsymbol{x}; Re). \tag{2.1}$$

where the function Q is a quadratic function of $\boldsymbol{x} \in \mathbb{R}^9$. The model assumes periodic boundary conditions; following [5], we take the periodic cell length to be 2π and a cell height of π, where unit length is defined as the width of the flow channel. The origin of the system is associated with the laminar flow condition, and is stable for all Reynolds numbers [1]. Moreover, all numerical trajectories that we have computed eventually relax to the attracting laminar flow condition. Parameter space was explored by varying the Reynolds number, Re.

To each point in phase space we assign a *lifetime* $L(\boldsymbol{x})$, based on estimating when the trajectory leaves the neighborhood of the saddle and begins its approach to the attractor. Robust sampling of 9-dimensional space is not practical, but we are able to illustrate the fractal structure of the lifetime landscape by selecting points on a two dimensional subset of phase space. Fig 2.1 shows the lifetime function for $Re = 600$, plotted on three different scales. We note: (1) there is no increase in smoothness as the resolution is increased; and (2) although there are macroscopic areas

[1] The specific equations of motion are provided in Appendix A, though the appendix expresses the system using the variable y instead of the variable x.

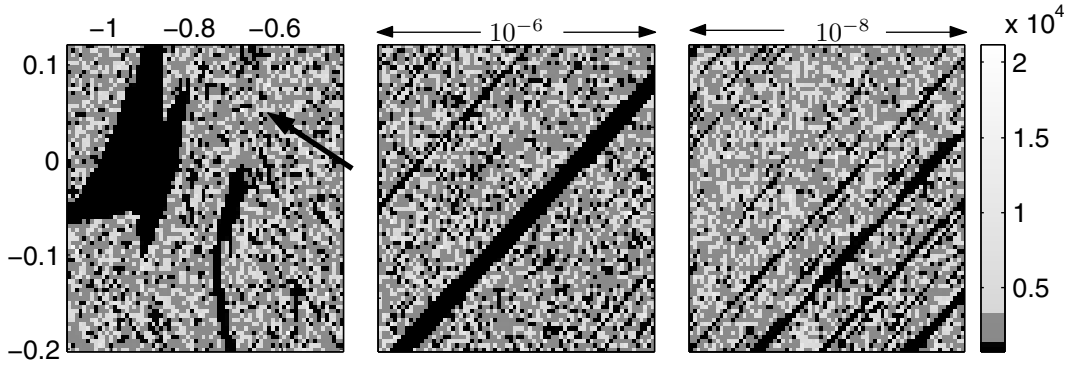

Figure 2.1: **Lifetime plots for a typical region.** Each figure shows a sampling on a $x_1 - x_2$ plane. The grids are shaded according to the lifetime of the center of each grid square, with black representing points that rapidly decay to the origin (rapid return to laminar flow). Coordinates are provided for picture 1, and show that the sample is not near the origin. The arrow indicates the center-point for the sample in Picture 2, which provides a finer resolution by considering a size 10^{-6} box. The third picture is a size 10^{-8} resampling of the lower left corner of picture 2. The three pictures all show macroscopic areas of short lifetime. The "speckled" regions, where short and long lifetimes are intermingled, indicate an intersection of the 2-dimensional sampling plane with the stable set of the chaotic saddle.

of short lifetime, the "speckled" regions indicate that there are areas of phase for which trajectories of long lifetime appear to be nearly dense.

To generate long numerical trajectories, we follow the basic approach as in [13], with minor modifications. As a brief description: a trajectory $\boldsymbol{x}(t)$ is numerically integrated as long as $L(\boldsymbol{x}(t))$ remains above some threshold value T^*. This threshold is chosen such that $\boldsymbol{x}(t)$ remains near the invariant set. When necessary, the trajectory is perturbed by some small amount δ to increase the lifetime. By requiring $\|\delta\|$ to be small, the error introduced by the perturbation can be kept smaller than the error associated with the numerical integration. The resultant *pseudo-trajectory* can be continued in this fashion to arbitrary length. A more detailed description of our precise technique is provided in Appendix B.

We focus on the range of Reynolds numbers $350 \leq Re \leq 800$. Lyapunov exponents were calculated from pseudo-trajectories of roughly 10^6 time units; the results are illustrated in Fig 2.2. For this range of Reynolds number, we note that the saddle has two unstable directions (two positive Lyapunov exponents). The third largest Lyapunov exponent is 0, which results from the system being an autonomous differential equation.

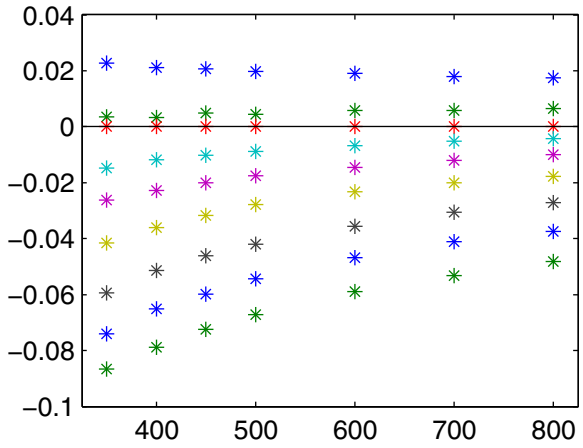

Figure 2.2: The nine Lyapunov exponents for $350 \leq Re \leq 800$. The saddle has two positive exponents for this entire parameter range, with one 0 exponent because the system is autonomous.

Decay time and fractal dimension. In [14], the authors extend the Kaplan-Yorke dimension (D_{KY}) from chaotic attractors to chaotic saddles. As in the case of attractors, the formulation is conjectured to give the information dimension of the natural measure on a typical chaotic set as a function of the Lyapunov exponents. However, for a chaotic saddle, the computation must by modified to account for the instability of the saddle. Specifically, a portion of the entropy created for trajectories near the saddle is due to instability that is transverse to the chaotic invariant set. This transverse instability is described by the *decay time* τ, defined as follows: From a large ensemble of $\{\boldsymbol{x}_i\}_1^n$ of initial conditions, let $n(t)$ be the number of points whose lifetime exceeds t; then let

$$\frac{1}{\tau} = \lim_{t\to\infty} \lim_{n(0)\to\infty} \frac{-\ln\left(n(t)/n(0)\right)}{t}. \tag{2.2}$$

Like Lyapunov exponents, this exponential decay time is considered a global characteristic of the

chaotic saddle.

The stable set of the chaotic saddle consists of those points in phase space that approach the saddle in forward time. For ease of language and notation, we call this set simply the *stable set*, and we let D_s be the fractal dimension of that set. The stable set is the physical observable, since any trajectory that starts near the stable set will have a long transient lifetime, even though it might initally be far from the actual saddle. The decay time is closely related to D_s, through the largest Lyapunov exponent, λ_1. As identified in [15], in an N dimensional system, if τ is sufficiently large, then

$$d := N - D_s = (\tau\lambda_1)^{-1}. \tag{2.3}$$

We call d the *defect* of the stable set, which varies with Reynolds number, as shown in Fig 2.3. The formulation in [15] assumes that generically, a line through phase space will have a non-empty intersection with the stable set, or equivalently, that $D_s > N - 1$. Therefore, requiring $d < 1$ implies that (2.3) should apply whenever $\lambda_1 > 1/\tau$, which (for our model) is satisfied throughout the parameter range studied.

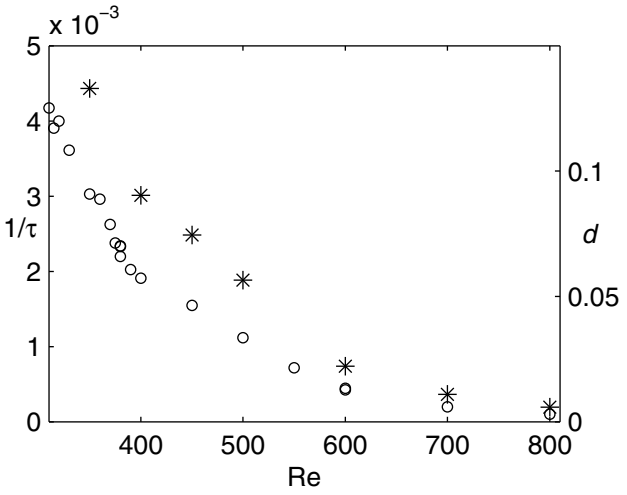

Figure 2.3: $1/\tau$ **(circles) and defect** $d := 9 - D_s$ **(asterisks) plotted as a function of Reynolds number (**Re**).** Since λ_1 is approximately constant over this parameter range, the shape of the defect curve closely matches the shape of $1/\tau$.

Applying the formulae of [14], we are able to estimate the information dimension of not only the stable set, but also the dimension of the saddle itself [2]. Fig 2.4 shows the computed dimension values as a function of Reynolds number. We note that although the saddle is "small" in relation

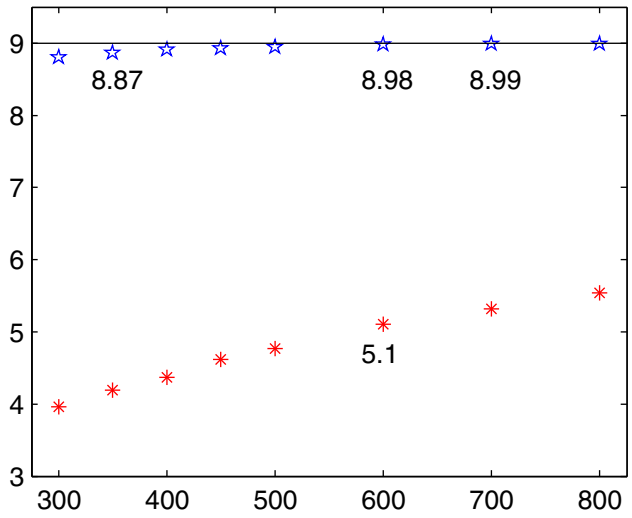

Figure 2.4: **The information dimension for the chaotic saddle (asterisks) and its stable set (stars).** The stable set becomes nearly dense as Reynolds number increases, making it "easy" to find a point near the stable set, which would result in a chaotic transient.

to 9-dimensional phase space, the stable set of the saddle becomes nearly dense as the Reynolds number grows large.

Resolving saddle escape. An important goal of our research was to develop a better understanding of how the transient turbulence dies away. For our model, the analogous goal was to describe the path through which chaotic transients departed the neighborhood of the saddle. Although all transient chaos trajectories eventually decay to the origin, we define a transition from *chaotic* to *decaying* in the following way: On the saddle, sensitive dependence implies that nearby trajectories are diverging, but near the asymptotically stable origin, phase space is *contracting* in

[2]Following [14], the dimension formulae require the full spectrum of Lyapunov exponents. For the saddle itself, the full spectrum is required. However, for the stable set, the formula from [14] can be algebraically reduced to (2.3).

all directions. Therefore, a transient trajectory would show divergence for some period of time (while near the saddle) and then convergence (as it approaches the attractor). We determine this point of transition by comparing the base trajectory with a perturbed trajectory, rescaling the perturbation as required to keep the two trajectories sufficiently close that the difference provides a good linear approximation of the local expansion. As the base trajectory leaves the neighborhood of the chaotic saddle, the perturbed trajectory will begin to converge to the base trajectory. For any initial condition, we define its lifetime as how long it takes for the trajectory to reach that point in phase space where the perturbed trajectory begins to converge to the base trajectory. The details for this technique are provided in Chapter 6.

Using this new approach to determine lifetime, we can define a set S to be all the points with positive lifetimes. More simply, outside of S, nearby trajectories are converging and decaying to the origin together. We denote the boundary of S by ∂S, and remark that ∂S will not necessarily have a simple geometric structure. Our interest was in understanding where typical chaotic transients intersect this boundary. We create an ensemble of initial conditions, $\{\boldsymbol{x}_i\}, \boldsymbol{x}_i \in \mathbb{R}^9$, which we take from a pseudo-trajectory on the saddle, so that the ensemble will reflect the natural measure on the invariant set. For each point in the ensemble, we define the point $\boldsymbol{y}_i$ to be the point in phase space where the trajectory of $\boldsymbol{x}_i$ intersects ∂S. The resultant ensemble $H = \{\boldsymbol{y}_i\}$, allows us to visualize what we call the "hole in the saddle." By definition, $H \subset \partial S$, but we have sampled only a portion of that boundary that naturally reflects the path through which typical long transients depart the neighborhood of the saddle. Fig 2.5 illustrates the presence of structure in H by plotting x_8 vs. x_7 for data computed with $Re = 390$.

Our analysis of H reveals that although there are multiple paths that support return of transients to the laminar flow condition, most trajectories follow one of just a small number of typical approaches before quickly collapsing to the origin. Although our sampling of phase space is quite sparse, it appears that trajectories leaving the neighborhood of the saddle seem to separate into disjoint sets as they relax to the stable origin. Additional study will be required to better understand the implications of this behavior. However, we expect that the technique of using this

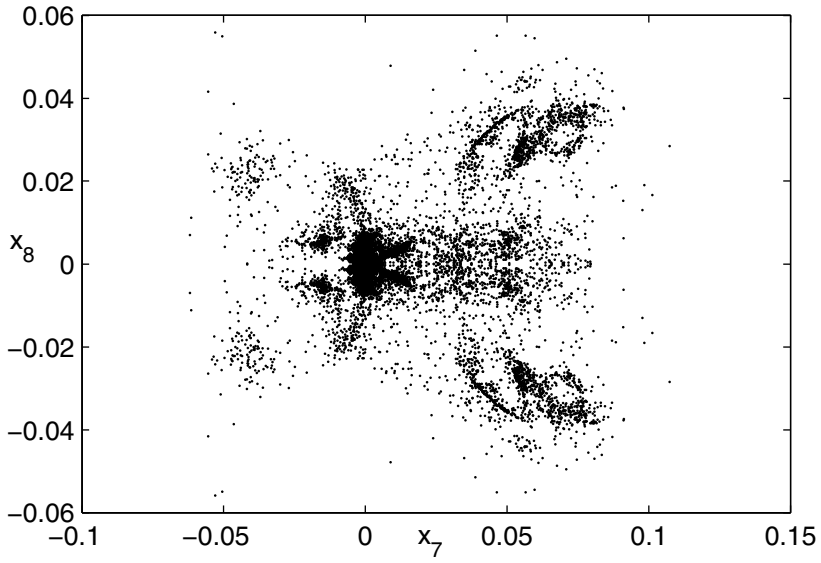

Figure 2.5: **The "hole of the saddle" for** $Re = 390$. We take an ensemble of points near the saddle, and integrate each point forward in time. While a trajectory is near the saddle, nearby trajectories diverge. However, since all transient trajectories converge to the origin, there is some "point" at which the trajectory characterization changes from *diverging* to *converging.* We collect these "points" into an ensemble H, which samples the "hole of the saddle." The figure shows a projection of H onto the $x_7 - x_8$ plane for an ensemble of about $11,000$ points. The reflection symmetry in x_8 is a global characteristic of the system

new lifetime function and analyzing the 0-lifetime set from ensembles of long-lived transients will have a broader application to other systems as we try to understand the terminal path of chaotic transients.

Chapter 3

The Edge of Chaos in a model of plane Couette flow

We study the transition between laminar and turbulent states in a Galerkin representation of a parallel shear flow, where a stable laminar flow and a transient turbulent flow state coexist. The regions of initial conditions where the lifetimes show strong heterogeneity and a sensitive dependence on initial conditions are separated from the ones with a smooth variation of lifetimes by the edge of chaos. We describe a technique to identify and follow the edge of chaos and provide evidence that it is a smooth manifold. For low Reynolds numbers we find that the edge of chaos coincides with the stable manifold of a periodic orbit, whereas at higher Reynolds numbers it is the stable set of a higher-dimensional chaotic object [1] .

In planar shear flows like plane Couette flow or pipe flow, turbulent dynamics may appear despite the linear stability of the laminar flow [1]. Experiments and numerics show that near onset, the turbulence is transient, sometimes persisting for a very long time and then suddenly decaying to the laminar profile [4, 5, 6, 7, 3, 8, 9]. The median lifetime of the transient increases rapidly with Reynolds number (Re) and may become longer than typical observation times, even at moderate Re. Both experimental and numerical evidence support an interpretation that the transients are due to a chaotic saddle [3, 4]. Several low-dimensional models, based on Galerkin method, have been used to better understand this chaotic saddle [5, 11, 6, 12, 10]. Recently, using the 9-variable model of [10], we were able to compute Lyapunov exponents and to confirm a link between lifetimes and dimension of the chaotic saddle [16, 14, 15]. In this letter, we explore the structure in phase space that separates the laminar state and the transient chaos. Previous work [5, 6, 7, 4] suggests that there is a well defined envelope to the chaos in phase space. We call this structure *the edge*

[1] This chapter has been submitted for publication in Physical Review Letters with this opening paragraph as the abstract, and may appear in that journal before publication of this thesis.

of chaos, so named because chaotic trajectories come arbitrarily close to it. Figure 3.1 provides a visualization of the edge using model data for Reynolds number (Re) of 420.

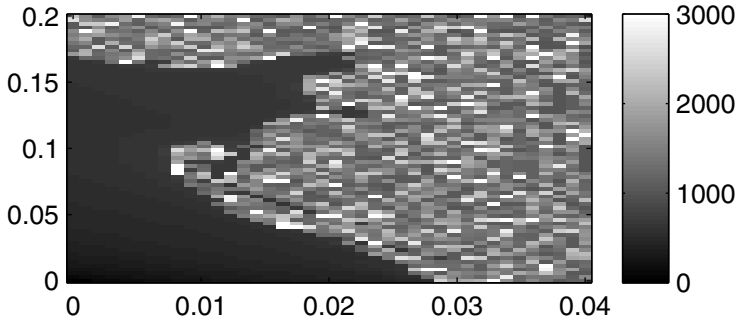

Figure 3.1: **Edge of chaos.** A 2-dimensional sample of phase space, with the laminar state at the origin. Each grid square is colored to show the transient lifetime for the trajectory with initial condition at the center of the square. The speckled region shows wildly varying transient behavior of the system and indicates that the sampled points are near the chaotic saddle. The smooth region appears to be clearly separated from the speckled, and we call that separating boundary *the edge.* Axis coordinates are magnitudes of the two randomly selected orthogonal vectors that generate the sample space.

The purpose of this letter is two-fold: (1) to outline a new technique to calculate the edge, and (2) to present evidence that *the edge is a surface,* with interesting invariant structures embedded within. For $Re < 402$, the surface coincides with the stable manifold of a symmetric pair of periodic orbits. A similar phenomena has been identified in planar maps (such as the forced damped pendulum [17]), where the "edge" [2] between basins of attraction is formed by the stable manifold of a periodic orbit. To our knowledge, such structures have not previously been identified in higher dimensional systems or systems with a single basin of attraction. Additionally, we find that as Reynolds number is increased beyond $Re \approx 402$, although the edge structure continues to exist as a saddle surface in phase space, trajectories on the edge are no longer asymptotically periodic, but chaotic. The resultant limit set of these edge trajectories is a high dimensional,

[2]These points are also known as *accessible points* or *accessible boundary points.*

fractal object embedded in the edge surface.

Because characterization of the transition boundary requires extensive numerical simulations, we chose to develop our ideas using the 9-d Galerkin projection of [10], which was derived from the 19-variable model studied in [5] by restricting the dynamics to an invariant symmetry subspace. The general structure of this class of n dimensional models is that of ordinary differential equations with linear damping, quadratic coupling and a constant forcing:

$$\dot{x}_i = -\frac{d_i}{Re} x_i + \sum_{j,k} a_{i;j,k} x_j x_k + f_i, \quad i = 1., \ldots, n. \tag{3.1}$$

Besides the Reynolds number, which controls the damping, there are two geometric parameters determining the widths and length of the flow domain. Following [5], we take the periodic cell length to be 2π and a cell height of π, where unit length is defined as the width of the flow channel. The laminar profile is a fixed point of the system. By linear change of coordinates, we translate the system to place the attracting laminar state at the origin. We denote this new system $\dot{\boldsymbol{y}} = Q(\boldsymbol{y}; Re)$, indicating that the right hand side is quadratic in $\boldsymbol{y}$ and studied over the parameter Re. The equations of motion for this system are provided in Appendix A.

The lifetime of an initial condition, denoted $L(\boldsymbol{y}_0)$, is defined as the time it takes the trajectory to come within a small distance ϵ of the laminar profile [3]. By theorems on uniqueness of solutions to differential equations, each initial condition has a unique lifetime. Points of finite lifetime are in the *laminar basin.* A point whose trajectory never approaches the laminar profile has an infinite lifetime and is said to be in the *saddle set.*

In simulations of low-dimensional models [6, 5] as well as fully resolved simulations [4, 7], the lifetime function has a consistent characteristic: As we increase the distance from the laminar profile, the lifetime function typically increases, first slowly and then very rapidly. Beyond a certain point (the *edge*), lifetime fluctuates wildly, with smaller intervals of smooth lifetimes interspersed (see Fig 3.2). This behavior can be considered as a typical "lifetime landscape" [18, 5, 6] for a

[3] Note that this definition of *lifetime* differs from the one that was used in chapter 2. We use this more simple and standard definition in this chapter because the advantages of the other lifetime function are not required for this analysis.

chaotic saddle. As illustrated in Fig 3.3, the saddle set is bounded away from the attracting origin by the edge structure.

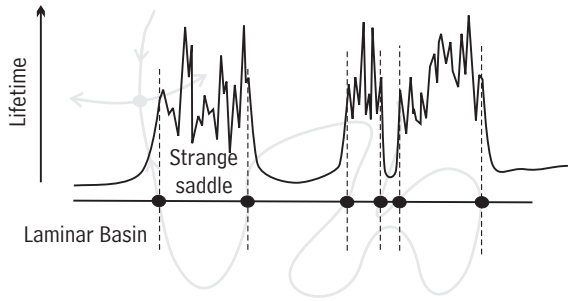

Figure 3.2: **Lifetime indicates the edge.** Lifetime $L(\boldsymbol{y})$, sampled along a line. In the laminar basin, $L(\boldsymbol{y})$ is smooth, while in the saddle region, it appears fractal. The point of separation between those behaviors is an edge point. The gray curve (extended in Fig 3.3) is drawn to illustrate that the behavior on the sampling line is related to larger structures in phase space.

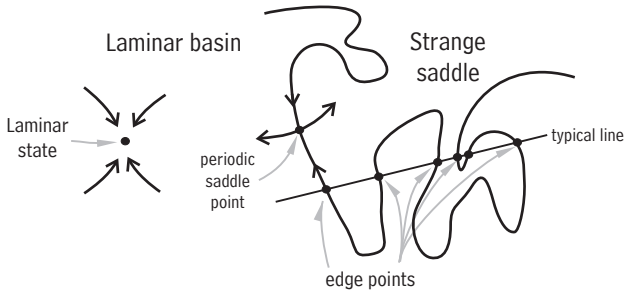

Figure 3.3: **The edge of chaos.** This cartoon schematically illustrates the *edge of chaos,* which separates the laminar basin from the strange saddle. The picture is representative of small Reynolds number, where we find that edge points lie on the 8-dimensional stable manifold of a periodic saddle orbit.

Sampling of the lifetime function is a standard approach and reveals some of the characteristic of both the saddle and the edge. From the results of [16, 15] on the dimension of the stable set of the saddle, we know that a typical line through phase space will intersect the saddle on a measure-0 Cantor set, with the lifetime diverging at each of those points. Edge points can be associated with the end-points of the "removed intervals" of the usual Cantor set construction.

Each of these "removed intervals" is a segment of points that lie in the laminar basin, yet in any neighborhood of the ends of these intervals is an uncountable infinity of points in the saddle set. For the range of Reynolds numbers considered, the Cantor set is significantly more dense than the middle-thirds construction, and the "small" [4] laminar intervals will be difficult to resolve.

The primary weaknesses of sampling are: (1) sampling will not be sufficiently dense in a high dimensional space; and (2) there are no dynamics associated with the sampled set. Whereas sampling looks at a fixed region of phase space, we can gain additional insight by considering the behavior of the edge under the flow of the differential equation. A simple continuity argument shows that the trajectory of an edge point must remain on the edge (an *edge trajectory*). By analyzing edge trajectories, we are able to observe the dynamical structure that creates the edge.

Approximation of edge trajectories. Because the edge trajectory is unstable, standard numerical integration cannot provide satisfactory approximations. Our approach provides a tractable solution to overcome this difficulty. We are confident that the technique has wider application to a broader class of problems. We outline our technique below.

If we trace along a simple path from the origin to the chaotic saddle, there must be a *first* intersection of the edge. A point on the path *before* we reach that edge point will have a trajectory whose amplitude remains "small" as it relaxes to the origin. However, a point on the path *after* we cross the edge will generate a chaotic transient, and these transients typically contain at least one large amplitude excursion before decaying. We classify an initial condition $\boldsymbol{y}$ as being either on the *high-side* or the *low-side* based on whether the maximum amplitude of its forward trajectory is above or below an appropriately chosen threshold value. To apply these ideas, we start with a low-side point (near the origin) and a high-side point (a chaotic transient). Any path that connects them must intersect the edge. By repeated bisection, we can reduce the distance between the high-low pair to accurately approximate the edge point that lies between them. This technique is significantly more efficient than trying to find the point of transition from smooth to fractal lifetimes, and it has proven very robust in numerical implementation. Figure 3.4 shows

[4] Quantitatively, the saddle set is nearly full dimension, approximately equivalent to removing only 1/10 of the remaining intervals instead of the usual 1/3.

how the bisection technique leads to increasingly accurate approximations of an edge trajectory. Because of the positive Lyapunov exponent associated with the unstable edge, a numerical initial condition will not generate the long trajectory which we require. As illustrated in Fig 3.5, we apply techniques similar to those used in the PIM-triple method [19] to generate arbitrarily long numerical approximations to the edge trajectory by successive refinement at suitable time intervals.

Structure from edge trajectories. In simple dynamical systems, such as the two or 4 coupled ODES of [20] and [12], the boundary of the laminar basin is defined by the stable manifold of a stationary point that appears in a saddle node bifurcation, and the structure in phase space is relatively simple. In higher dimensions, these flow models typically have a rich bifurcation behavior, and the boundary orbits (equivalent to the entire saddle set) are less clearly structured. However, embedded in the saddle, the invariant subset defined by the edge provides an identifiable structure, which can be resolved by examining edge trajectories.

For $Re \lesssim 402$, we find that a numerical edge trajectory converges to a periodic orbit, which we denote as p^+. Because of a reflection symmetry of the system, periodic orbits occur in pairs, and we denote the symmetry orbit as p^-. An example pair is shown in Fig 3.6. These edge periodic orbits are unstable in only one direction, creating 8-dimensional stable manifolds $W^s_{p^+}$ and $W^s_{p^-}$, which are surfaces in 9-dimensional space. As the Reynolds number is increased, the edge orbit undergoes period doubling and period halving bifurcations. At these bifurcations, the "old" periodic orbit becomes unstable in two directions, and the "new" edge orbit emerges with an 8-dimensional stable manifold. Based on computational experimentation, we conjecture that for each value of Reynolds number in this range, there is a unique periodic orbit pair with 8-dimensional stable manifold such that numerical edge trajectories converge to one or the other member of that pair, and therefore, the edge is prescribed by the union of $W^s_{p^+}$ and $W^s_{p^-}$.

Above $Re \approx 402$, edge trajectories no longer converge to a periodic orbit. At the bifurcation, when the "old" edge orbit becomes unstable in two directions, there appears to be no emergence of a "new" periodic orbit with an 8-dimensional stable manifold. We note that *throughout* the parameter range considered, the edge set (as viewed by sampling) appears to vary continuously in

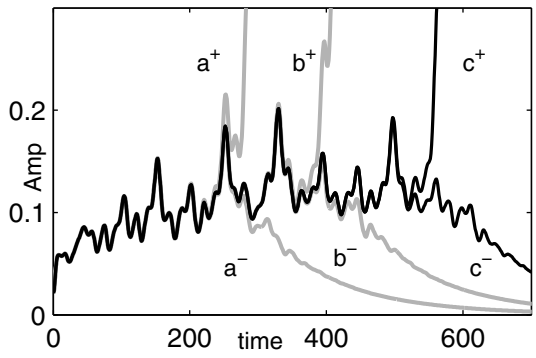

Figure 3.4: **High-side and low-side pairs.** Trajectory amplitude as a function of time plotted for three pairs of nearby initial conditions. Trajectories labeled "-" are on the *low-side,* and those with "+" on the *high-side.* The initial conditions for the "a" pair were separated by $\approx 10^{-7}$. The pairs "b" and "c" result from refining the "a" pair (using bisection) to separations of $\approx 10^{-10}$ and $\approx 10^{-13}$, respectively. The limit of the bisection algorithm (in infinite precision) would yield a trajectory that would remain bounded away from the origin, but would never achieve a large amplitude typical of chaotic transients. The data shown are for $Re = 390$.

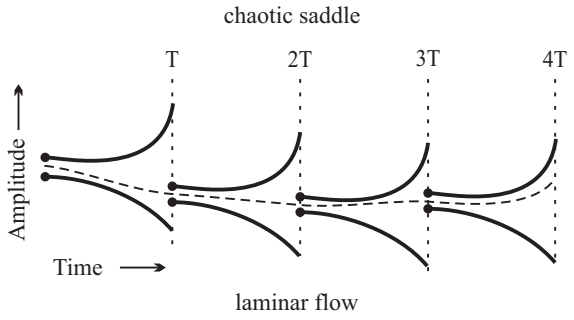

Figure 3.5: **Numerical edge trajectory.** At time 0, we start with two nearby initial conditions, one on each side of the edge. As the trajectories evolve, they are repelled from the edge, and we begin to lose precision in our approximation. At time T, before the error grows large, we use bisection to find a new pair of nearby initial conditions that are closer to the edge. By controlling refinement precision and interval T, we ensure the approximation maintains desired accuracy throughout the trajectory.

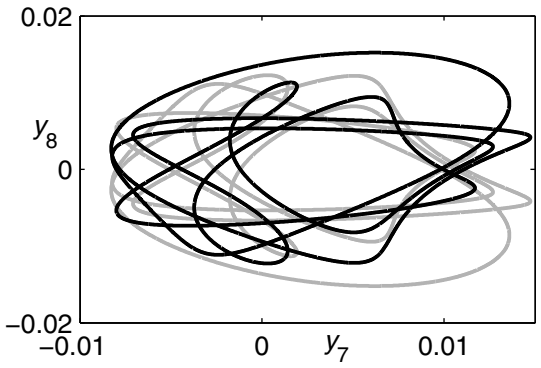

Figure 3.6: **Periodic orbit pair for** $Re = 390$, graphed by plotting the y_7 and y_8 components over one period. Edge trajectories will asymptotically approach either the black or the gray orbit.

phase space with changes in the parameter, despite any bifurcations. The invariant saddle object that persists appears to be the union of surfaces that are smooth deformations of the manifolds W^s_{p+} and W^s_{p-} which existed before the bifurcation. In this parameter range, edge trajectories are numerically chaotic, with two positive Lyapunov exponents. We conjecture that the leading Lyapunov exponent is transverse to the edge, while the second positive exponent can be associated with the observed chaos on the edge. Edge trajectories converge to a more complicated invariant set which we call a *relative chaotic attractor* because it attracts nearby edge trajectories, while the edge itself remains unstable. Figure 3.7 illustrates that edge trajectories approach some higher dimensional object instead of being asymptotically periodic.

Between the folds of the envelope. For all Reynolds numbers considered, the edge appears to be an 8-dimensional surface. Because this surface could separate phase space, a reasonable question, then, is: "How do chaotic transient return to the origin?" In answer, we provide the following observations: The edge is composed of two symmetric parts which are intertwined in a complex fashion, repeatedly folded throughout phase-space. A chaotic transient has finite lifetime, and is therefore inside the laminar basin. An appropriate way to envision this edge dividing phase-space is that a point in the basin is contained in an open region that set lies between the two symmetric parts of the edge, where this region can be extended to the origin without crossing

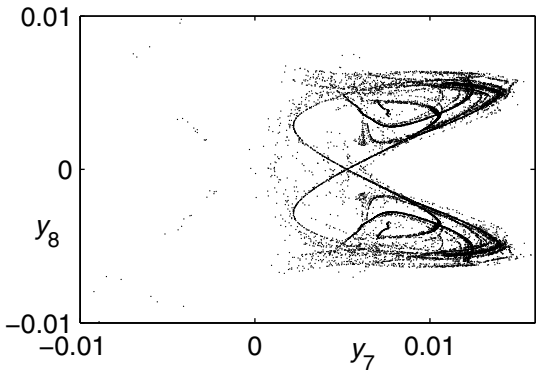

Figure 3.7: **The relative attractor.** From a long edge trajectory at $Re = 420$, we use the zero crossing of y_4 to construct a Poincare section. The graph shows only the y_7 vs. y_8 components. The data appears to have the fractal structure characteristic of chaotic attractors.

either edge.

Concluding remarks: the edge of chaos described here is significant for issues such as control of turbulence, since it separates the laminar from the turbulent. Transitions from the laminar to the turbulent state and vice versa will have to pass close to the edge of chaos described here. It is remarkable that even though the turbulent state and its almost space filling basin of attraction are high-dimensional, the edge orbits seem to be of much lower dimension.

Chapter 4

Details of the saddle in the model of plane Couette flow

Chapter 2 provided a short description of some of the principle results regarding the chaotic saddle in the 9-variable model of plane Couette flow. In this chapter, we provide a more detailed description of the techniques employed, with special focus on explaining those techniques which differ from previous research. Additionally, this chapter provides a more complete set of the numerical results on this chaotic saddle. Finally, this chapter will highlight some items for future research.

4.1 Background.

Osborne Reynolds, a British mathematician and scientist, was the first to identify that flow could be categorized into two broad regimes [1], which are now called "laminar" and "turbulent." His experiments in pipe-flow are considered to be seminal achievements. In addition to the purely laminar flow regime (for small fluid velocities) and turbulent (at high fluid velocities), Reynolds identified that there was an intermediate regime of non-dimensionalized velocities where the system exhibits both behaviors, with laminar flow interrupted by intermittent regions of transient turbulence. Characterizing this transition to turbulence remains one of the significant problems in fluid dynamics[2].

Plane Couette flow has a transition to turbulence that is similar in character to that of pipe flow in that the transition is dominated by transient behavior. Mathematically, the two flows share a common characteristic in that the laminar flow condition remains linearly stable for all Reynolds numbers [3]. Experiments and numerics show that near onset, the turbulence is transient, sometimes persisting for a very long time and then suddenly decaying to the laminar profile [4, 5, 6, 7, 3, 8, 9]. The transients are sensitively dependent upon initial condition, which, in experiment, may imply that the specific response to a perturbation may be "unpredictable."

This behavior can be contrasted with other shear flow problems, such as Rayleigh Bérnard and Taylor-Couette flow (viscous flow between two concentric, rotating cylinders), where rich spatio-temporal behavior can be reliably predicted over a wide parameter range. Figure 4.1, reproduced from [21], illustrates the structure of parameter space for Taylor-Couette flow. Some researchers

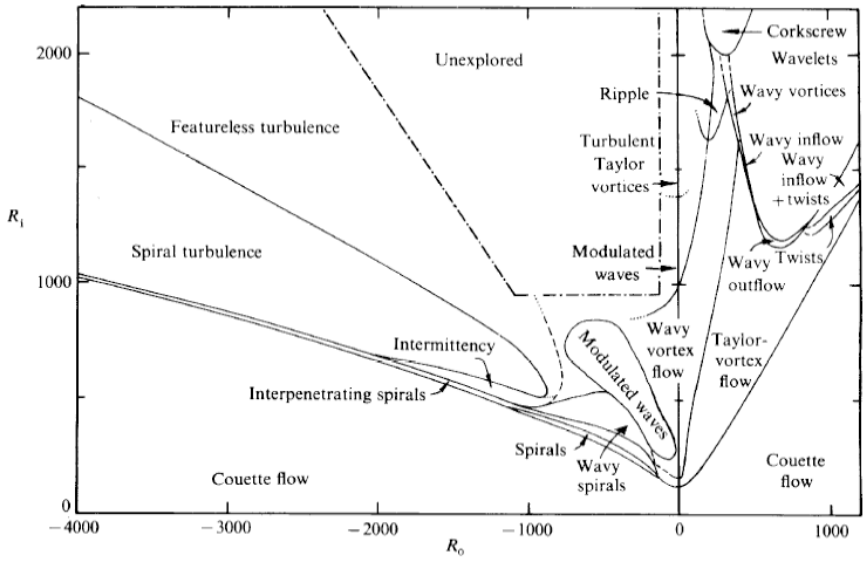

Figure 4.1: Behavior of Taylor-Couette flow over parameter space. The horizontal and vertical axes are the Reynolds number of the inner and outer cylinders in experiments by Andereck, Lui, and Swinney [21]. The experiments show highly repeatable behavior that was accurately predicted by the mathematical models.

have proposed that the sensitive dependence, as well as an exponential distribution of transient lifetimes, indicate the presence of a chaotic saddle in the dynamics [3, 4]. Our goal in this chapter is to characterize the chaotic saddle in a 9-variable model of plane Couette flow. Although similar analysis techniques have been applied to low dimensional systems, application of these tools to realistic physical problems of higher dimension have not been previously attempted.

4.2 The model

Because direct numerical simulation (DNS) is computationally expensive, several researchers [5, 11, 6, 12, 10] have developed low-dimensional representations based on Galerkin method, which allow parameter space to be more fully explored. Generically, this approach leads to a system of ordinary differential equations with quadratic coupling, linear damping, and constant forcing, with state space variable prescribing the time-varying amplitude for the selected modes. Taking $\boldsymbol{x} \in \mathbb{R}^n$ as the variable of state, the general form for these systems is given by

$$\dot{x}_i = -\frac{d_i}{Re} x_i + \boldsymbol{x}^T A_i \boldsymbol{x}, \quad i = 1., \ldots, n, \tag{4.1}$$

with A_i an $n \times n$ (typically sparse) matrix, and d_i a scalar constant. The values for the d_i, as well as the elements of the A_i depend upon two geometric parameters which determine the length and height of the periodic flow domain. The transient turbulence of the physical system is associated with transient chaos in these finite dimensional representations.

Eckhardt and Mersmann used this approach to develop a 19-variable model of plane Couette flow [5], and they identified additional symmetries which could be specified to further reduce this system. Schmiegel [10] showed that a 9-variable reduction had sufficiently rich behavior that it could be used to study the transient behavior of the system. The study of plane Couette flow in this work is based entirely on that model. As in [5], we take the periodic cell length to be 2π and a cell height of π, where unit length is defined as the width of the flow channel. The laminar flow condition is an asymptotically stable fixed point of the system. Therefore, by application of a linear change of coordinates, the laminar flow state can be placed at the origin of the coordinate system, with a transformed equation of motion given by

$$\dot{\boldsymbol{y}} = Q(\boldsymbol{y}; Re), \tag{4.2}$$

denoting that the new system is quadratic in $\boldsymbol{y}$ and studied over the parameter Re. To view an explicit listing of the equations of motion, please refer to Appendix A.

4.3 The *Lifetime* function and pseudo-trajectories.

A standard technique in the study of transient behavior is to consider the *duration* of a transient. For an autonomous system, this duration can be treated as a scalar function of points in phase space. For each point $\boldsymbol{y}$, we consider its trajectory under the flow of the dynamical system, $\phi^t(\boldsymbol{y})$. If some characteristic of the trajectory is transient, then we can find the first time, $t = t^*$ for which $\phi^{t^*}(\boldsymbol{y})$ no longer has that characteristic, and assign $L(\boldsymbol{y}) = t^*$ as the *lifetime* of $\boldsymbol{y}$. We then use the lifetime function as a tool to explore the transient characteristics of the system.

A typical lifetime definition for studying non-attracting chaotic sets (chaotic saddles) is to find a compact set in phase space that has no attractors, and define the lifetime to be the amount of time it takes the trajectory to leave that set. For our model of plane Couette flow, the laminar state is the only attractor that we are able to identify in the system, and every numerical trajectory asymptotically approaches the origin. One method for defining lifetime would be to place a small ball around the origin, and define the lifetime as the time it takes a trajectory to reach that ball. That method is used in both Chapters 3 and 5. As an alternative, in this chapter we choose to determine the transient lifetime based on the idea that while a trajectory is near the chaotic saddle, it shows sensitive dependence on initial conditions, and two nearby trajectories will *diverge* at an exponential rate. However, eventually, the trajectory will approach the stable origin. In some neighborhood of the origin, all nearby trajectories must *converge.* The lifetime of the chaotic transient is based on detecting this change in character. We determine this point of transition by comparing the base trajectory with a perturbed trajectory, rescaling the perturbation as required to keep the two trajectories sufficiently close that the difference provides a good linear approximation of the local expansion. As the base trajectory leaves the neighborhood of the chaotic saddle, the perturbed trajectory will begin to converge to the base trajectory. For any initial condition, we define its lifetime as how long it takes for the trajectory to reach that point in phase space where the perturbed trajectory begins to converge to the base trajectory. Chapter 6 contains a detailed explanation of this method. However, for the purposes of this chapter, it is sufficient to understand that the lifetime assigned to an initial condition reflects the duration of the chaotic portion of its

trajectory.

A chaotic saddle, C, is a non-attracting chaotic set, repelling all but a measure-0 set of initial conditions. Initial conditions whose trajectories approach C as time goes to ∞ lie on a stable manifold of one of the unstable periodic orbits in C. We call the collection of all such initial conditions the *stable set* of the saddle, C^s. Similarly, the set of initial conditions whose trajectories approach the saddle in backward time are called the *unstable set* of the saddle, C^u. We note that

$$C = C^s \cap C^u.$$

Almost every initial condition in phase space approaches the laminar flow condition and has a finite lifetime. We say that these points lie in the *laminar basin.* Our lifetime definition is based on a forward trajectory, so every $\boldsymbol{y} \in C^s$ will have an infinite lifetime [1]. In Appendix D, we prove that a dissipative system (such as our 9-variable model) must have an unbounded stable set. However, based on realistic physical assumptions, we can focus on a compact set of initial conditons that represent reasonable energies in the flow. We assume that if an initial condition has a long lifetime, then it is close to the stable set. Therefore, the lifetime function can be used to probe phase space to approximate the location of C^s. Figure 4.2 provides a graphical representation of the lifetime landscape, sampled on a two dimensional subspace for model data at $Re = 600$.

Data for 4.2 is from a two-dimensional sampling of 9-dimensional phase space, but the results are "typical" of such samples and we highlight some of the key characteristics:

- The black regions indicate that there are macroscopic regions of phase-space that do not intersect the stable set. Within these regions, the lifetime function is smooth.
- The speckled regions indicate that the lifetime function is varying rapidly in these regions, indicating the presence of many singularities in the lifetime function, where those singularities are points on the stable set.

[1] As a practical matter, the lifetime function is generally defined over some compact set S such that $C \subset S$ and S contains the portions of phase space that are of interest in some particular problem. However, it is often the case that C^s is unbounded. Consequently, those points in C^s that lie outside of S would not be assigned a lifetime value.

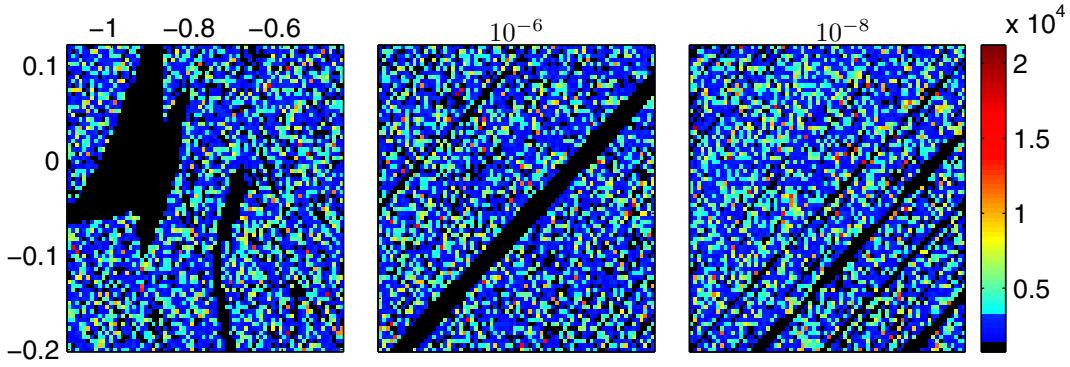

Figure 4.2: **Lifetime plots for a typical region.** Each figure shows a sampling on a $y_1 - y_2$ plane. The grids are shaded according to the lifetime of the center of each grid square, with black representing points that rapidly decay to the origin (rapid return to laminar flow). Coordinates are provided for picture 1, and show that the sample is not near the origin. Picture 2 provides a finer resolution by considering a size 10^{-6} box centered at $(-0.65, 0.05)$. The third picture is a size 10^{-8} resampling of the lower left corner of picture 2. The three pictures all show macroscopic areas of short lifetime. The "speckled" regions, where short and long lifetimes are intermingled, indicate that the sampled points are "near" the stable set of the saddle.

- The dense speckling (at all scales) indicate that the stable set is nearly full measure. (As described later in this chapter, the fractal dimension of this set is ≈ 8.98. for the $Re = 600$.)

- The broader pattern of macroscopic black regions intermingled within speckled regions is detectable on all three scales, indicating a fractal structure.

Although sampling of phase-space can reveal some of the structure, it is an impractical approach in higher dimensional systems as it is quickly becomes computationally intractable to obtain a sufficiently dense sample. Additionally, in a typical sampling approach (such as the "sprinkle method" of [22] the dynamics do not play a direct role in the chosen sample set, making it difficult to recover natural measures. Much of the theory of dynamical systems is based upon asymptotic results using these natural measures associated with the invariant objects in phase space. Under typical assumptions, long trajectories of the system are used to gather the necessary

statistics. For chaotic attractors, simple numerical integration is sufficient to yield arbitrarily long trajectories, and shadowing theorems [23] and principles of ergodicity are used to assert that computations based on these long trajectories are representative of system behavior. Eckmann and Ruelle [24] provides an appropriate review of application of ergodic theory to chaotic attractors.

In order to apply these measure based principals to understand a system with a chaotic saddle, it is useful to compute long trajectories of the system. However, because the saddle is an unstable invariant set (non-attracting), simple numerical integration is not sufficient. The techniques of [19, 18, 25] provide some options for approaching this type of problem, though [19] is limited to saddles with a single expanding direction. We chose to use a modified Step-and-Stagger technique [13] to study the saddle in this model of Couette flow. In [13], the authors demonstrate the technique on low dimensional systems, and assert that it can be applied in higher dimensional systems with an arbitrary number of positive Lyapunov exponents. To our knowledge, this research reflects the first application of this approach to a high dimensional system of physical relevance.

The basic Step-and-Stagger attempts to construct an arbitrarily long *pseudo-trajectory* as a numerical approximation to an actual trajectory along the stable set of the saddle. The basic idea is that one can establish a threshold value T^* for lifetime such that if $L(\boldsymbol{y}) > T^*$ then $\boldsymbol{x}$ is assumed to be sufficiently close to the stable set. Starting from some $\boldsymbol{y}_0$ with a long life, the pseudo-trajectory evolves in accordance with system dynamics, except that when necessary, the trajectory is perturbed by some small amount δ to increase the lifetime such that all points on the pseudo-trajectory have lifetimes higher than the threshold T^*. By requiring $\|\delta\|$ to be small, the generated numerical trajectory can be expected to approximate an actual system trajectory on the saddle with sufficient accuracy to estimate Lyapunov exponents. The cartoon of Fig 4.3 illustrates the strategy. The small perturbations are called "staggers," and each stagger is found by conducting a random search. Our technique, which we call *Multistagger*, is essentially the same approach, with minor modifications to the search technique as well as the threshold criteria. We require that a successful stagger raise the lifetime by some minimum amount ΔL. While searching for a suitable perturbation, we accept any improvement in lifetime, and take subsequent perturbations from

that new basepoint. Figure 4.4 illustrates this modified approach. Appendix B contains a more detailed description of the multistagger technique as well as additional discussion of our methods for choosing algorithm parameters.

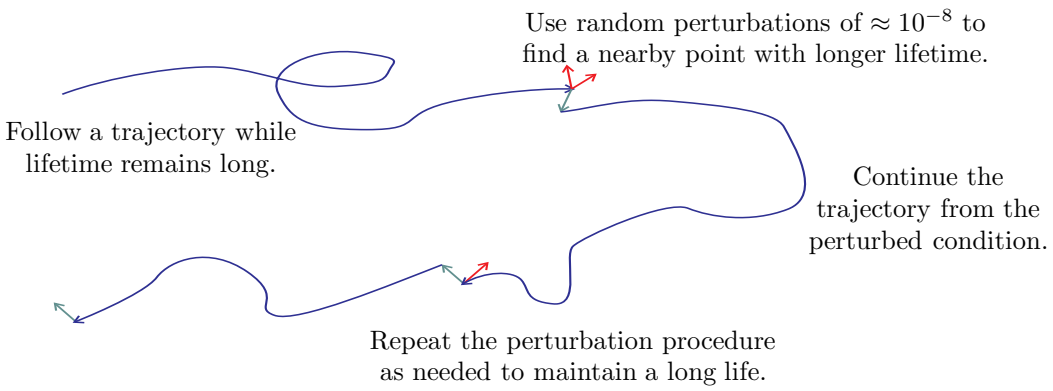

Figure 4.3: **Schematic of a pseudo-trajectory.** A pseudo-trajectory is created by following system dynamics while the lifetime is above threshold. To keep a long lifetime, occasional perturbation are used to find nearby points with long life. An acceptable perturbation (green) is found by random search, rejecting perturbations that do not increase the lifetime (red).

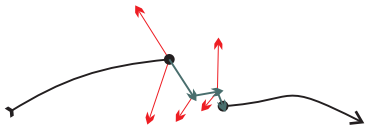

Figure 4.4: **Multistagger technique.** Perturbation that raise lifetime (green) are accepted, while we reject points of lower lifetime. When lifetime has been raised by ΔL compared to the initial point, we continue the pseudo-trajectory by integrating the system (black) Appendix B provides a detailed explanation.

4.4 Numerical results for Lyapunov spectrum

Lyapunov exponents provide a key characterization of a chaotic set. In particular, the desire is to compute Lyapunov exponents that are representative of the natural measure on the chaotic saddle. The criteria for construction of long-pseudo trajectories was based on a long "forward"

lifetime, which should ensure that the trajectory remains near the *stable* set of the saddle, and not necessarily the saddle itself. However, if we assume that a pseudo-trajectory approximates a system trajectory, then after some transient period, the flow of the system should cause that trajectory to converge toward the saddle. Consequently, except for the initial transient phase, we assume that the pseudo-trajectory provides statistical information that is characteristic of a trajectory on the saddle.

To compute the Lyapunov spectrum, we generate a pseudo-trajectory of $O(10^6)$ time units, and then discard the first 20% of that trajectory as transient. We then compute the full spectrum of exponents by integration of the tangent bundle. The primary parameter range of interest was $350 \leq Re \leq 800$. For this parameter range, the saddle is expanding in two directions (two positive Lyapunov exponents) [2] . The multiple expanding directions in this low dimensional model is consistent with the observations of the full numerical simulation of [4]. Figure 4.5 illustrates the results for Lyapunov spectrum as calculated from the pseudo-trajectories.

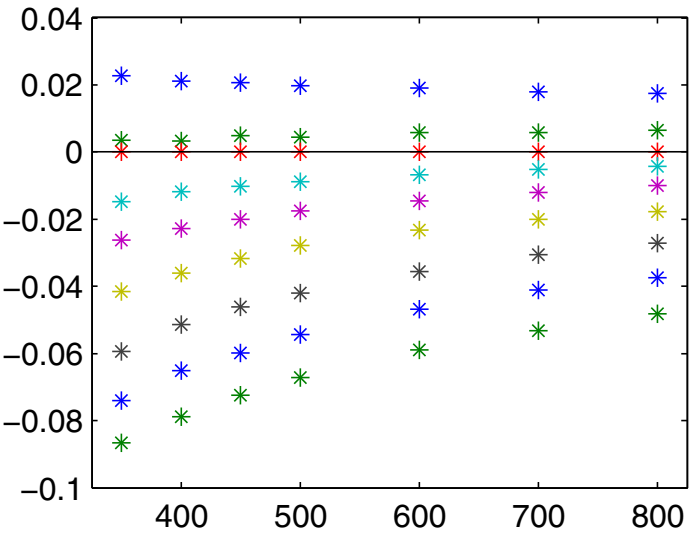

Figure 4.5: **The nine Lyapunov exponents for** $350 \leq Re \leq 800$. The saddle has two positive exponents for this entire parameter range, with one 0 exponent because the system is autonomous.

[2] Because the system has two expanding directions, the PIM-triple method would be expected to fail, making this problem a good candidate for Step-and-Stagger

It is typical of many physical models in higher dimensions that the system is non-hyperbolic. The effect of the non-hyperbolicity can be examined using finite time Lyapunov exponents. The time-T Lyapunov exponents, $\{\lambda_i^T\}_{i=1}^9$, describe the growth rate of small perturbations along a trajectory of length T. For our Couette flow model, the system had two positive exponents, but the second was close to 0. Consequently, we focus on λ_2^T, and consider its distribution. In [26], it is shown that systems with fluctuating number of positive Lyapunov exponents will fail to have an arbitrarily long shadow trajectory. Figure 4.6 shows a plot of distributions for λ_2^T for $200 \leq T \leq 1000$. A significant portion of each distribution falls to the left of 0, and we can conclude from the arguments of [26, 27] that shadowing distance will be finite. The numerical trajectory will shadow a true trajectory for some finite period, and then it will experience a "glitch." After the glitch, the numerical trajectory will be shadowing a different system trajectory (until the next glitch). However, as is typical in the literature, we assume that a long pseudo-trajectory provides adequate accuracy in estimating Lyapunov exponents for the system.

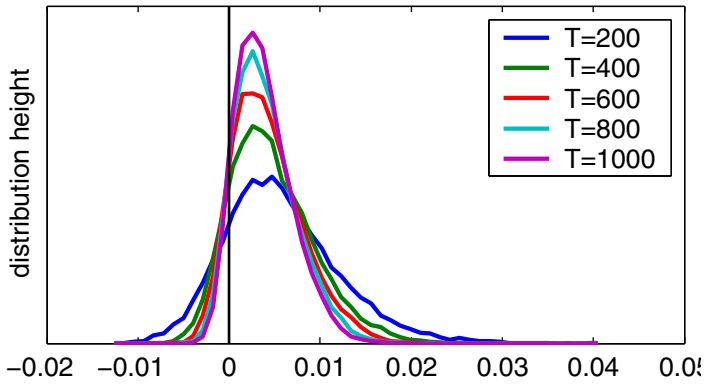

Figure 4.6: **Distribution for finite time Lyapunov exponent** λ_2^T, the second largest Lyapunov exponent, plotted for $200 \leq T \leq 1000$. Although the distribution mean is positive, a significant portion of the distribution lies to the left of 0, indicating that shadowing time will likely be finite.

4.5 Decay time

Trajectories near the chaotic saddle are repelled from the invariant set. If one assumes that the natural measure on the saddle is ergodic, then trajectories that start very close to the saddle

would be close to some saddle trajectory, and would therefore visit near every point on the saddle. Consequently, the rate at which trajectories are repelled from the saddle can be treated as a global characteristic. Suppose we start with a large ensemble of $N(0)$ initial conditions taken uniformly from some set W which intersects the saddle. Let $N(t)$ be the number of those initial conditions whose lifetime exceeds t. Because of the saddle structure of the invariant set, we can expect that for some constant $c > 0$,

$$N(t) \sim \mathrm{e}^{-ct}. \tag{4.3}$$

Following the terminology of [14] we define *decay time,*[3] τ by

$$\frac{1}{\tau} = \lim_{t\to\infty} \lim_{N_0\to\infty} \frac{-\ln\left(n(t)/n(0)\right)}{t}. \tag{4.4}$$

In Appendix D, we prove that the decay time, as an asymptotic value, is essentially independent of the specific random sampling strategy.

We note that as τ increases, the transient behavior becomes more persistent, with the limiting situation of $\tau = \infty$ indicating a chaotic attractor. As a global characteristic, it is reasonable to study the behavior of τ as we vary the controllable parameter Re. To determine τ, we take a large sample of initial conditions and plot the cumulative distribution of the sample, $F(t) = N(t)/N(0)$, as a function of t, plotting on a logarithmic scale (where exponential decay should plot as a line). For small t, the shape of the distribution is somewhat determined by the sample region of phase space. However, for t large, the trajectories of long lifetime must remain near the saddle for a long time, so the exponential decay characteristic of the saddle begins to dominate. The graph should show a range $t_1 \le t \le t_2$ where the graph is nearly linear (which determines t_1) yet the sample size is still large enough that statistical errors are small (which determines the choice of t_2). Then curve fitting to that linear portion yields a value for the slope of the linear portion, which should approximate $-1/\tau$. In some sense, it is the existence of the linear regime on these semilog plots

[3] In some of the literature, τ as defined by (4.4) is called the *average lifetime*, which is somewhat of a misnomer. If lifetimes were distributed precisely in accordance with an exponential distribution, generating the cumulative distribution for lifetime $\mathbb{P}(L > t) = \mathrm{e}^{-t/\tau}$, then τ would be the expected value of that distribution. However, in general (4.3) is accurate only for t sufficiently large. The average lifetime over a general set W will depend upon both W and the specific definition of the lifetime function.

that indicates that the transient behavior is due to a chaotic saddle. Figure 4.7 show a partial data set collected for a range of Re.

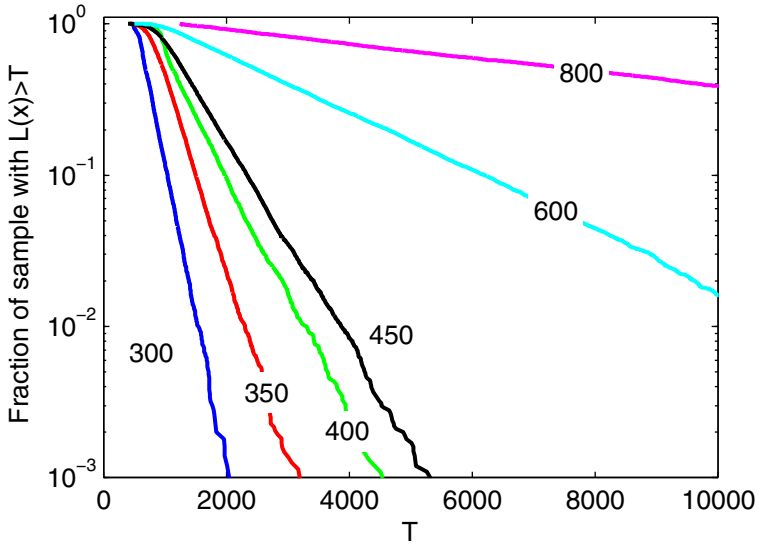

Figure 4.7: **Cumulative distribution of lifetimes.** $F(t) = N(t)/N(0)$,is plotted as a function of time on a semilog plot. A linear shape on this graph indicates the presence of the saddle, and the slope of the linear portion is $-1/\tau$. Each curve is labeled with its Reynolds number. The data clearly shows that τ is increasing with Re.

Some experimental results indicate that over some range of Re, the gross relationship between the Re and the decay time is given by

$$\tau = \frac{\alpha}{R_c - Re}, \tag{4.5}$$

where α is constant, and R_c would be a *critical Reynolds number*. If this scaling law were to hold, at $Re = R_c$, a chaotic attractor would emerge. Figure 4.8(L) shows the data collected over the parameter range of interest, with $1/\tau$ plotted against Reynolds number, where (4.5) would plot as a straight line on this graph. The graphic indicates linear ranges of the parameter, but also an apparent bifurcation at $Re \approx 400$ and again at $Re \approx 600$. Although the data in these ranges can be used to fit the ansatz to yield a value R_c, there appears to be no emergence of a chaotic attractor in our 9-variable model in the parameter range that we studied. To be more precise, throughout

our extensive simulations, all numerical trajectories decayed to the origin. However, it is possible that a chaotic attractor with a small basin of attraction might remain undetected in this high dimensional space. [We note that in [28], using a 9-variable model with the same form of (4.1) but with slightly different modes than in our model, the authors did observe a chaotic attractor for some ranges of Re.] Other experimental and numerical results indicate transient lifetime might scale exponentially with Reynolds number in these shear flows, with ansatz

$$\tau \sim \mathrm{e}^{\beta Re}. \tag{4.6}$$

Figure 4.8(R) shows how the numerical data from this model might be fit to that form.

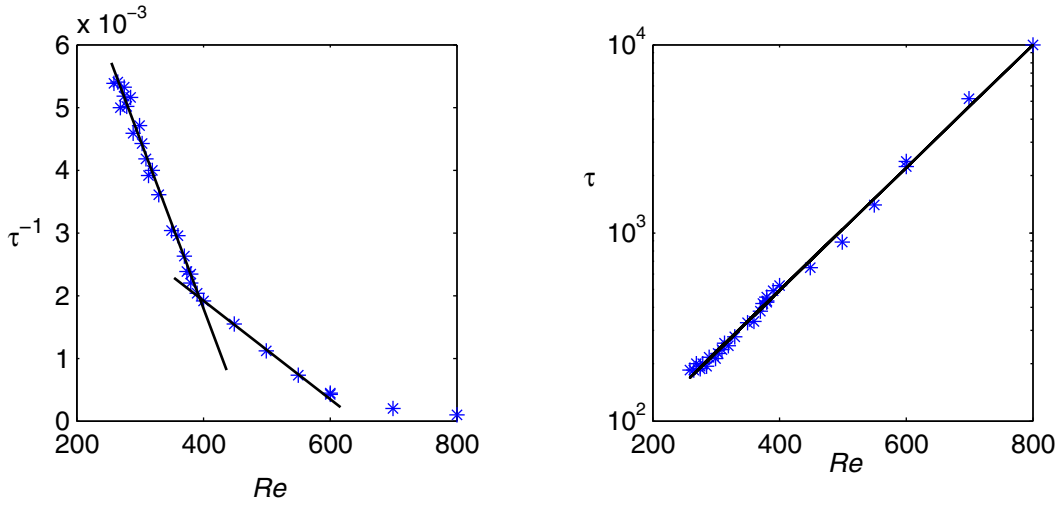

Figure 4.8: τ **vs.** Re. (L) $1/\tau$ is plotted against Re. The linear slope indicates agreement with (4.5) over various ranges of the parameter. However, since $1/\tau > 0$, no attractor emerges in our model. (R) The same data set, with τ plotted vs. Re on a semilog scale. A linear relationship on this graph would indicate that lifetime grows exponentially with Reynolds number, in agreement with (4.6)

4.6 The dimension of the saddle

In trying to quantify the "size" of the chaotic saddle, we focus on two key invariant sets – the stable set of the saddle (or simply the *stable set*) and the saddle itself. The importance of the stable set

is that it is a primary physical observable. The general approach to a transient system (whether model or experiment) is to take an initial condition, and test its lifetime. Such experiments, based only on lifetime, will reveal whether an initial condition is close to the *stable set* (but might reveal little about the actual saddle). The probability of finding a long-lived transient, therefore, is related to the fractal dimension of the stable set, which we denote D_s. For systems with a robust transient character, the decay time is closely related to D_s, through the largest Lyapunov exponent, λ_1. As identified in [15], in an N dimensional system, if τ is sufficiently large, then

$$d := N - D_s = (\tau\lambda_1)^{-1}. \tag{4.7}$$

We call d the *defect* of the stable set. The formulation in [15] assumes that generically, a line through phase space will have a non-empty intersection with the stable set, or equivalently, that $D_s > N - 1$. Therefore, $d < 1$, implies that (4.7) should apply whenever $\lambda_1 > 1/\tau$, which, for our model, is satisfied throughout the parameter range studied. Fig 4.9 illustrates the close relationship between τ and d for this system.

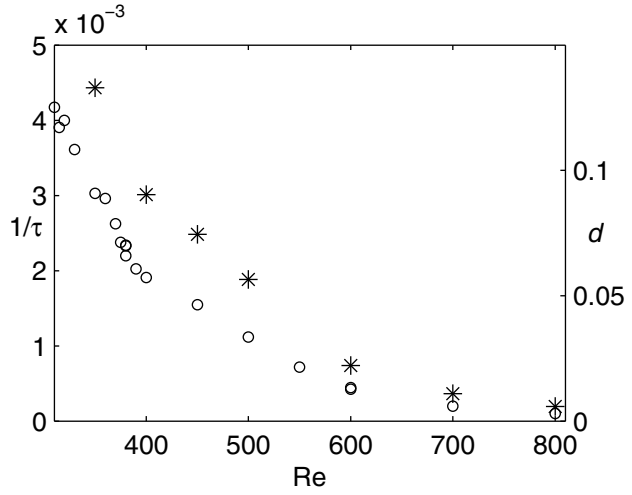

Figure 4.9: $1/\tau$ (circles) and defect $d := 9 - D_s$ (asterisks) plotted as a function of Reynolds number (Re). Since λ_1 is approximately constant over this parameter range, the shape of the defect curve closely matches the shape of $1/\tau$.

For large Reynolds number, the defect is very small, and the stable set becomes nearly dense

($D_s \approx 8.98$ at $Re = 600.$). Consequently, long-lived transients become "easy" to find in most regions of phase space. Additionally, since τ is getting large, the typical lifetime of these transients is getting longer. In a physical experiment, where the duration of the experimental run would be some fixed, finite maximum, the very dense long-lived transients might be indistinguishable from sustained turbulence, even if a chaotic attractor has not formed.

Although the *stable set* is the invariant set of interest to understand the trajectory of a sampled initial condition, the chaotic saddle itself describes the region of phase space where long trajectories are located during most of the transient phase. A typical transient (near the stable set) will start near some point on the stable manifold, moving along that invariant set toward the saddle. The trajectory will then remain near the saddle for a long time before decaying to the laminar state by exiting the saddle region along an unstable manifold. Therefore, the saddle set is an important invariant object because the transient spends much of its time near this set. To find the dimension of the saddle, we apply the formulation of [14], which generalizes the Kaplan-Yorke dimension to chaotic saddles [4]. In addition to τ, these computations require the full spectrum of Lyapunov exponents, but they permit the determination of the dimension of the stable set, the unstable set (points that approach the saddle in backward time) and the saddle itself. For D_s, the results are algebraically equivalent to (4.7)[5]. Figure 4.10 plots dimension versus Reynolds number for both the saddle and the stable and unstable sets.

4.7 The "hole" in the saddle.

In the previous section, we discussed the importance of two of the three invariant sets: (1) the stable set, detected by sampling, which is nearly full dimension, and (2) the saddle, where transient trajectories spend most of their transient life. The third key invariant set is the *unstable set.* Using the notation that D is the dimension of the saddle, and D_u for the dimension of the unstable set, if we assume that the intersection of the stable and unstable sets is generic, then $D = D_u + D_s - N$. We previously noted that the stable set is nearly full dimension and denoted the *defect* as $d = N - D_s$,

[4] [22] contains a similar result to [14], but uses a very different formulation to derive the result.

[5] Appendix C provides a short explanation of the relationship between the two formulations.

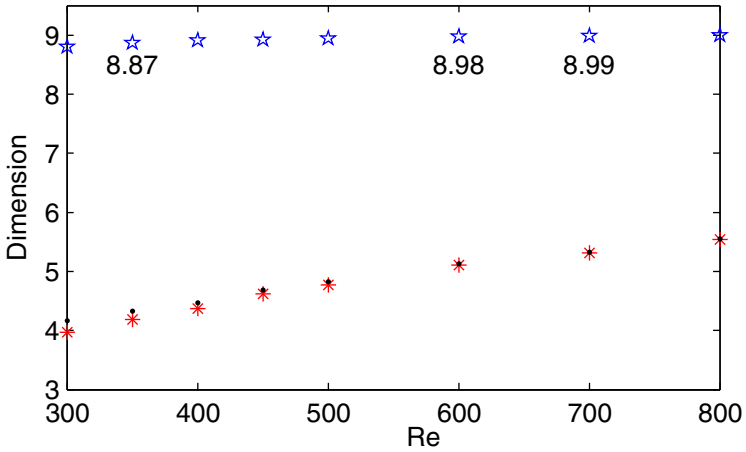

Figure 4.10: **Dimension of the invariant sets.** The information dimension for the chaotic saddle (blue) and its stable set (red) and the unstable set (black) are plotted as a function of Reynolds number. The stable set becomes nearly dense as Reynolds number increases, making it "easy" to find a point near the stable set, which would result in a chaotic transient.

so that

$$D_u = D + d.$$

Consequently, when the defect is small, the unstable set is only slightly larger than the saddle itself. For the most part, the chaotic saddle lies on the unstable manifolds that compose D_u. However some small portion of these unstable manifolds tend to drive orbits away from the saddle. As a transient trajectory begins its final stages of decay, it will depart the neighborhood of the saddle along the expanding direction of portions of these unstable manifolds, and we desire to better understand this decaying behavior.

We first revisit the *lifetime* function. The standard approach is to enclose the unstable structure with a compact set S that contains no attractors. Then the lifetime of a point in S is the time it takes for a trajectory of that point to leave S. Generally, S is chosen to have an easy geometric description. However, in this chapter, the *lifetime function* that is used is based on detecting the change from exponential sensitivity to initial conditions (near the saddle) to convergence of nearby trajectories (as they approach the attractor). To further exploit this

lifetime function, we note that we may still associate the lifetime of a point with its time of first exit from some set $\overline{S}$, where S contains all points with positive lifetime. In general, S no longer has a simple geometric description and is not compact. However, the set contains boundary points (where lifetime approaches 0), and we denote the set of boundary points as ∂S. Then ∂S describes a surface in phase space such that once a trajectory passes through this surface (under forward time flow), all nearby trajectories will begin to converge.

Recalling that C^u denotes the unstable set of the saddle, we can now define the *hole in the saddle* to be the set

$$H := \partial S \cap C^u.$$

We can think of the *hole* as a cross section of the unstable set, with the section taken such that trajectories on the section are leaving the saddle set. If we assume that the intersections are generic, then we expect

$$\dim H = D^u - 1 = D + d - 1. \tag{4.8}$$

Although much of C^u may coincide with the saddle C, the hole describes trajectories that are decaying to the origin, and consequently, $H \cap C = \emptyset$.

To approximate the *hole*, we consider an ensemble of initial conditions $\{\boldsymbol{y}_i\}, \boldsymbol{y}_i \in \mathbb{R}^9$, that are chosen from a pseudo-trajectory such that all the points have long life and approximate a natural measure on the saddle. For each of these points, we may compute its lifetime, $l_i := L(\boldsymbol{y}_i)$. Then we identify the point $\boldsymbol{y}_i' := \phi^{l_i}\boldsymbol{y}_i$, which describes where the trajectory of $\boldsymbol{y}_i$ intersects ∂S. The resultant ensemble $\tilde{H} = \{\boldsymbol{y}_i'\}$, allows us to visualize the typical path through which transient trajectories decay to laminar flow.

Our simplified description is that because the saddle has a stable set that is nearly full dimension, it is "almost" an attractor, but that it permits a little bit of leakage. More precisely, a chaotic saddle typically contains an infinity of unstable periodic orbits, and the saddle is the closure of the unstable manifold of all but a small (possilbly finite) number of these periodic orbits. Those periodic orbits whose unstable manifold are not part of the chaotic saddle are the ones that create the leakage from the saddle. If the saddle set is transitive, then trajectories near the saddle would

eventually visit sufficiently close to one of those periodic orbits, allowing the trajectory to escape the neighborhood of the saddle and decay to laminar flow. In Fig 4.11, we provide a visualization of the *hole* for an ensemble at $Re = 390$.

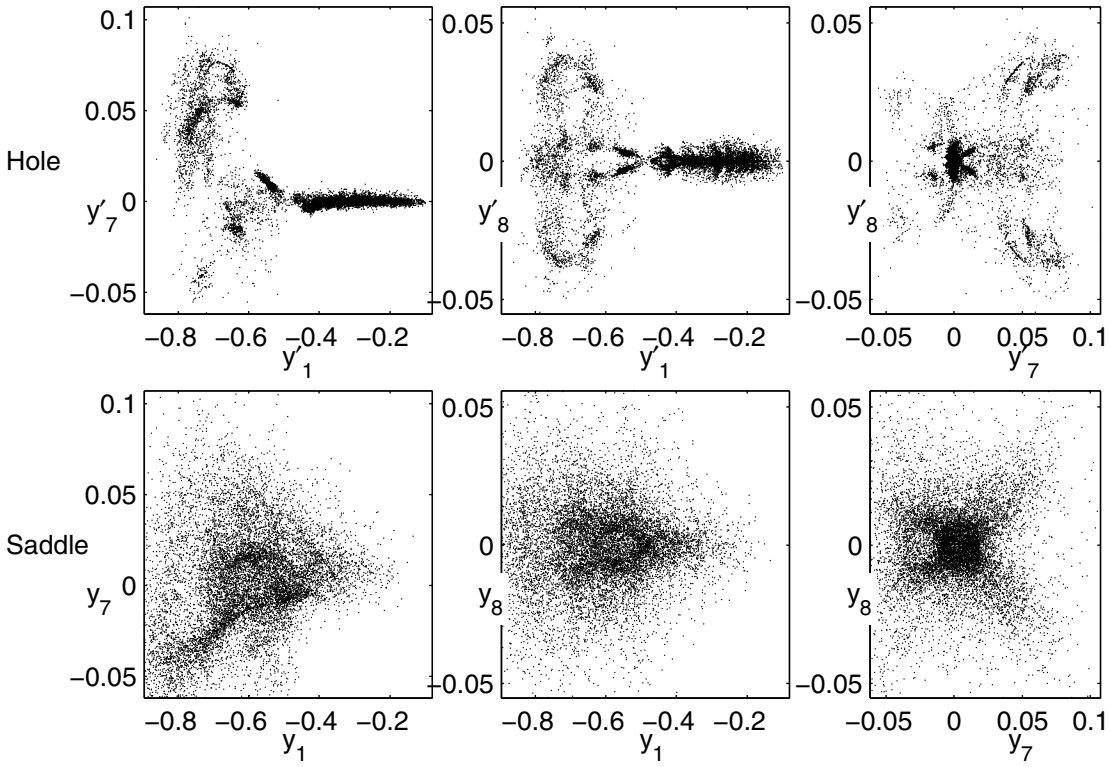

Figure 4.11: **Comparing the saddle with the hole (**$Re = 390.$**)** An ensemble of ≈ 11000 points is generated as described above. All points are in $\mathbb{R}^9$, but we plot the projection of those points into a two-dimensional subspace. The top row plots the ensemble at the hole, viewed from the $y'_1 - y'_7, y'_1 - y'_8$, and $y'_7 - y'_8$ planes, where the "prime" notation on the axes does not represent a change of phase space, but simply emphasizes that these are points from the ensemble $\tilde{H}$. The lower row of plots is the same projections, but plotting the ensemble of initial conditions on the saddle. The apparent lack of structure in the saddle is a result of projecting a high (≈ 4) dimensional object into two dimensions.

The data in Fig 4.11 is typical for the parameter range studied. We make the following observations from our analysis of those plots:

- The estimated correlation dimension for the data set is $D_2 \approx 2.9$ (at 10^{-4} scale) for the *hole*, while for the *saddle* ensemble, $D_2 \approx 3.8$ (at 10^{-3} scale). These measurements are consistent with (4.8), providing some verification that are procedure for approximating the hole is valid.

- Even in the 2-dimensional projection, we are able to detect that the hole has significant structure.

- About 2/3 of the hole points are in the cluster with $y_1' > -0.5$, indicating points that continue to have transient chaotic behavior even as they reach relatively low energy levels. The other components of these points are also very small in magnitude, such that the points are confined to a narrow region along the y_1 axis. In relation to the physical system, points near the y_1 axis would be associated with flows that may have significant deviation from the mean laminar profile in the streamwise direction, but with little or no streaks and eddy's.

- From the $y_1 - y_7$ plane views, we note that for higher energy points (where $y_1 < -0.5$), the hole is more heavily weighted to positive values, while the saddle is weighted to negative values.

- From the $y_1 - y_8$ views we can see significant clusters at large amplitude y_8' for the hole, while these are relatively low density regions for the saddle. Additionally, we see that the hole retains structure, even at the low energies.

- In the $y_7' - y_8'$ view, we note the winglike clusters that indicate an apparent high energy leakage path.

Our observations regarding the hole indicate that the leakage paths have structure, which are possibly related to the slow manifold of a small number of periodic orbits whose unstable manifolds are not part of the chaotic saddle. This structure is potentially exploitable. We imagine that it might be possible to design a control strategy that would target regions of the saddle that have a propensity for leakage, with a goal of reducing the average length of a transient. However, the analysis of the these leakage paths remains an area where further work is required.

4.8 Conclusions

Understanding transient turbulence remains an important problem in fluid dynamics. In full numerical simulations and experiments, it appears that the turbulent landscape is sensitively dependent upon initial conditions. In a finite dimensional models, this behavior is best characterized by a chaotic saddle. In this paper, we chose to study a small dynamical systems that appears to capture much of the relevant characteristics of such flows. Our primary conclusions are that (1) robust transient behavior can be associated with a stable set of the saddle which is nearly full dimension, (2) the Step-and-Stagger algorithm can perform robustly, even in higher dimensional systems, and (3) the increased analysis of the leakage paths from the saddle may lead to development of additional techniques with direct application to minimizing transient turbulence.

Chapter 5

Describing the *Edge of Chaos* in a model of parallel shear flow

We study a parallel shear flow model, where a stable laminar flow and transient turbulence coexist. Using a Galerkin representation, we study the boundary between these two characteristic behaviors. In the model, some regions of phase space show strong sensitive dependence on initial conditions, with transient lifetimes that fluctuate wildly, while in other regions of phase space, the transient lifetimes behave smoothly. We identify an invariant saddle structure that lies between these regions, which we call the *edge of chaos.* We describe a technique for computing trajectories on this invariant object. We find that for some ranges of Reynolds number, the *edge* coincides with the stable manifold of a periodic orbit, while in other ranges, trajectories on the invariant set have a higher dimensional chaotic object as their limit set.

The *edge of chaos* was introduced in Chapter 3. This chapter provides a more detailed description of edge and the techniques employed to study the edge.

5.1 Introduction

Parallel shear flows, such as plane Couette flow or pipe flows, have the ability to produce turbulent dynamics even while the laminar flow condition remains linearly stable [1]. The experimental evidence, supported by numerical studies, shows that as the Reynolds number (Re) increases above some threshold value, the system may exhibit transient turbulent behavior. These transients may persist for a very long time before rapidly decaying and allowing the system to return to the laminar profile [4, 5, 6, 7, 3, 8, 9]. The average lifetime of the transients increases rapidly with Reynolds number, often becoming longer than the typical observation time of physical experiments or detailed numerical simulations, even at moderate flow rates. A significant body of evidence, from both physical and numerical experimentation, has led some researches to interpret the transients as indications of a chaotic saddle [3, 4]. Because full numerical simulations are computationally com-

plex, exploring phase space structures using those models is generally not practical. Consequently, several researches developed low dimensional Galerkin models of these flow to facilitate study of these chaotic saddles [5, 11, 6, 12, 10]. Chapters 2 and 4 provide a description of the chaotic saddle using a 9-variable model that was proposed in [5] and studied more extensively in [10]. Those chapters focus on the statistical quantifiers, such as Lyapunov exponents and fractal dimensions, and emphasize the overall structure and transient behavior, linking it to previous general results on chaotic saddles [14, 15]. In this chapter, we focus our analysis on the boundary between the laminar state and the transient turbulence. Previous work suggests that as one moves away from the laminar state in phase space, there seems to be a well defined envelope to the chaotic transients [5, 6, 7, 4]. We call this structure the *edge of chaos* because chaotic trajectories come arbitrarily close. In Fig 5.1, we provide a visualization of this structure.

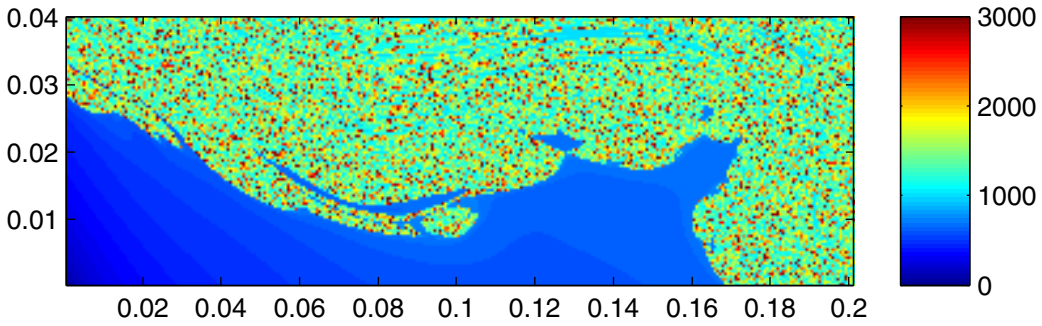

Figure 5.1: **Lifetime on a 2-d subspace.** Transient lifetime from the 9-variable model is computed for initial conditions on a randomly chosen 2-d subspace, with the laminar state at the lower left corner of the plot. Each block is colored based on the lifetime of its center coordinate. The field of blue appears to be separated from the speckled regions. We call that separating structure the *edge of chaos.* (Parameter $Re = 420$)

In this paper, we describe the following key findings regarding the *edge* in this model of shear flow:

1. The *edge* is composed of an unstable invariant set that moves smoothly with changes in the

Reynolds number, and we present evidence that the *edge* is a surface in phase space.

2. For some ranges of Reynolds number, the edge coincides with the stable manifold of a symmetric pair of periodic orbits. A similar phenomena has been identified in planar maps with multiple basins of attraction, such as the forced damped pendulum [17], but to our knowledge, these structures have not previously been identified in higher dimensional systems.

3. For other ranges of the Reynolds number, trajectories on the edge are no longer asymptotically periodic, but chaotic. When we consider the restriction of dynamics to the invariant set, we discover a high dimensional and fractal chaotic set that attracts the edge trajectories.

Additionally, we developed techniques that allowed efficient computation of edge trajectories. We explain those techniques in hopes that they may have application to other systems that show transient chaos.

This chapter is organized as follows: In §5.2 we introduce our model of shear flow. In §5.3 we define the edge and describe how it relates to the transient lifetime structure of the system. §5.4 provides a detailed description of our efficient computational methods for following trajectories on the edge. §5.5 describes the nature of the invariant edge structure. In §5.6, we provide some initial results from our studies at low Reynolds number. §5.7 illustrates how the edge relates to the decay of transients. In §5.8, we prove that a horseshoe generates an edge and prove that the edge in the horseshoe is a manifold. §5.9 discusses the smoothness properties of the edge. §5.10 provides some concluding remarks, with direction for further research.

5.2 The model

Because extensive numerical simulations are required to study structures in phase space, we developed our ideas using a simplified 9-d model of shear flow, based on a Galerkin method approximation. In [5], the authors developed a 19-variable model of plane Couette flow and proposed some additional lower dimensional models that could be derived by applying additional symmetries to the problem. The general structure of this broad class of approximations to shear flow is a finite

dimensional ordinary differential equation with quadratic coupling, linear damping, and a constant forcing, with periodic boundary conditions in the streamwise and spanwise directions:

$$\dot{x}_i = -\frac{d_i}{Re}x_i + \sum_{j,k} a_{i;j,k}x_j x_k + f_i, \quad i = 1., \ldots, n. \tag{5.1}$$

In addition to specific choice of modes, there are three essential parameters in these models: the Reynolds number, which dictates the damping, and the geometric parameters that determine the size of periodic flow cell. In [10], the author studied one of the 9-dimensional reduced models from [5] and showed that it captured some of the main qualitative features of both the 19-variable model as well full numerical simulations. We study that 9-dimensional model, with the additional constraint of fixed geometry, where we take the periodic cell length to be 2π and a cell height of π, where unit length is defined as the width of the flow channel. The laminar state is a fixed point of that system, so we translate that system so that the laminar state is at the origin. We denote this new system $\dot{\boldsymbol{y}} = Q(\boldsymbol{y}; Re)$ to emphasize that the right hand side is quadratic in $\boldsymbol{y}$ and will be studied over the parameter Re. Throughout this paper, we denote the flow of that differential equation by ϕ^t.

5.3 The "lifetime landscape" and *edge points.*

To facilitate study of transient behavior, we define a *lifetime function*, $L(\boldsymbol{y})$, defined as the time it takes for the trajectory of $\boldsymbol{y}$ to approach within some fixed distance ϵ of the origin. By standard theorems from ordinary differential equations, each point in phase space is assigned a unique lifetime (possibly infinite). Because the origin (the laminar state) is attracting and linearly stable, we can choose ϵ such that dynamics inside the ball are described by simple exponential decay, ensuring that we are discarding no interesting dynamics. Points of finite lifetime are said to be in the *laminar basin*. However, based on the results of Chapter 4, we know this system contains a chaotic saddle — a measure 0 set of points which do not approach the laminar state. These points in phase space will have an infinite lifetime, and we say that these points belong to the *saddle set.* By these definitions, we may conclude that the *laminar basin boundary* is the entire saddle set.

Chapter 4 provided detailed statistics about the behavior of the saddle set as a function of

Re. Of particular note was that the saddle set was shown to be a nearly dense fractal. However, our interest here is to focus upon the boundary of that fractal structure. A common characteristic, detected not only in low-dimensional models of shear flow [6, 5, 10], but also in fully resolved simulations [4, 7], is that the lifetime function follows a typical pattern. As distance from the laminar state is increased, the lifetime function initially increases, but at a slow rate. However, as the perturbation size approaches some threshold value, the lifetime increases rapidly. Beyond that threshold (the *edge*), the lifetime function fluctuates wildly, reflecting the fractal structure of the saddle set, with lifetimes that depend sensitively upon the initial condition. Figure 5.2 illustrates this very general characteristic.

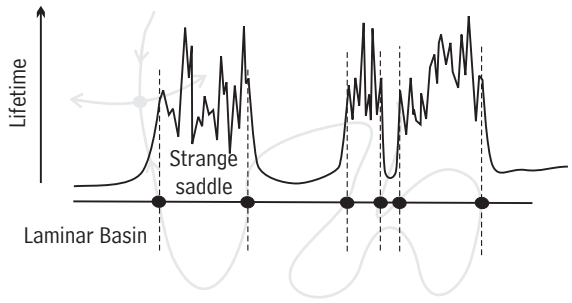

Figure 5.2: **Lifetime indicates the edge.** Lifetime $L(\boldsymbol{y})$, sampled along a line. In the laminar basin, $L(\boldsymbol{y})$ is smooth, while in the saddle region, it appears fractal. The boundary between those behaviors is an edge point. The gray curve (extended in Fig 3.3) is drawn to illustrate that the behavior on the sampling line is related to larger structures in phase space.

That the lifetime function has smooth regions interspersed with wildly fluctuating regions is typical of chaotic saddles, and has been termed the typical "lifetime landscape" [18, 5, 6] of a chaotic saddle. Similar structures will be observed whenever the saddle set has fractal dimension D, with $n-1 < D < n$ for a system in $\mathbb{R}^n$, because a typical line through phase space will have a non-empty intersection with the saddle set. Consequently, for systems with robust transient chaos, this behavior is typical.

From the results of Chapter 4, the saddle set (equivalent to the stable set of the saddle) [1] has

[1] In Chapter 4 we described the *saddle* as the invariant object (under both forward and backward flows) and the

dimension just slightly less than 9 for our parameter range of study. A line through phase space intersects the saddle set on a measure-0 Cantor set. At each of those intersections, the lifetime function diverges to infinity. An *edge point* is defined by the characteristic that along a sampling line, the edge point is a point in the saddle set that is also the endpoint of some interval of points in the laminar basin. In terms of the typical Cantor set construction, the *edge points* would be the endpoints of each of the removed intervals, and the *edge* is defined as the set of all edge points. To one side of the edge is an open set of points that lie in the laminar basin, while to the other side is an accumulation of points in the saddle set. We note that for moderately large Reynolds number, the saddle set is significantly more dense than the usual middle-thirds Cantor set. Consequently, the small intervals of smooth lifetime are difficult to discern. Figure 5.3 uses fine scale sampling to reveal small intervals of smooth lifetime, along with the associated edge points. Under this typical Cantor set geometry, we note that edge points along a sampling line will be countable, while the Cantor set itself is uncountable. Consequently, the edge is only a small part of the entire saddle.

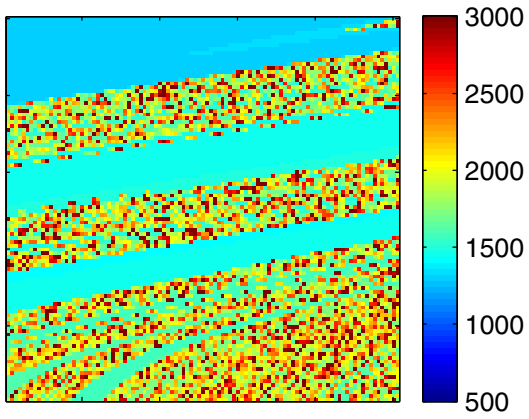

Figure 5.3: **Fine scale sampling of lifetime.** Lifetime $L(\boldsymbol{y})$, on a $10^{-6} \times 10^{-6}$ subset of a 2-d sample space. At fine scales, small intervals of smooth lifetimes are detectable, with edge points defining the ends of those intervals. ($Re = 420$.)

stable set was the set of all points that approached the saddle as $t \to \infty$. In this chapter, we focus only on the forward flow problem and have restricted our discussion to a forward chaotic invariant set — the stable set of the saddle. We simplify our terminology, and call this the saddle set.

Although we have used a sampling line to define the *edge* (and sampling can provide some insight and visualizations), a sampling approach will not be sufficient to discover underlying structure. There are two main drawbacks to sampling: (1) there are no dynamics associated with the sampled set, and (2) sampling will not be sufficiently dense (even in this moderate 9-dimensional model) to capture those dynamics. Bringing the dynamics back to the description of the set will be critical to understanding the structure. An important observation is that the *edge* is invariant under the dynamics, which we argue as follows: Consider a neighborhood of an edge point e. e lies on the boundary of an open set of points in the laminar basin. Under evolution of the flow, the trajectory of e will remain on the boundary of that open set of laminar basin points. Also in that neighborhood of the edge points is an uncountable infinity of points in the saddle set, which accumulate on e. Under evolution of the flow, for some fixed time, they must remain arbitrarily close. Consequently, any point on the trajectory of e must be an edge point, generating an *edge trajectory.* Our strategy is to analyze edge trajectories to reveal the structure of the invariant edge.

5.4 Approximation of edge trajectories

Because the *edge* is part of the saddle set, edge trajectories are unstable. Consequently, even if we resolve an edge point to machine precision, the numerical trajectory generated by standard ODE solvers can approximate the edge for only a short period of time. Therefore, we needed to develop specialized techniques that would allow us to generate arbitrarily long edge trajectories that would remain accurate, while maintaining computational efficiency. In this section, we describe those techniques in some detail because we believe they have wider application to a broad class of systems that exhibit transient chaos.

Resolving an edge point. Because the origin (laminar flow) is linearly stable and attracting, a region surrounding the origin is in the laminar basin. If we move outward from the origin along a radial direction until we intersect the saddle, there must be a "first" point along that line that has infinite lifetime, which will necessarily be an edge point. The issue is how do we efficiently find a numerical approximation to that point. By definition, the edge point separates smooth

lifetimes from discontinuous lifetimes, but identifying the precise edge of a fractal requires very fine sampling. Refinement to high numerical precision is computational expensive, and we find that it is difficult to implement a robust algorithm based on lifetime. The PIM-Triple method [19] is useful when phase space has only one expanding direction. However, for the moderate Reynolds numbers under consideration, the results of Chapter 4 indicate that the saddle has two expanding directions, and the algorithm is likely to fail.

If a system has two basins of attraction (call them A and B), a robust technique for finding points on the boundary is to find a point in basin A, and another point in basin B. By repeated bisection, always keeping an (A, B) pair, one can resolve a boundary point to required precision. In our model, there is a single attractor. To be able to apply bisection, we must identify some characteristic that allows us to assign a binary classification to each initial condition, where that binary classification is sufficient to determine that the edge lies between points of opposite classification. For the portion of the edge that is not too far from the origin, we apply the following logic to construct this classification: Points perturbed only slightly from the origin decay rapidly in energy, collapsing back to the laminar state. Consequently, those trajectories stay small in amplitude. However, if the perturbation is large enough to cross the edge, then that trajectory will exhibit a chaotic transient. The chaotic saddle (turbulence) is far from the laminar state. Consequently, a chaotic transient is characterized by having at least one high amplitude ($O(1)$) excursion. We define a maximum amplitude function, $A_{\max} : \mathbb{R}^9 \mapsto \mathbb{R}$ by

$$A_{\max}(\boldsymbol{y}) := \max_{t \geq 0} \|\phi^t(\boldsymbol{y})\|. \tag{5.2}$$

We classify an initial condition $\boldsymbol{y}$ as being either on the *high-side* or the *low-side* based on whether $A_{\max}(\boldsymbol{y})$ is above or below an appropriately chosen threshold value. Figure 5.4 compares the visualization of the edge using maximum amplitude and lifetime. Because the difference in amplitude from high-side to low-side is so large, it is not necessary to compute $A_{\max}$ very precisely. Therefore, we can compute a trajectory using our normal numerical integration techniques, then find an approximate maximum from the discrete time step output. Consequently, in implementation, finding $A_{\max}(\boldsymbol{y})$ adds almost no computation time to simply computing the trajectory.

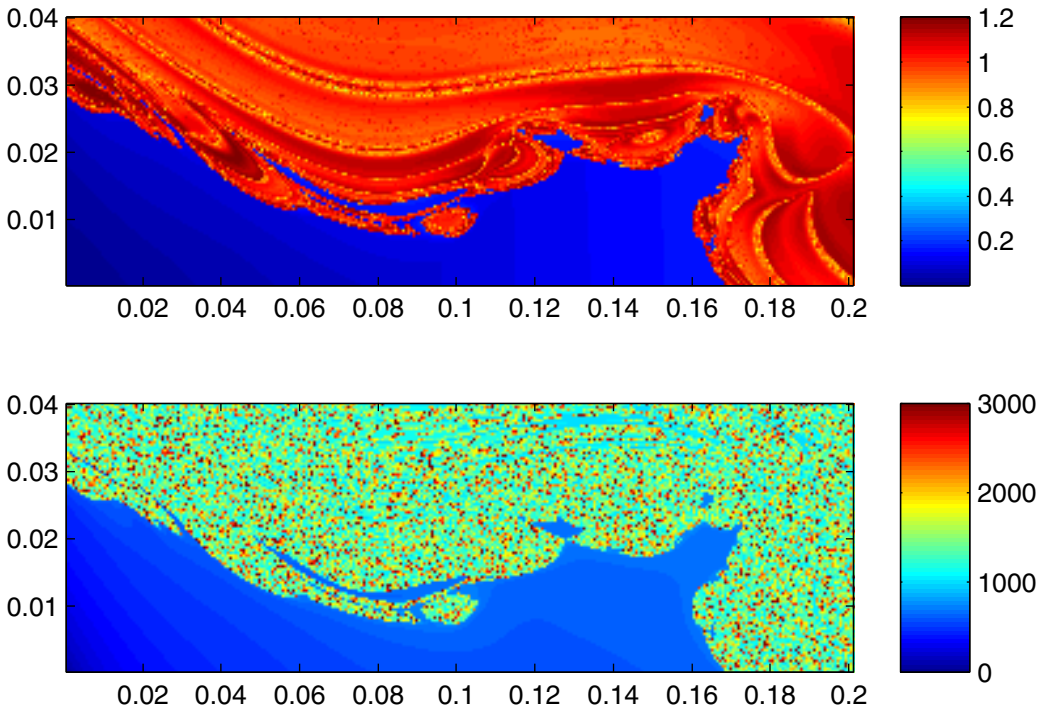

Figure 5.4: **Maximum Amplitude compared with Lifetime.** (Top) $A_{\max}(\boldsymbol{y})$ and (bottom) $L(\boldsymbol{y})$ are computed over the same 2-d subspace of sample points. Each block is colored based on the computed value for the center coordinate. At this scale, both characteristics provide adequate information to describe the edge, though maximum amplitude provides a sharper visual distinction. (Parameter $Re = 420$)

From Fig 5.4, one might conjecture that the maximum amplitude construct is not required, and that *lifetime* could be used to provide the binary classification. However, $A_{\max}$ provides the following significant advantages:

- Since lifetime approaches infinity as we approach the edge from either side, a precise edge classification using $L(\boldsymbol{y})$ requires that we determine if the neighborhood of $\boldsymbol{y}$ has fractal lifetime structure. However, $A_{\max}(\boldsymbol{y})$ can be classified as "high" or "low" without computing any other trajectories.

- The discontinuity in $A_{\max}$ at the edge is sharp and unambiguous, and therefore, it is easy to

implement code that detects the edge using amplitude.

- Although at the rough scale, it appears that a lifetime threshold would provide similar classification as is done with amplitude, at fine resolution, the threshold criteria may fail to give a correct classification, because points on the low-side of the edge may have arbitrarily large lifetimes, while those on the high-side may have exhibit relatively short transients. Figure 5.5 compares the effectiveness of L and $A_{\max}$ at distinguishing the edge, illustrating the superiority of maximum amplitude.

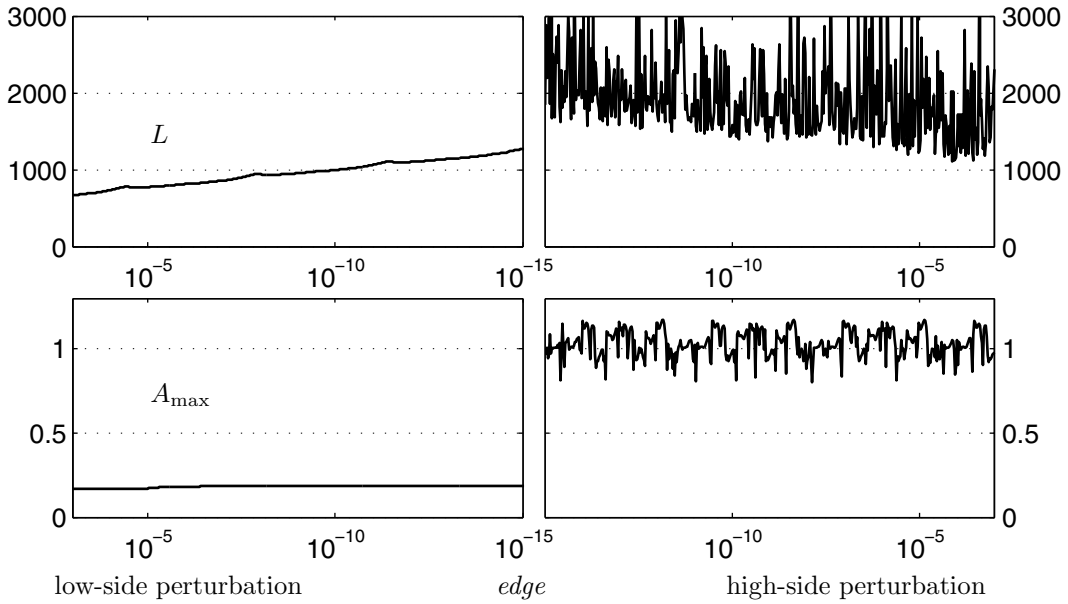

Figure 5.5: **Comparison of L and $A_{\max}$ for edge detection.** The upper pair of graphs plot lifetime L, and the bottom pair of graphs show $A_{\max}$ as a function of distance from the edge. The x-axis is on a log scale, with high-side perturbations to the right, low-side to the left, with the edge in the middle. (top-pair) If one tries to classify based on a threshold value for lifetime, any threshold value that properly classifies the low-side will improperly classify some nearby points on the high-side. (bottom) $A_{\max}$ provides a clear discontinuity at the edge, with no ambiguous amplitudes on the high-side. A threshold amplitude of 0.4, for example, would properly classify all the points. Moreover, this discontinuity in amplitude is preserved to arbitrary precision.

Using this classification of *high* and *low,* we can apply a bisection routine and determine

an edge point to an accuracy limited only by numerical precision. Starting from an arbitrary pair of initial conditions, if one is a "high-side" point and the other is "low-side," we can use that pair to find an edge point. This technique has proven to be both robust and efficient in numerical implementation. We note that the sequence of approximations of the edge also provides a sequence of trajectories that converges uniformly on a finite time interval to an edge trajectory. Figure 5.6 illustrates how the bisection algorithm leads to an increasingly accurate representation of an edge trajectory.

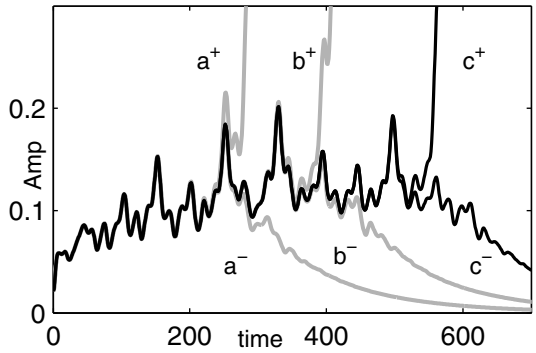

Figure 5.6: **High-side and low-side pairs.** Trajectory amplitude as a function of time plotted for three pairs of nearby initial conditions. Trajectories labeled "-" are on the *low-side,* and those with "+" on the *high-side.* The initial conditions for the "a" pair were separated by $\approx 10^{-7}$. The pairs "b" and "c" result from refining the "a" pair (using bisection) to separations of $\approx 10^{-10}$ and $\approx 10^{-13}$, respectively. The limit of the bisection algorithm (in infinite precision) would yield a trajectory which would remain bounded away from the origin, but would never achieve a large amplitude typical of chaotic transients. The data shown is for $Re = 390$.

Because the edge is unstable, even when the edge point is refined to machine precision, its trajectory will move far from the edge, with the approximation typically being accurate for only a few hundred time steps. To approximate a long strategy, we apply a techniques similar to those employed in [19]. Starting with an initial high-side/low-side pair (denoted $\boldsymbol{y}_0^+$ and $\boldsymbol{y}_0^-$) that are very close (to some tolerance $\epsilon_i \ll 1$), we evolve the trajectory of both points for some fixed period

T, and approximate the edge trajectory as the pointwise average on the time interval $[0, T]$. The resultant points $\phi^T(\boldsymbol{y}_0^+)$ and $\phi^T(\boldsymbol{y}_0^-)$ must also be a high-side/low-side pair. T can be selected sufficiently small such that for tolerance ϵ_f with $1 >> \epsilon_f > \epsilon_i$ the pair remain within a distance ϵ_f throughout the interval $[0, T]$. This pair is then refined using bisection to yield a high/low pair denoted $\boldsymbol{y}_1^+$ and $\boldsymbol{y}_1^-$, with $\|\boldsymbol{y}_1^+ - \boldsymbol{y}_1^-\| \leq \epsilon_i$. This process can be continued indefinitely, producing a numeral approximation to an edge trajectory. Because the edge is always between the pair of high/low trajectories, the approximation of the edge remains accurate to within ϵ_f. Figure 5.7 gives a graphical illustration of this procedure.

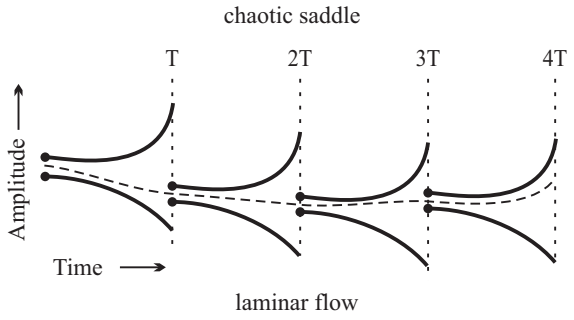

Figure 5.7: **Numerical edge trajectory.** At time 0, we start with two nearby initial conditions, one on each side of the edge. As the trajectories evolve, they are repelled from the edge, and we begin to lose precision in our approximation. At time T, before the error grows large, we use bisection to find a new pair of nearby initial conditions that are closer to the edge. By controlling refinement precision and interval T, we ensure the approximation maintains desired accuracy throughout the trajectory.

The focus of this section has been to provide a thorough explanation of our technique for computing edge trajectories. Because the method relies on an amplitude threshold, its utility is restricted to that portion of the edge that is not too far removed from the origin. In application to our model of plane Couette flow, we find that even this limited range of applicability is sufficient to resolve the structure of the edge. We have successfully applied these techniques to other dynamical systems with chaotic saddles, and they have proven to be a robust tool for identifying invariant structures that lie on the *edge*. Consequently, we feel that the technique itself is a valuable

contribution to the study of transient chaos. However, we also recognize that the method is a *tool.* In the following sections, we focus on applying that tool to improve our understanding of the *edge* in our model of plane Couette flow.

5.5 Structure from edge trajectories

In the very simplest of dynamical systems used to study shear flows, such as the two and four dimensional systems of [20] and [12], the boundary of the laminar basin is the stable manifold of a stationary point. As the model is enhanced by adding additional modes, the dynamics are enhanced by a rich bifurcation structure [10]. The boundary of the laminar basin evolves into a chaotic saddle with fractal dimension and is no longer a simple manifold. Although the entire boundary is a fractal set, we have identified the *edge* as an invariant subset of that saddle, with the special property that those points are precisely where an interval of laminar basin points touches the saddle. In order to resolve the structure of the edge, we will study the dynamical properties of that invariant set by studying **edge trajectories.** In this section, we focus on a relatively narrow region of parameter space, restricting ourselves primarily to the range $380 \leq Re \leq 420$, where we have performed the bulk of the numerical experimentation.

[Note: although the edge is invariant, it is repelling. Consequently, the tools described in the previous section are essential to the numerical calculation of edge trajectory. However, the specifics of how we find the trajectories are not relevant to the observations about the dynamics. Therefore, in this section, we make an *a priori* assumption that the trajectories reflect actual trajectories on the invariant set, with no need to discuss the approximating algorithms.]

Periodic structure on the edge — $380 \leq Re \lessapprox 402$. For this range of the parameter, we find that a typical edge trajectory is asymptotically periodic. Our primary tool for classifying these trajectories is a Poincare surface of section applied to an edge trajectory, which reveals that edge trajectories converge rapidly to a periodic orbit. We denote this periodic orbit of the flow as p^+. Due to a symmetry in the system, periodic orbits must occur in pairs, and we denote the symmetry orbit as p^-. Figure 5.8 illustrates the complexity of these periodic orbits. Analysis of

these periodic orbits indicate that they are unstable in only one direction, with an 8-dimensional stable manifold, which we denote $W^s_{p^+}$ and $W^s_{p^-}$. In a 9-dimensional phase space, these manifold are surfaces. We associate the single unstable direction with the repelling action of the edge. Since we are focusing on the restriction of the dynamics to the edge, we use the term *relatively stable* to indicate that these periodic orbits are stable with respect to flow on the invariant set. We remark

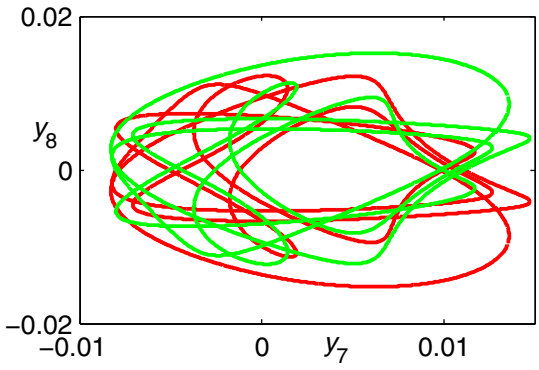

Figure 5.8: **Periodic orbit pair for** $Re = 390$, graphed by plotting the y_7 and y_8 components over one period. Edge trajectories will asymptotically approach either the red or the green orbit.

that the characteristic exponents of this periodic orbit are very different from those calculated for the entire saddle set. For example, at $Re = 390$, the three largest Lyapunov exponents for the periodic orbit are $0.048, 0, -0.005$, while for the chaotic saddle (using the techniques of Chapter 4), the leading exponents are $0.021, 0.003, 0$.

We say that these orbits p^+ and p^- are *relative attractors* to indicate that although they are unstable in the direction transverse to the edge, they attract nearby edge trajectories. While it is impossible to perform an exhaustive search of phase space, we note that in this parameter range where the edge periodic orbit has an 8-dimensional stable manifold, all numerical edge trajectories asymptotically approach either p^+ or p^-. Similar results for planar maps are discussed in [17]. However, the high dimensionality of these models permits other behavior.

As the Reynolds number is increased toward $Re = 402$, the Poincare maps indicate that the edge periodic orbits undergo period-doubling and period-halving bifurcations of the relative

attractor. When a period-one orbit bifurcates to a period-two orbit, the period-one orbit remains an edge trajectory, but the dimension of its stable manifold is reduced by one. However, the newly emerging orbits have an 8-dimensional stable manifold and becomes the relative attractor. In our terminology, the emerging period-2 orbit would be designated the p^+ orbit and is relatively stable.

Using continuation methods, we are able to follow the period-1 orbit as we vary Re through the bifurcation as it becomes unstable in two directions. We find that despite the additional instability, the orbit remains on the edge. We say that the period-1 is now *relatively unstable* to indicate that it repels nearby edge trajectories, and remark that while this orbit has two unstable directions, one is transverse to the edge, while the other is tangent to the edge. We conjecture that while the essential part of the edge is formed by the union of the 8-dimensional surfaces $W^s_{p^+}$ and $W^s_{p^-}$, the edge is also embedded with the stable manifold of some number of relatively unstable periodic orbits. A partial bifurcation diagram of observed orbits is provided in Fig 5.9. We note that other periodic orbits may exist on the edge, but they are not detected because they never achieve an 8-dimensional stable manifold.

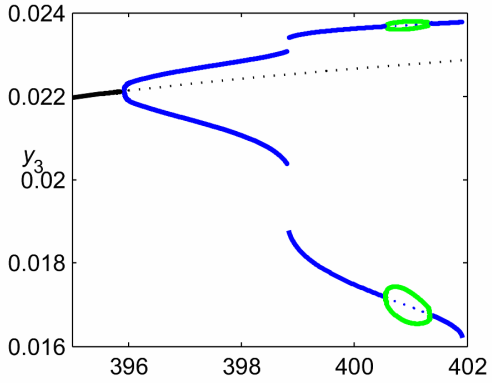

Figure 5.9: **Partial bifurcations diagram.** The y_3 component at the crossing of the Poincare surface of section is plotted vs Re for the observed periodic orbits. Period-1 is plotted in black, period-2 in blue, and period-4 in green. The dotted portions are show were those orbits are relatively unstable. The discontinuity in the period-2 is indicates our inability to resolve specific behavior.

Chaos on the edge — $Re \gtrapprox 402$. At $Re \approx 402$, the relatively stable periodic orbit loses stability in a saddle-node bifurcation. Consequently, it is not replaced by a periodic relative attractor. We denote this critical value of the parameter as Re_c. For $Re > Re_c$ (to the top of the parameter range studied, $Re = 420$), although there are relatively unstable periodic orbits on the edge, there are no periodic orbits with 8-dimensional stable manifold to form the edge. However, we note that as an invariant set in phase-space, the edge continues to persist as a structure and it appears to vary continuously as we move through both the periodic parameter range ($Re < Re_c$) and the new regime ($Re > Re_c$). Figure 5.10 illustrates this structural robustness as viewed by 2-dimensional sampling.

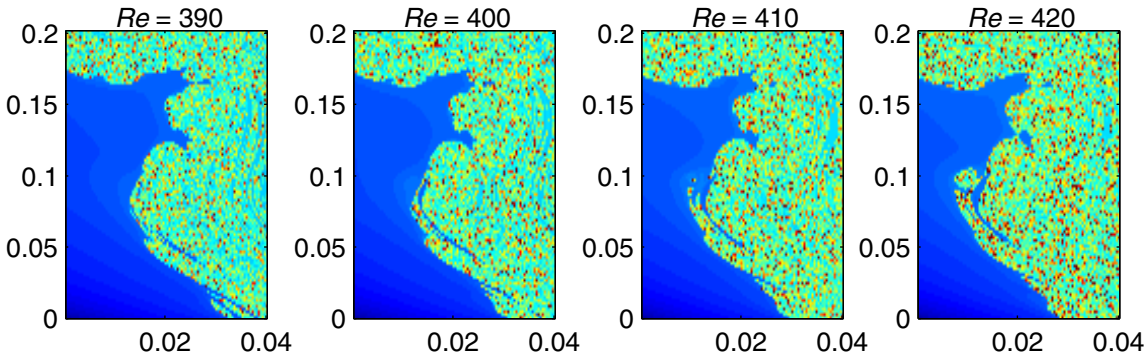

Figure 5.10: **The edge structure is robust.** The lifetime function, plotted on the same sample set, for $Re = 390, 400, 410, 420$. Despite the bifurcations of the relative attractor, the edge appears to vary smoothly with changing Reynolds numbers.

Our numerical experimentation indicates that after the bifurcation at Re_c, the invariant saddle object appears to be a union of surfaces that are smooth deformations of $W^s_{p^+}$ and $W^s_{p^+}$, the stable manifold of the relatively attracting periodic orbits that existed just prior to the bifurcation. Analysis of edge trajectories indicate that they are chaotic, with two positive Lyapunov exponents. We conjecture that the leading Lyapunov exponent can be associated with the repelling action away from the edge, while the second Lyapunov exponent is responsible for the chaotic motion of trajectories on the edge. Table 5.1 provides some comparative data of leading Lyapunov exponents

of various invariant sets at $Re = 420$.

Invariant set	λ_1	λ_2	λ_3	λ_4
Period-1 orbit	0.094	0.008	0	−0.008
Edge orbit	0.045	0.012	0	−0.007
System saddle	0.021	0.004	0	−0.011

Table 5.1: **Comparison of Lyapunov exponents for invariant sets at** $Re = 420$. The period-1 orbit is one of the low period orbits embedded in the relative attractor on the edge, and the exponents of the relative attractor are very close to those of the periodic orbit. However, the exponents of the relative attractor are vastly different from those of the system saddle because typical chaotic transients visit near that attractor very infrequently.

Edge trajectories now converge to a more complicated, chaotic set, which we call a *relative chaotic attractor.* Figure 5.11 provides a visualization of this more complex, higher dimensional structure, by plotting coordinates of the Poincare return map. We note that a periodic edge orbit would generate a finite set of discrete points, and quasiperiodic motion would generate a 1-d line of points on the plot of the return map. Although the graph shows high density regions that appear to be a nearly simple curve, their are many regions of the plot that show significant thickening. We find that the thin portions of the plot of Fig 5.11 can be associated with relatively unstable periodic edge orbits. Those orbits are only weakly repelling, so trajectories tend to shadow those periodic orbits for long periods of time before being pushed to another part of the relative attractor. The symmetry in the graph of Fig 5.11 seems to indicate that if periodic orbit Γ^+ is embedded in the relative attractor, then its symmetry pair, Γ^- is also embedded, implying a heteroclinic intersection of stable and unstable manifolds of at least one of these symmetry pairs.

If we assume that the leading Lyapunov exponent of the chaotic edge trajectory (denoted λ_1) is a direct indication of the repelling action of the edge, then we can determine the dimension of the relative attractor using the formulation of [14], because the *decay time* for the chaotic invariant set (the rate at which measure leaves the neighborhood of the edge) would be given by $\tau = 1/\lambda_1$.

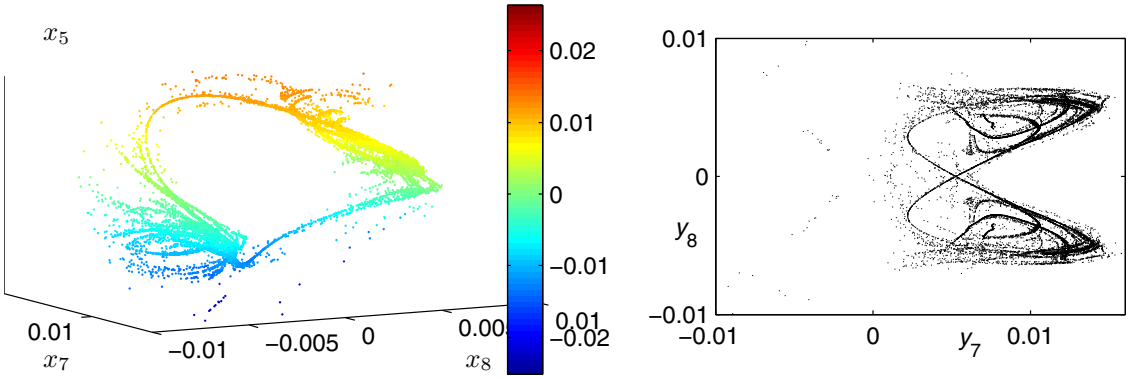

Figure 5.11: **Relative chaotic attractor at** $Re = 420$. Using points from a Poincare surface of section, to the left we plot (y_7, y_8, y_5) colored by y_5. On the right is the same data, plotted in the $x_7 - x_8$ plane, which better illustrates the symmetry. The relatively thin line of points that cross from one side of the symmetry to the other indicate the path along the unstable manifold that creates the heteroclinic intersection.

Under these assumptions, $D_1 \approx 3.8$ at $Re = 420$.

5.6 Initial studies at low Reynolds numbers

The majority of our numerical experimentation has focused on a range of moderately large Reynolds number, where the model indicates a robust transient turbulence behavior. Additionally, we have begun initial studies with small Reynolds numbers to see how edge analysis techniques might provide insight into the conditions which support the onset of the transient turbulence behavior. Our experimental approach is to choose a random unit vector $\boldsymbol{v}$, and then study the behavior of trajectories of $\boldsymbol{y} = \gamma \boldsymbol{v}$ over two parameters — Reynolds number Re and perturbation amplitude γ — for a fixed $\boldsymbol{v}$. Figure 5.12 shows maximum amplitude data, for a typical data set.

We use the maximum amplitude of a trajectory to determine if the initial condition is on the "high-side" or the "low-side" of the edge, where we expect a discontinuity at the edge. Below $Re \approx 130$, there appears to be no discontinuity as we increase the amplitude of the perturbation. We note that [10] reported that the first periodic orbits formed at approximately this value of

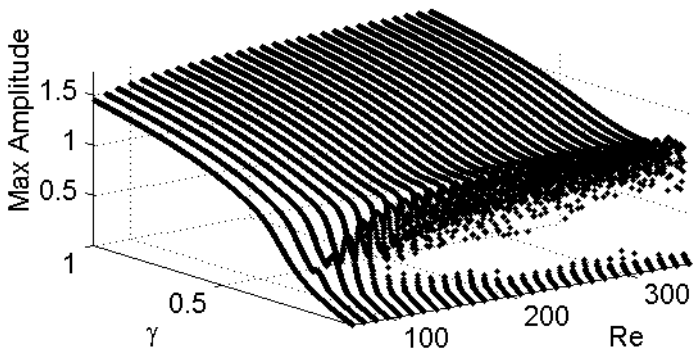

Figure 5.12: **The edge at low Reynolds number — Maximum Amplitude.** Using a fixed unit vector $\boldsymbol{v}$ we plot maximum amplitude for 1000 discrete perturbation $\gamma\boldsymbol{v}$ for $70 \leq Re \leq 350$. The first crossing of the edge (moving from the laminar origin) is indicated by a discontinuity in the Maximum amplitude function. The discontinuity appears to persist down to about $Re \approx 130$.

Reynolds number. We conjecture that the first appearance of chaotic transients occurs when this periodic orbit is formed. Using data from the same set of initial conditions as the Maximum amplitude plot of Fig. 5.12 , we see that for $Re < 130$, the lifetime function appears to be a smooth, without evidence of long transients or fractal structure (Fig. 5.13).

As we reduce the Reynolds number, we find that the edge moves continuously with the change in parameter. However, the regions of smooth lifetime begin to grow dramatically. The regions of phase space that contain the saddle set become very thin, making it increasingly difficult to "find" a chaotic transient under an arbitrary perturbation. Figure 5.14 illustrates this thinning of the saddle set. Although only partial analysis is complete, we note that while the relative attractor at $Re = 150$ is a periodic orbit, a chaotic relative attractor is detected at $Re = 250$. Additional work will be required to understand the precise route to chaos in those windows of the parameter value that yield a chaotic relative attractor.

5.7 How are transients able to decay

Folds in the envelope. For all Reynolds numbers considered, the edge appears (at least locally)

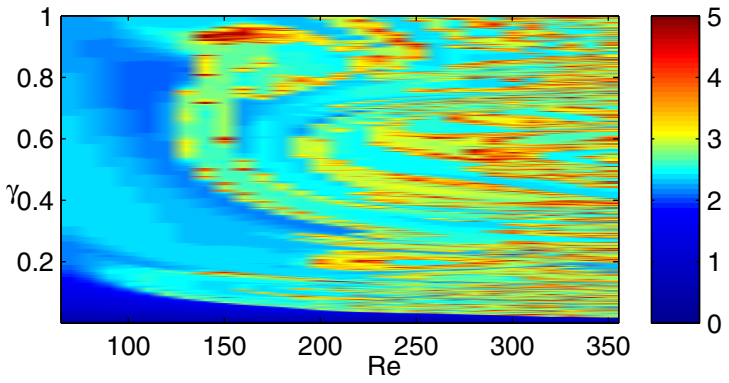

Figure 5.13: **The edge at low Reynolds number — Lifetimes.** In this plot, the horizontal axes is Re, while the vertical is perturbation amplitude γ. (The initial conditions y are identical to those of Fig 5.12.) We color this plot according to $L(y)/Re$. (Normalizing by Reynolds number removes the linear affects that the parameter Re has on lifetime.) The dark blue region is the low side of the edge. Below $Re \approx 130.$, lifetimes vary smoothly, with no long lived transients, and therefore, there is no longer an edge.

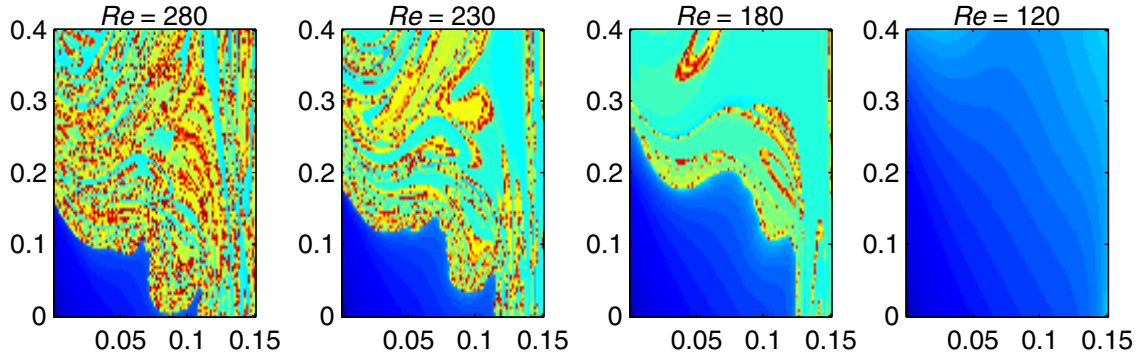

Figure 5.14: **Thinning of the saddle at small** Re. Lifetimes (normalized for Re) are plotted over a two-dimensional sample set at four values of Re. The saddle set is detectable in a large fraction of the phase space at $Re = 280$. As Re decreases, the area containing the saddle set gets increasingly smaller. At $Re = 180$, the majority of phase space beyond the edge lies in a region of smooth lifetimes (the light blue field). At $Re = 120$, there is no indication of an edge.

to be a smooth, 8-dimensional surface, which could, therefore, separate phase space. Additionally, we find that any line through the origin will cross the edge, with the exception of lines that fall in the invariant 4-dimensional symmetry subspace of the system. Therefore, no matter what direction we move from the laminar state, we find the edge. A reasonable question, then, is: "How do chaotic transient (*high-side* trajectories) return to the origin (the *low side*)?" As a restatement of the question, we can ask: "If we start from the origin, and move outward until we cross the edge, how can we have a transient return to the origin (re-crossing the edge) if the edge is invariant?" Part of the reason that this question is difficult to resolve intuitively is that we tend to focus on the idea that the edge bounds a region of smooth lifetime. Our edge detection scheme (based on amplitude) detects only the first crossing of the edge. However, on the other side of the edge point lies a fractal structure of infinite lifetime points. Consequently, within any arbitrarily small distance after first crossing the edge, there is an infinity of edge crossings. Although it is reasonable to view the edge as locally providing a separation, this intuitive view cannot be extended globally. The edge does create a separation of phase space — it separates the almost everywhere laminar basin from the Lebesgue measure-0 saddle set.

Despite our intuitive difficulties, it is still reasonable to address the questions posed in the above paragraph. For ease of explanation, we focus on the case where the relative attractor is periodic. Then the edge is composed of two symmetric parts, but they are folded and intertwined in a complex fashion, and there is space between the folds that provide a path to the origin. We conjecture that for every basin point, we can find a line segments lying entirely in the laminar basin such that one endpoint of the segment lies on $W^s_{p^+}$ and the other lies on $W^s_{p^-}$. Fig 5.15 illustrates how a "dying" transient weaves around the edge as it returns to the laminar state. In essence, a transient trajectory does not need to "cross" the edge because it lies in a region that is between the two "parts" of the edge. Although the trajectory may follow a circuitous path, its neighborhood will always remain "between" the edge parts until it eventually reaches the origin.

As an alternative view, we may focus on the basin itself, instead of transient trajectories. Consider the small ball of initial conditions B_ϵ around the origin that defines states whose lifetime

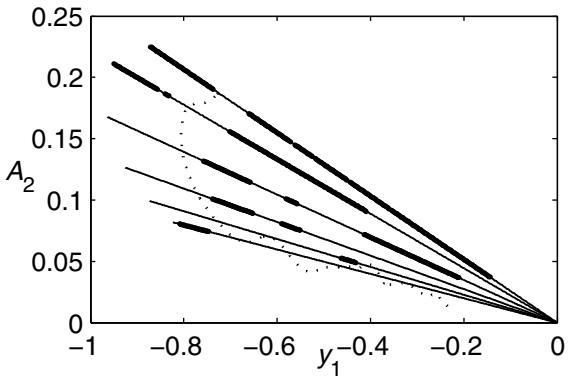

Figure 5.15: **Terminal stages of a chaotic transient.** The dotted line shows the trajectory of a chaotic transient from the time it begins its final relaxation to the origin. At several points along the trajectory we have computed the lifetime function along the direction in phase space that points to the trajectory. The bolded portions of those lines show regions where the lifetime function is fractal, while the unbolded portions lie entirely in the laminar basin. The "dying" transient weaves around the folds, always remaining in a region that lies in the laminar basin. The projection coordinate (vertical) for this figure is defined by $A_2 = \sqrt{\sum_{i=2}^{9} y_i^2}$. Data shown is for $Re = 390$.

is 0. If we "grow" that ball by evolving that volume backward in time, we remain in the laminar basin, but the evolved set will include points of increasing lifetime. (Figure 5.16 provides a cartoon drawing of this process.) Initially, near the origin, phase space expands in all directions as we evolve backward in time. However, as the boundary of the evolved ball approaches the edge, the one positive Lyapunov exponent of the edge means that phase space will contract in one direction under time reversal. We note that the system is dissipative, so although there is contraction in one direction, the local phase space volume is expanding. As we continue to push backward in time, the boundary of the ball becomes squeezed between the two manifolds that create the edge, growing exponentially thin in that contracting direction.

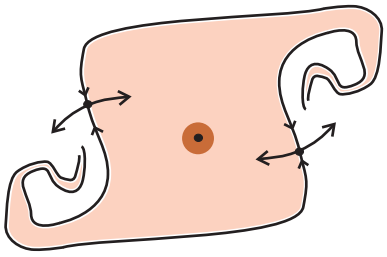

Figure 5.16: **Cartoon: Laminar basin expands between the edges.** If we evolve an ϵ ball of the origin backward in time, it expands to the edge (as $t \to \infty$.) This region of the laminar basin lies between the two symmetric parts of the edge. As drawn, it shows that under evolution, the boundary of the ball begins to shrink in at least one direction, and the distance between $W^s_{p^+}$ and $W^s_{p^-}$ gets smaller. However, the volume of the evolved ball will continue to grow and will fill almost all of phase space.

5.8 The edge in the Horseshoe Map.

In our model of plane Couette flow, the edge plays a significant physical role in that (near the origin) it separates the nearly laminar states from the transient turbulence. Our expectation is that a similar behavior will persist in higher dimensional models, including full numerical simulations. That expectation is based (in part) on the role that the horseshoe plays in chaotic dynamics. In this section, we discuss the edge in a horseshoe map and prove that its edge is the stable manifold of a fixed point.

To simplify the explanation, we consider a construct which Smale called the *reduced horseshoe* [30]. We start with the standard Horseshoe map $M(x)$ (Fig 5.17a), acting on the rectangular region B. To generate the reduced horseshoe, we proceed as follows: If we were to shrink box B from the left, then $M(B)$ gets thinner, but it also gets close to the left edge of B. Consequently, we can shrink from the left until we find box B' such that the left side of $M(B')$ exactly coincides with the left edge of B'. Similarly, we can shrink from the right, top, and bottom to create box B'' whose image $M(B'')$ reaches exactly to the bottom and right edges of B''. By rescaling, we can define the reduced horseshoe to be the map on the unit square. For ease of notation, we assume that we simply redefine M to be the reduced horseshoe. The map is shown graphically in Fig 5.17b, with inverse in Fig 5.17c.

As is typical, we define the lifetime of a point $\boldsymbol{x} \in B$ to be the time that the trajectory of $\boldsymbol{x}$ first leaves B. Almost every initial condition has a finite lifetime. The points of infinite lifetime lie on a Cantor set of horizontal lines, which form the *saddle set* for this map. We note that the origin is a fixed point, which immediately implies that it has infinite lifetime. Its local stable manifold falls along the horizontal axis. To construct the global stable manifold, we take inverse images of the local stable manifold, as illustrated in Fig 5.18a.

Let $M(x)$ be the reduced horseshoe map on the unit square B. The set $B \cap M^{-1}(B)$ is composed of two horizontal rectangles. Denote the lower rectangle as H_0 and the upper as H_1 (See Fig 5.18b). We denote by λ the vertical expansion rate of M, which implies that the vertical height of these rectangles is $1/\lambda$.

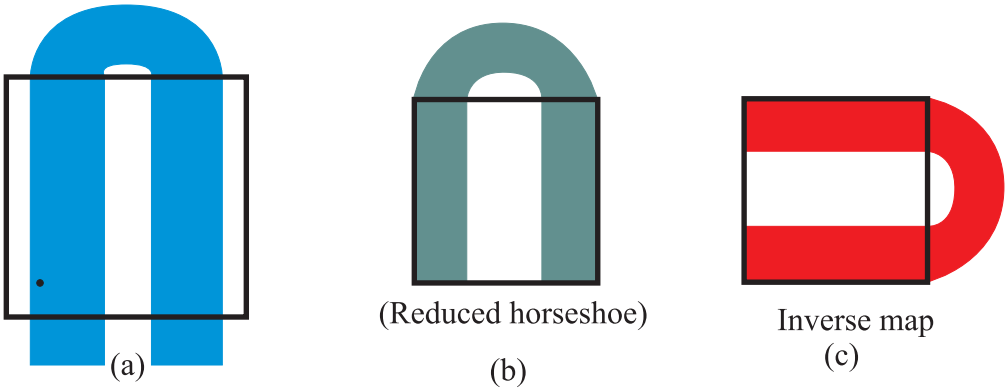

Figure 5.17: **The reduced horseshoe map.** (a) The standard horseshoe map, with saddle fixed point in the lower left portion; (b) the reduced horseshoe map; (c) the inverse of the reduced horseshoe.

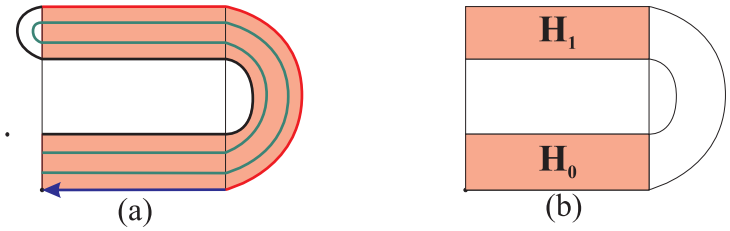

Figure 5.18: **Stable manifold and symbol dynamics for the horseshoe map.** (a) The local stable manifold (blue) is imaged under M^{-1} to produce the global stable manifold. The first three iterates (red, black, and green) are shown in this figure. (b) Rectangles H_0 and H_1, used to assign symbol dynamics, are bounded by the stable manifold.

As preliminary material, we define a symbol dynamics in the usual way: For each $x \in H_0 \cup H_1$, we consider the possibly bi-infinite sequence $S_x := \{\ldots, M^{-2}(x), M^{-1}(x), x, M(x), M^2(x), \ldots\}$, where M^k is the k times composition of M for $k > 0$, and the k times composition of the inverse function for $k < 0$. The sequence is terminated to the right at the smallest integer $k \geq 0$ such that $M^{k+1} \notin H_0 \cup H_1$, and terminates to the left at the largest $j \leq 0$ such that $M^{j-1} \notin H_0 \cup H_1$. Then to S_x we can associate a symbol sequence $\sigma_x := \ldots a_{-2}a_{-1}.a_0a_1a_2\ldots$, where $a_i := 0$ if $M^i(x) \in H_0$, and $a_i := 1$ if $M^i(x) \in H_1$. We call $.a_0a_1a_2\ldots$ the *forward sequence.*

We make the following observations about symbol sequences of the horseshoe map:

- The symbol dynamics associated with the horseshoe is a full shift on two symbols.
- A bi-infinite sequence would indicate that x is a point on the forward and reverse time invariant set — the chaotic saddle. Since the edge is defined from forward lifetimes, we focus on points in the stable set of the saddle, which requires that they remain in B for all forward iterates. These sequences are of the form $X.Y$, where X is a symbol sequence of arbitrary length, and Y is of infinite length. We call $.Y$ the forward sequence.
- Because M is contracting in the horizontal direction, all points on a horizontal line in B will have the same forward sequence, and our terminology is to denote that horizontal line by its forward sequence.
- The fixed point at the origin generates the symbol sequence $\ldots 00.00 \ldots$.
- Any point on the horizontal axis in B will have a sequence forward sequence $.00 \ldots$.
- Any point on the stable manifold of this fixed point will have a forward sequence of the form $.Y00 \ldots$, with Y a finite arbitrary sequence.
- The horizontal line at the top of H_0 is composed of points with forward sequences $.01\ 00 \ldots$.
- The bottom and top of H_1 contains points whose forward sequences are of the form $.11\ 00 \ldots$ and $.10\ 00 \ldots$ respectively.
- Two horizontal lines of the form $.YZ_1$ and $.YZ_2$ are separated vertically by no more than $1/\lambda^r$, where r is the length of sequence Y.

Theorem 5.1. *The edge of the reduced horseshoe map is the stable manifold of the fixed point at origin,* W_0^s.

Proof. We break this proof into two parts. First, we show that the stable manifold of the origin must lie on the edge. Secondly, we show that no other points in the stable set can be edge points.

Part 1: Denote by B_H the set of all points in B that are not in $H_0 \cup H_1$. B_H is the rectangle that lies between H_0 and H_1. All the points in B_H leave B in one iterate, so B_H contains no points of the saddle set. Moving vertically from a point in B_H, the first discontinuity occurs as we cross the boundary of H_0 or H_1, which are part of W_0^s. Therefore, every point on the horizontal line sequence $.01\ 00\ldots$ lies on the edge. Because the edge is invariant, all forward and backward images of those points will lie on the edge, which will construct the entire stable manifold of the origin.

Part 2: Let $w := X.a_0a_1a_2\ldots$ be a right infinite sequence such that $w \notin W_0^s$. Then for each k, the horizontal lines $.a_0\ldots a_k\ 0\ 0\ldots$ and $.a_0\ldots a_k\ 1\ 0\ldots$ bound w from both above and below. As $k \to \infty$, these horizontal lines come arbitrarily close to each other and to w. Therefore, any non-horizontal line segment with w as an endpoint must intersect infinitely many of these horizontal lines. Therefore, w cannot be the endpoint of an interval of points with smooth lifetime. Consequently, w is not an edge point. □

We note that the argument above extends directly to the standard horseshoe map, where the edge is defined by the stable manifold of the fixed point with symbol sequence $\ldots 0.0\ldots$.

5.9 Smoothness of the edge

Our numerical studies throughout the parameter range seem to indicate that the edge is smooth. For those values of *Re* where the edge coincides with the stable manifold of a periodic orbit, the theory of ordinary differential equations ensures that the surface is smooth. As we slowly vary *Re* to a region where the relative attractor is chaotic, sampling suggests that the edge varies continuously with the change in the parameter, so we conjecture that it remains a smooth surface. Figure 5.10 illustrates this suggested continuous dependence on the parameter.

We conjecture that for this system, the edge is a smooth object. Although we cannot provide a rigorous argument, we have three lines of thought that provide some justification that this is a reasonable conjecture. These ideas also provide some insight into the more general question of what characteristics of a system might lead to a smooth edge, since we know that some systems

generate a fractal edge structure [31]. We emphasize that these ideas are not meant to *prove* that the edge in our system is smooth, but merely provide some idea of possible approaches that might lead to some rigorous conclusions.

- **A Hausdorff dimension based argument.** Suppose we have a chaotic saddle in some n-dimensional system. Furthermore, let us suppose that the saddle set S (the stable set of the saddle), with dimension D_s, is such that $n-1 < D_s < n$, implying that a general line l through phase space intersects S the saddle in a Cantor set. Let E be the set of edge points, and denote by E_l the edge points in $S \cap l$, the endpoints of the removed intervals of that Cantor set. As a countable set, E_l will have Hausdorff dimension 0. If we assume the E_l is representative of a general intersection of E with a line through phase space, then $\dim E_l = 0$ implies $\dim E \leq n-1$. On the other hand, since a general line through phase space has a non-empty intersection with the edge, we know $\dim E \geq n-1$. Consequently, we conclude that if these general intersections apply, then

$$\dim E = n - 1.$$

  We would infer from this dimension argument that the edge is not a fractal object. Researches have found that in typical dynamical systems, it is usually the case that the box counting dimension and the Hausdorff dimension are equivalent [32].

- **A D_1 dimension argument.** In our model of plane Couette flow, we found that when the relative attractor changes from a periodic orbit to a chaotic object, the leading Lyapunov exponent does not change very much and that the edge appears to move continuously through phase space. In the periodic situation, that leading exponent is the only one that is positive and represents the repelling action from the unstable edge object. If we assume that in the parameter range where the system is chaotic, the leading exponent remains associated with the repelling action away from the edge, then we can use the formulations of [14, 15, 22] to find the D_1 dimension of the edge, proceeding as follows: We treat the chaotic relative attractor as the chaotic saddle, and its stable set is the edge, E. Then the decay time, τ,

for this analysis would describe the rate at which nearby trajectories leave the neighborhood of the edge. If we assume that the leading Lyapunov exponent, λ_1, is associated with the repelling action that is transverse to the edge, then

$$1/\tau = \lambda_1.$$

As the most direct calculation, we apply the formulation of [15], and conclude that

$$\dim E = n - \frac{1}{\tau\lambda_1} = n - 1.$$

Again, this argument provides some evidence that the edge is a surface, but does not directly address the issue of smoothness.

- **Smoothness of the edge is a result of the strong repelling action.** It has been shown that in some dynamical systems, the edge is a fractal object [31, 33]. The authors consider the map

$$\begin{aligned} x_{n+1} &= \lambda_x x_n \bmod 1 \\ y_{n+1} &= \lambda_y y_n + \cos(2\pi x_n), \end{aligned}$$

with $\lambda_x > 1$ and $\lambda_y > 1$. For almost every initial condition, the trajectory diverges to either ∞ or $-\infty$ in the y component. However, there is an invariant set that remains bounded, and this separating curve can be described analytically as a function of x. The authors show that if $\lambda_y > \lambda_x$, the curve is smooth, while if $\lambda_x > \lambda_y$, the curve is continuous, but nowhere differentiable.

We conjecture that a similar condition should hold in higher dimensions. Specifically, if phase space is expanding away from the edge at a rate that is bounded below by some value $\lambda_\perp$, and the expansion rate of phase space tangent to the edge is bounded above by λ_t, then the edge will be smooth as long as

$$\lambda_\perp > \lambda_t.$$

5.10 Concluding remarks.

The edge of chaos described here is significant for issues such as control of turbulence. In particular, if the goal is to prevent a turbulent transient, then the ability to describe the portion of the edge that it nearest the origin is of crucial physical importance. The fact that almost every point is in the laminar basin is of little practical utility. Once the system is perturbed beyond the edge, it will undergo a large amplitude transient. From an engineering perspective, knowing the location of the edge allows the system designer to design a control system that will prevent the large excursions. If it is possible to prevent the approach to the edge, the laminar profile can be kept stable. Similarly, if one wants to re-laminarize a turbulent flow using small perturbations, understanding the edge structure might allow for efficient targeting of a portion of phase space that allows rapid decay to the origin. We expect that the edge structure will be detectable in high-dimensional models, including full scale simulation. Additionally, we believe that in other systems with robust transient chaos, one should be able to find the edge in these systems, and the edge will have similar physical significance in efforts to control these systems.

Chapter 6

Many fixed points

6.1 Introduction

Chaotic transients have become an important part of the field of dynamical systems because they often arise in higher dimensional models of physical phenomena. Such transient behavior indicates the presence of a *chaotic saddle.* Because these saddle invariant sets are unstable, they are difficult to study without specialized algorithms [19, 25, 13, 18] that allow the computation of long trajectories near the saddle. These long trajectories can then be analyzed with techniques that are similar to the ones that are routinely used to study chaotic attractors. In application and demonstration of these algorithms, most of the work has focused on low dimensional systems. In concept, the techniques may be applied to higher dimensional systems, but we find little demonstration of that application in the literature, particular in the case where the saddle is hyperchaotic (multiple positive Lyapunov exponents).

Our goal was to find a system with a chaotic saddle with a large number of positive Lyapunov exponents to truly challenge these algorithms. The system selected was a slight modification to the Lorenz 40-variable model of the weather [34], where we replace an affine term with a cubic $f(x_i)$, which we associate with the forcing of the system:

$$\dot{x}_i = x_{i-1}x_{i+1} - x_{i-1}x_{i-2} - \underbrace{x_i(x_i - a)(x_i - b)}_{f(x_i)}, \qquad i = 1, \ldots, n, \tag{6.1}$$

By controlling parameter values a and b, we have been able to study chaotic saddles whose number of positive Lyapunov exponents can be as large as about $n/4$.

A very interesting structure arises in this system because there are a large number of fixed points that are associated with 0's of $f(x_i)$. The number of fixed points grows exponentially with the size of the system (for $n = 40$, there are more than 5×10^{10} fixed points, and about 5×10^7 of those are stable). Consequently the attractor for the system, though not a strange attractor, is

still a very complex set.

The complexity of the attractor causes a computational difficulty for the standard approaches to analyzing chaotic saddles. Those techniques rely upon finding a set A which contains the saddle but excludes the attractor. The *lifetime* of a trajectory is computable for each point in A by determining how long before the trajectory leaves the set. However, for the large number of stable fixed points for this system, the algorithmic step of identifying this stopping point would be computationally impractical. Therefore, we develop an alternate technique for assigning a lifetime value to each point that is based on finite time Lyapunov exponents. The technique appears to be broadly applicable to problems where the attractor cannot be easily described.

The primary advantages of the lifetime function defined in this chapter are:

- Lifetime is based on behavior near the chaotic saddle. Consequently, it can provide an accurate representation of the location of the saddle in phase space directly from the lifetime computation.
- Multiple attractors, including periodic orbits, have no effect on the computational effort required to compute lifetimes.
- It requires no knowledge of the number or type of attractors of the system, as long as the attractors are not chaotic.
- It requires no knowledge of the basins of attraction for the attractors in the system.

We believe that as the study of chaotic saddles is pushed to analyze higher dimensional systems, it may become too difficult to perform the necessary analysis to define a lifetime function in the standard way. The method described in this chapter provides a means to study these more complex, high dimensional saddle structures.

This chapter is organized as follows: in Section 2, we formally describe the system and provide some basic analysis to describe the general behavior of the system. In Section 3, we provide detailed analysis of the attractor structure of the system. Sections 4 develops the theory of our new lifetime function, and in Section 5 we develop an algorithm that provides a computable

implementation. In Section 6, we provide some numerical results regarding the system.

6.2 System description.

The original 40-variable system of [34] is given by

$$\dot{x}_i = x_{i-1}x_{i+1} - x_{i-1}x_{i-2} - x_i + F, \qquad i = 1, \ldots, n, \tag{6.2}$$

where we define $x_{-1} = x_{j-1}, x_0 = x_j$, and $x_{j+1} = x_1$. One of the motivations for this choice is that we note that

$$\sum_i x_i(x_{i-1}x_{i+1} - x_{i-1}x_{i-2}) = 0.$$

Therefore, using the natural energy function

$$E = \frac{1}{2}\sum_i x_i^2,$$

we compute

$$\dot{E} = \sum_i x_i(-x_i + F),$$

where the derivative is taken along trajectories of the system. In the original system, this was used to conclude that for fixed F, trajectories would be bounded and the origin would be unstable.

Motivated by this system, we define the cubic system by

$$\dot{x}_i = x_{i-1}x_{i+1} - x_{i-1}x_{i-2} - \underbrace{x_i(x_i - a)(x_i - b)}_{f(x_i)} =: g_i(\boldsymbol{x}), \qquad i = 1, \ldots, n, \tag{6.3}$$

with $0 < a < b$, and $g(x)$ is defined simply for ease of notation. Our goal in choosing this description was to take advantage of the basic structure of the system while providing two control parameters. Consequently, we are able to increase the number of positive Lyapunov exponents of the saddle while preventing the system from developing a chaotic attractor.

Applying the natural energy function, we find that

$$\dot{E} = \sum_i -x_i f(x_i) = \sum_i -x_i^2(x_i - a)(x_i - b). \tag{6.4}$$

We can immediately conclude that the origin is now stable. Additionally, if $x_i > b$ for all i, then the energy is decreasing, so trajectories remain bounded. Energy is added to the system

by each component satisfying $a < x_i < b$. Although we cannot prove that no chaotic attractor exists, experimentally, we find that the system asymptotically approaches either a fixed point or a periodic orbit.

6.3 Fixed points

Let $\boldsymbol{x}_f$ be a fixed point of the system, and therefore satisfying

$$g_i(\boldsymbol{x}_f) = 0, \quad \forall i. \tag{6.5}$$

Although we see no general technique that identifies all solutions to (6.5), we are able to locate a large subset of the solutions by noting the following: If we restrict to the finite domain $x_j \in S = \{0, a, b\}$ for all j, then the cubic term in g_i is 0, and we can solve the simpler system,

$$\tilde{g}_i(\boldsymbol{x}) = x_{i-1}(x_{i+1} - x_{i-2}) = 0, \qquad i = 1, \ldots, n, \tag{6.6}$$

by considering solutions represented by length n sequences on the three symbols $\{0, a, b\}$. Although there are 3^n such sequences, not all such sequences are solutions to (6.6). Our goal is to both enumerate and understand this solution subset, which we call *special fixed points* and denote by the symbol $\mathcal{S}$.

6.3.1 Allowable sequences and solutions.

Since we desire to generate sequences that are solutions to (6.6), we define a process on the symbols of set S that will satisfy $\tilde{g}_i(\boldsymbol{x}) = 0$ for arbitrary i :

$$\begin{aligned} &\text{if} \quad x_{i-1} \neq 0 \quad \text{then} \quad x_{i+1} = x_{i-2} \\ &\text{if} \quad x_{i-1} = 0 \quad \text{then} \quad x_{i+1} \in S \end{aligned} \tag{6.7}$$

We can express this process via a digraph $\mathcal{G}$ as follows: Since the possible future states of the system are determined by the triple (x_{i-2}, x_{i-1}, x_i), we let vertices of the graph be represented by a three symbol sequence. There is an edge from vertex tuv to vertex uvw if setting $x_{i-2} = t, x_{i-1} = u, x_{i+1} = w$ satisfies (6.7). The complete digraph, $\mathcal{G}$, is shown in Fig 6.1.

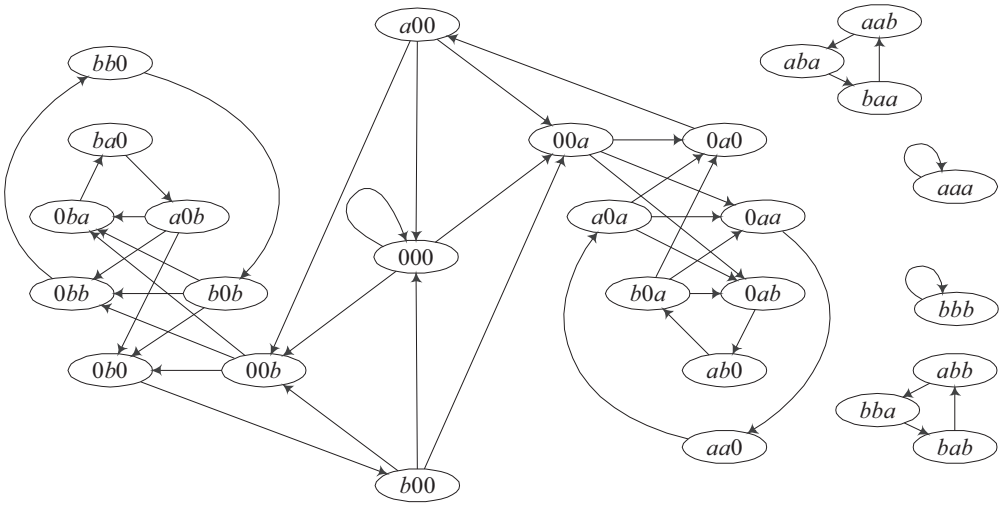

Figure 6.1: Digraph $\mathcal{G}$.

As we move from one vertex to the next along an edge of $\mathcal{G}$, we are, in essence, adding only the symbol w to our generated sequence. Therefore, a walk of length n in the graph can be placed in 1-1 correspondence with a symbol sequence of length n. Since a solution to (6.6) must satisfy (6.7) for all i, and our indices are taken mod n, the resultant condition in terms of the graph is that the walk of length n must be *closed* — it must begin and end at the same vertex. To count the number of special solutions, we apply some additional results from graph theory. Let $A = [a_{ij}]$ be the adjacency matrix of $\mathcal{G}$, defined by labeling the 27 vertices of $\mathcal{G}$ as $e_1, \ldots, e_{27}$ and let $a_{ij} = 1$ if there is an edge from e_i to e_j, and 0 otherwise. Let $C = A^n$. Then a well known result from graph theory tells us that c_{ij} is the number of length n walks from e_i to e_j [35]. Since solutions must be closed walks on $\mathcal{G}$, we can compute the cardinality of $\mathcal{S}$ by summing the main diagonal of C :

$$\|\mathcal{S}\| = N(n) = \sum_{i=1}^{27} c_{ii} = \operatorname{tr} A^n. \tag{6.8}$$

Fig 6.2 shows a plot of $\log N$ as a function of n and indicates that the number of solutions grows exponentially with n, with $N(n) \approx (1.8516)^n$, (whereas a full shift on three symbols would grow as 3^n).

Although the symbol dynamics defined by graph $\mathcal{G}$ could be studied as a discrete dynamical system, our primary focus remains understanding the character of the special fixed points. As

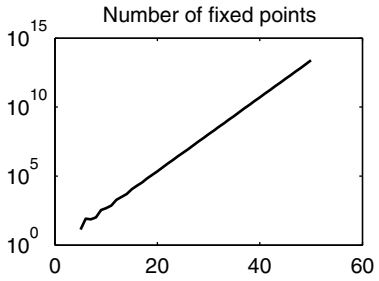

Figure 6.2: A plot of $\log N(n)$ indicates that the number of fixed points grows exponentially with the dimension of the system.

such, we address only a few of the consequences of those dynamics which apply whenever $n \geq 4$.:

1. Three adjacent non-zero entries force the entire sequence to be a repetition of those three symbols. Example: $(a, a, a, \ldots), (b, b, b, \ldots), (a, a, b, a, a, b, \ldots), (a, b, b, a, b, b, \ldots)$.

2. As a corrolary to item (1), if a sequence contains a 0, then at most two non-zero components may be sequential. Therefore, at least 1/3 of the components must be 0. Example: $(\ldots, 0, u, v, 0, u, u, 0, u, \ldots)$.

3. When at least two zeroes separate portions of the sequence, the sequence is separated into two independent parts. Example: (*'word 1'* , $0, 0,$ *'word 2'*, $0, 0$), where word 1 and word 2 are any allowable subsequences that contain a 0.

6.3.2 Stability analysis of special fixed points.

Linear stability analysis is based upon finding the eigenvalues of the Jacobian matrix, J, at each of the fixed points. The required partial derivatives to compute J are

$$\frac{\partial g_i}{\partial x_{i-2}} = -x_{i-1}, \tag{6.9}$$

$$\frac{\partial g_i}{\partial x_{i-1}} = x_{i+1} - x_{i-2}, \tag{6.10}$$

$$\frac{\partial g_i}{\partial x_i} = \begin{cases} -ab & \text{if } x_i = 0\ , \\ a(b-a) =: ad > 0 & \text{if } x_i = a\ , \\ -b(b-a) =: -bd < 0 & \text{if } x_i = b\ , \end{cases} \tag{6.11}$$

$$\frac{\partial g_i}{\partial x_{i+1}} = x_{i-1}, \tag{6.12}$$

where $d := b - a$, defined for ease of notation, will become a key parameter in determining the stability of the fixed points. All other partial derivatives are 0, resulting in a Jacobian matrix with entries concentrated near the main diagonal. For the general element of $\mathcal{S}$, the constraint of (6.7) forces further sparseness along the sub-diagonals. However, the circular indexing convention allows the possibility that the upper right and lower left corners of the Jacobian may be non-zero.

The fixed points at $\mathbf{b} = (b, b, b, \ldots)$ and $\mathbf{a} = (a, a, a, \ldots)$. The Jacobian for these points are *circulant matrices,* where each row is a circular shift to the right of a previous row:

$$J_b = b \begin{bmatrix} -d & 1 & 0 & \ldots & 0 & -1 & 0 \\ 0 & \ddots & \ddots & \ddots & & \ddots & -1 \\ -1 & \ddots & & & & & 0 \\ 0 & \ddots & & & & & \vdots \\ \vdots & & & & & & \\ & & & & & \ddots & 0 \\ 0 & & & \ddots & \ddots & \ddots & 1 \\ 1 & 0 & & & -1 & 0 & -d \end{bmatrix}, \qquad J_a = a \begin{bmatrix} d & 1 & 0 & \ldots & 0 & -1 & 0 \\ 0 & \ddots & \ddots & \ddots & & \ddots & -1 \\ -1 & \ddots & & & & & 0 \\ 0 & \ddots & & & & & \vdots \\ \vdots & & & & & & \\ & & & & & \ddots & 0 \\ 0 & & & \ddots & \ddots & \ddots & 1 \\ 1 & 0 & & & -1 & 0 & d \end{bmatrix}.$$

The circulant structure allows easy closed form computation of the eigenvalues. Using standard results from linear algebra, one finds that the eigenvalues of J_b are given by

$$p_b(z) = b\left(-d + z - z^{-2}\right)$$

evaluated at each of the nth roots of unity in the complex plane. To make a general conclusion (for arbitrary n), we proceed as follows: Consider the image of the unit circle $|z| = 1$ under the transformation

$$p_1(z) = z - z^{-2},$$

which is given graphically by Fig 6.3. $p_b(z)$ is a shift (by $-d$) and a scaling of that image, and

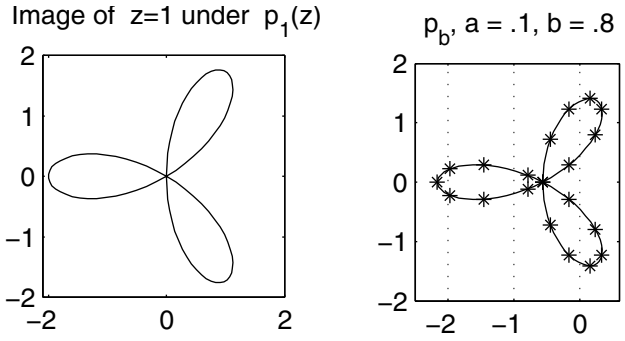

Figure 6.3: (L) The image of $|z| = 1$ under the map $p_1(z) = z - z^{-2}$. The maximum real part of the image is 9/8. (R) $p_b(|z| = 1)$ for $a = .1, b = .8$. The asterisk values indicate the eigenvalues for the case $n = 20$, showing the fixed point to be a saddle with a six dimensional unstable subspace.

all eigenvalues of J_b must fall on that curve. It is a simple exercise in complex arithmetic to show that the maximum real part of $\Lambda = \{p_1(z)||z| = 1\}$ is 9/8. Therefore, whenever $d = b - a > 9/8$, all of the eigenvalues will have negative real part, and $\boldsymbol{b}$ is stable, and otherwise, the point is a saddle. A similar analysis of J_a shows that its eigenvalues must fall on the scaled image of Λ after it has been shifted to the right by d (and then scaled by a). So $\boldsymbol{a}$ is a saddle for $d < 2$, and an unstable node or focus otherwise. The saddle behavior as a function of d is illustrated in Fig 6.4, which plots the number of unstable directions as a function of $d = b - a$.

Analysis of other special fixed points. To determine the stability of the other fixed points requires a detailed case by case analysis of each of possible subsequence and we are not able

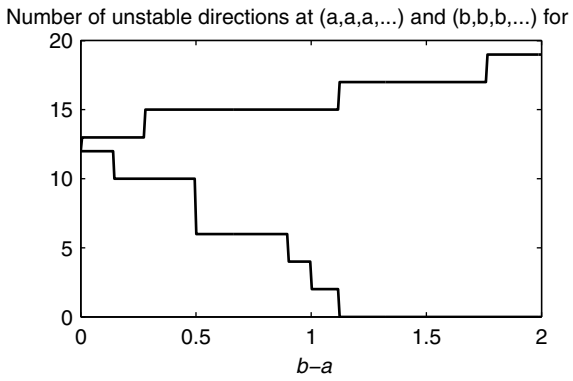

Figure 6.4: A plot of the number of unstable directions at **a** (upper curve) and **b** (lower curve) for $n = 20$.

to provide complete results. We note that if $(0, 0, 0, 0)$ appears in the fixed point, we can arrange the Jacobian to force a block lower triangular structure and determine the spectrum explicitly. Additionally, many other patterns allow the reduction to block lower triangular form. Analysis of those special cases, as well as numerical experimentation leads to the following observations and conjectures:

Observations:

- The origin is always stable, with all eigenvalues $-ab$, with Jacobian $diag\{-ab, \ldots, -ab\}$.
- The fixed point $\mathbf{b} = (b, b, b, \ldots)$ may be either attracting or a saddle, with its character depending only on the difference $b - a$.
- The fixed point $\mathbf{a} = (a, a, a, \ldots)$ is always unstable, but may be either a source or saddle, again dependent upon the difference $b - a$.
- Fixed points where all components are either 0 or b are stable as long as there is at least one component that is 0.

Conjectures:

- If any component is a, the fixed point will have some eigenvalues with positive real part and some with negative real part.

- Let n_a be the number of a components in the fixed point. Then the dimension of the unstable subspace is either n_a or $n_a - 1$ or $n_a + 1$.

To count stable fixed points, we simply need to identify all possible sequences that use only the components 0 and b. Using the same graph approach as for counting all fixed points, we develop graph $\mathcal{G}_b$, which is a subgraph of $\mathcal{G}$, and is illustrated in Fig 6.5.

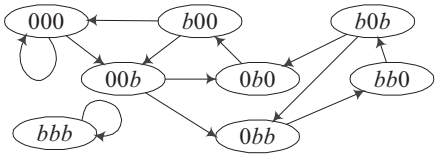

Figure 6.5: Digraph $\mathcal{G}_b$, generates allowable sequences using only the symbols 0 and b.

From $\mathcal{G}_b$, we identify the associated adjacency matrix B. We apply the same counting approach as in §6.3.1, but now defining $D = [d_{ij}] = B^n$, to find the number of stable fixed points

$$N_b(n) = \sum_{i=1}^{8} d_{ii} = \operatorname{tr} B^n, \tag{6.13}$$

which can be estimated by $N_b(n) \approx (1.559)^n$. We note that inclusion of the vertex (b, b, b) generates the fixed point $\boldsymbol{b}$ which may not be a stable fixed point, but is included for completeness. Fig 6.6 illustrates the exponential growth of (6.13).

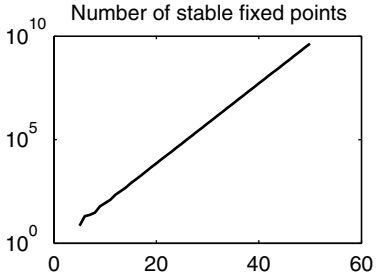

Figure 6.6: A plot of $\log N_b(n)$ indicates that the number of stable fixed points grows exponentially with the dimension of the system.

6.3.3 Brief comments on other attractors in the system.

The identification of other attractors in the system has been primarily through numerical simulation. We find that in the parameter range where we focused our attention ($b \leq 0.5$), most of phase space is attracted to one of the stable special fixed points. Occasionally, a random initial condition would approach some other stable fixed point, but this occurred in only a small percentage of the cases, and only when $n/4$ was an integer. The resultant fixed point was a circular repetition of four values, $(x_1, x_2, x_3, x_4, x_1, \ldots)$, where at least one of those components must be negative. This solution was the fixed point of the system when $n = 4$, repeated via the circular symmetry of the problem. For $b \approx 2$, the asymptotic solution was sometimes a periodic solution, which further complicates the overall attractor structure.

6.4 Defining a Lifetime Function

Background. The general language which facilities description of chaotic transients is the *lifetime function.* We assume that the chaotic saddle S is contained in some compact set B, where $B \cap A = \emptyset$ for any attractor A for the system. Therefore, a.e. trajectory that starts in B will eventually leave that set. If we define $x(t)$ to be the trajectory of the initial condition x_0 under the dynamics of the system, then we define the lifetime L of a point $x_0 \in B$ as the time that the trajectory first leaves B :

$$L(x_0) = \min_t \{t | x(t) \notin B\}.$$

Since the chaotic saddle is invariant, if $x_0 \in S$, then $L(x_0) = \infty$. As a corrolary, it is assumed that we can define a "long" lifetime L_t, such that if $L(x_0) > L_t$, then x_0 is "close" to S.

The above approach has been used successfully to implement various algorithms that seek to explore the set S [19, 25, 13, 18]. However, we note that some systems do not lend themselves to easy implementation of the typical lifetime function described above. In particular, we note three specific difficulties that may arise.

1. In general, all attractors must be known to define an appropriate set B. For many systems,

especially with $n > 2$, it may be very difficult to ensure that all fixed points and stable periodic orbits have been identified.

2. If the attractor is not a single point, but rather a collection of fixed points, stable periodic orbits, and unbounded trajectories, the set B becomes significantly more complicated, with potentially less confidence that the choice satisfies the conditions that $S \subset B$ and $B \cap A = \emptyset$. Moreover, the computational difficulty in determining the first time T such that $x(T) \notin B$ may be excessive.

3. If one cannot determine an a priori estimate of the basin of attraction of A, then to provide the greatest assurance that $S \subset B$ one would choose B to be as close as possible to the attractor A. Consequently, a trajectory may spend significant time far from the saddle before it exits B. The *lifetime*, then, may be dominated by slow dynamics away from the saddle, making it difficult to determine a reliable threshold, L_t.

A new lifetime function: Theory. As indicated by §6.3, the system we are considering in this paper certainly creates the difficulties generated by a complicated attractor. To attempt to overcome these obstacles, we develop a lifetime function that relies on the fact that the invariant set has at least one positive Lyapunov exponent. We assume that near the invariant set, the system will show sensitive dependence on initial conditions for almost every initial condition. at least for some finite time interval. Moreover, we assume that for most trajectories, exponential divergence of nearby trajectories will be detectable after a fixed, finite integration time.

The basic idea is that a trajectory near the chaotic saddle will behave like a chaotic trajectory, and nearby initial conditions would diverge over time, which implies that phase space is locally expanding in at least one direction. Since the saddle is unstable, the trajectory will eventually move away from the invariant set and toward the attractor, where phase space on average is contracting in all directions. We will define a lifetime function that is based on identifying this change in expansion properties. In the neighborhood of attracting fixed points , nearby trajectories converge over time, which is relatively easy to detect. However, attracting periodic orbits in an autonomous system present an additional difficulty in that ω-limit set for nearby trajectories is

the periodic orbit itself. Points on the periodic orbit do not converge in the direction along that periodic orbit. Therefore we will define *lifetime* by requiring only that nearby trajectories are converging in the directions transverse to the flow.

Formal definition of the lifetime function for bounded trajectories. Consider the dynamical system in $\mathbb{R}^n$ given by

$$\dot{\boldsymbol{x}} = F(\boldsymbol{x}) \tag{6.14}$$

We define the lifetime of the point $\boldsymbol{x}_0$, denoted $L(\boldsymbol{x}_0)$, as follows: Let $\boldsymbol{x}(t)$ be the trajectory satisfying (6.14) with $\boldsymbol{x}(0) = \boldsymbol{x}_0$. Linearizing about that trajectory leads to a variational equation of the form

$$\dot{\boldsymbol{\xi}} = J(t)\boldsymbol{\xi}, \tag{6.15}$$

where $J(t)$ is the Jacobian of $F(\boldsymbol{x})$ evaluated at $\boldsymbol{x}(t)$. The linear system (6.15) yields a fundamental solution matrix, $\Phi(t)$ such that $\boldsymbol{\xi}(t) = \Phi(t)\boldsymbol{\xi}_0, \quad \boldsymbol{\xi}_0 = \boldsymbol{\xi}(0)$. Since we are interested in the behavior of trajectories perturbed perpendicular to the flow, we define set

$$\mathcal{A}(\boldsymbol{x}_0) = \{\boldsymbol{\xi}_0 \text{ s.t. } \|\boldsymbol{\xi}_0\| = 1 \text{ and } \boldsymbol{\xi}_0^T F(x_0) = 0\},$$

the intersection of the unit ball with the perpendicular hyperplane. We define a scalar amplitude function

$$A(t) = \max_{\boldsymbol{\xi}_0 \in \mathcal{A}(\boldsymbol{x}_0)} \|\Phi(t)\boldsymbol{\xi}_0\|. \tag{6.16}$$

If phase space is expanding, then $A(t)$ will increase (on average). When the trajectories enter a contracting area of phase space, $A(t)$ will decrease. As the trajectory approaches an attractor, $A(t) \to 0$. Our lifetime function marks the transition from expanding to contracting phase space, which we take to be when $A(t)$ reaches its maximum value. Since it is possible for $A(t)$ to achieve its maximum at two different times, we ensure that $L(\boldsymbol{x}_0)$ is well defined by choosing the first time at which $A(t)$ achieves a global maximum:

$$L(\boldsymbol{x}_0) := \min_t\{t : A(t) = \max_t A(t)\}. \tag{6.17}$$

6.5 Implementation of the lifetime calculation.

Numerical implement of the lifetime function defined above presents three computationally difficulties:

1. For an n dimensional system, calculation of the tangent bundle (to calculate $\Phi(t)$) requires solving an $n(n+1)$ dimensional ODE. For large n, that calculation may become impractical.

2. To determine $A(t)$ for each fixed t, we must perform a maximization which is computationally comparable to an induced matrix norm operation, which will be very time consuming.

3. The definition also requires us to find a global maximum of $A(t)$. In general, a numerical calculation of a global extrema has some risk that the extrema is not within the (finite) search domain.

Our algorithm is specifically designed to reduced the computational issues of items (1) and (2) using a reasonable approximation technique. We are unable to avoid the third computational issue. However, our search technique guarantees that the actual lifetime is at least as large as the computed lifetime. We discuss the implication of this error near the end of this section.

To reduce the size of the system to be integrated, Our simplified numerical approach is based on the fact that under the evolution of a flow, almost every perturbed initial condition tends to align to the most unstable direction of the system. Therefore, instead of computing $A(t)$, we estimate its behavior by monitoring the difference between the nominal trajectory and a nearby trajectory. We call this difference $\delta(t)$, and define $A_\delta := |\delta|$ as our approximation to the amplitude function $A(t)$.

To ease the notation required to describe the computational algorithm, we define the following operators:

1. *Flow operator* ϕ_t, which is the flow of the original system , such that $x(t) = \phi_t x_0$ is a solution to (6.14) for all x_0.

2. *Projection operator* P_x, defined as

$$P_x(v) := v - F(x)\frac{v^T F(x)}{|F(x)|},$$

which projects v onto the hyperplane perpendicular to the trajectory of (6.14) at $x = x(t)$.

3. *Normalizing operator* $\mathcal{N}$, where

$$\mathcal{N}(x) := \frac{x}{|x|}.$$

Algorithm Description. Our goal is to compare the nominal trajectory of x_0 with a perturbed trajectory. We desire to approximate the dynamics of the linearization, so we select a small positive scalar ϵ, and let

$$\delta_0 = \epsilon\mathcal{N}\left(P_{x_0}((1,\ldots,1)^T)\right),$$

which yields an ϵ sized perturbation in a direction perpendicular to the flow. The evolution of the perturbation is given by

$$\delta(t) = \phi_t(x_0 + \delta_0) - \phi_t(x_0).$$

If A_δ grows too large, our computation is not providing a good approximation of the linearized equation, so we rescale back to the linear regime as follows: Let $M > \epsilon$ be a small positive number such that if $A_\delta < M$, then the linear approximation is reasonable. If $A_\delta(\hat{t}) = M$ then we rescale by letting

$$\hat{x} = \phi_{\hat{t}}(x_0), \tag{6.18}$$

$$\hat{\delta} = \epsilon\mathcal{N}\left(P_{\hat{x}}\left(\delta(\hat{t})\right)\right), \tag{6.19}$$

and redefining $\delta(t)$ on the interval $t \geq \hat{t}$ as

$$\delta(t) = \phi_t(\hat{x} + \hat{\delta}) - \phi_t(\hat{x}). \tag{6.20}$$

In addition to rescaling, (6.19) projects the perturbation back to the tranverse hyperplane, which eliminates any tangential component which may have been generated by the non-linear evolution of the flow. Fig 6.7 illustrates this rescaling and projection.

The above discussion describes how we will compute $A_\delta(t)$. In principle, we seek the global maxima of that function which would require an infinite search. Instead, we will search only some finite period beyond the time of a possible global maximum. Specifically, we let $T^* > 0$ be a sufficiently large increment of time such that if $A_\delta(t) \geq A_\delta(t+s) \quad \forall s \in [0, T^*]$ then we will assume $A_\delta(t) \geq A_\delta(t+s) \quad \forall s \geq 0$. We note that as $T^* \to \infty$, this search technique yields the global maximum. Choosing T^* large increases our probability of correctly identifying the global maximum, but it also increases the time to perform the optimization. The algorithm to calculate $L(x_0)$ is given in Table 6.1.

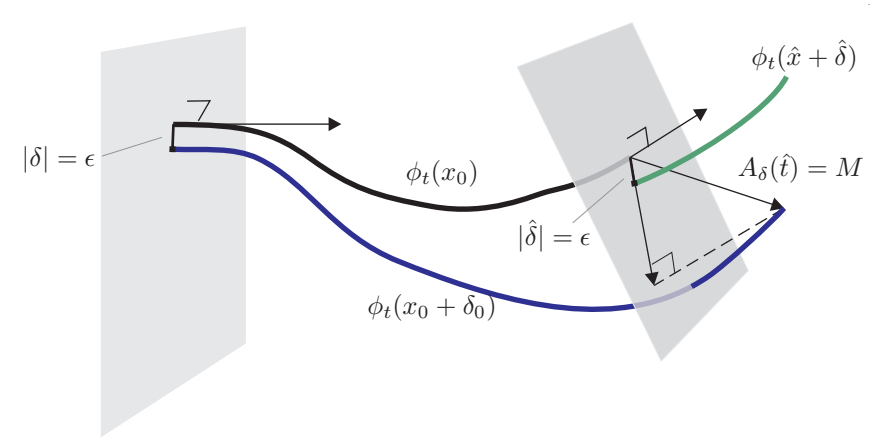

Figure 6.7: When the difference between the nominal trajectory, $\phi_t(x_0)$ and the perturbed trajectory $\phi_t(x_0+\delta_0)$ gets too large, the perturbation is projected to the plane perpendicular to the flow and rescaled to size ϵ.

		Remarks
1	Input x_0	
2	Set ϵ, M, T^*	Algorithm parameters as described above.
3	$L = 0, A = \epsilon,$ $\delta_0 = \epsilon\mathcal{N}\left(P_{x_0}((1,\ldots,1)^T)\right)$ $t_r = 0$	$L = L(x_0)$ will be computed. A holds the maximum amplitude value. δ_0 is as discussed above. t_r tracks the time of the last rescaling and projection operation and is used in determining a stopping criteria.
4	While $A_\delta \leq M$ and $t \leq L + T^*$: Compute $\delta(t)$ forward in time. Let $A = \max_{t_r \leq s \leq t} A_\delta(s)$ Let $L = \min_{t_r \leq s \leq t}\{s : A_\delta(s) = A\}$ end while	Calculation of δ is via some numerical integrator. The stopping criterion for the "while loop" are: (1) the perturbation grows too large (which requires rescaling), or (2) we have evaluated T^* units beyond the time of the last maxima. A and L are updated to track the time of the last maxima.
5	If $A = M$ then: $A = \epsilon$, $t_r = t$, rescale $\delta(t)$ to size ϵ. goto step 4 end if.	Rescaling of δ is as indicated by (6.19). Since this step was reached by pausing the integration at the point where A_δ was increasing through M, the global max could not have yet been reached. Therefore, reseting A and $\lvert\delta(t)\rvert$ to size ϵ does not invalidate the forward time search for the maximum.
6	Output L	To reach step 6, the current time t is T^* units beyond the time of the maximum (L), which satisfies our stopping criteria for the search for the global maxima.

Table 6.1: Algorithm for computing lifetime.

Implications of finite search for global maximum — choosing T^*. The theoretical algorithm requires determining the time of global maximum for the amplitude function. However, our search is on a finite domain. The immediate implication is that the *actual* lifetime of a point must at least as great as the *computed* lifetime. Therefore, the algorithm may "miss" some points that are near the saddle, and assign them a "short" lifetime. Since our search extends beyond L by T^* time units, our approximating algorithm yields

$$L_{\text{actual}} \approx L_{\text{computed}} \quad \text{or} \quad L_{\text{actual}} \geq L_{\text{computed}} + T^*.$$

By appropriate choice of T^*, we significantly improve the likelihood of correctly approximating the lifetime. Our technique for choosing T^* is as follows: Let $L_\tau(x_0)$ be the calculated lifetime of x_0 under the parameter choice $T^* = \tau$. As $\tau \to \infty$, $L_\tau(x_0)$ will monotonically approach the time of the global maximum for A_δ. From graphical inspection of a few plots of $A_\delta(t)$ for typical trajectories, we choose a time τ such that τ is longer than the time between local maxima of A_δ. Our basic approach is to compute $L_{k\tau}$ for increasing values of k until we no longer see an increase in computed lifetime. When we find k large enough so that $L_{k\tau} = L_{2k\tau}$ for a test ensemble of initial conditions, we set $T^* = k\tau$.

6.6 Some numerical results on the chaotic saddle.

The fundamental goals of our numerical experimentation were:

1. Assess the general behavior of the chaotic transient.
2. Determine the effectiveness of the our lifetime algorithm in providing accurate classification of points near the chaotic saddle.
3. To employ the lifetime function as part of a Step-and-Stagger approach to identifying the chaotic saddle. Using this approach, determine the number of positive Lyapunov exponents of the saddle.

General behavior. For a large subset of initial conditions, the trajectory has a chaotic transient period before decaying to one of the special fixed points (when n is a multiple of 4, a

nontrivial fixed point was often located). As a typical example: Using $a = 0.2, b = 1.2, n = 20$, (so that (b) was unstable) we initiate 5193 random initial conditions with $b < x_i < b + 1$. Of those 5193, there were 1113 that were attracted to a circular permutation of a fixed point of the $\mathbb{R}^4$ system, $(0.9891, 0.1928, -0.3198, -0.3212, \ldots)$. The rest of the trajectories all approached one of the special fixed points, with 1495 different special fixed points identified. Fig 6.8 shows a graphical representation of the special fixed points reached. Fig 6.9 displays the distribution of lifetimes of those initial conditions, plotting $f(L)$, the fraction of points whose lifetime is at least L. The exponential distribution of lifetimes is typical of chaotic saddles. The mean lifetime is ≈ 144.

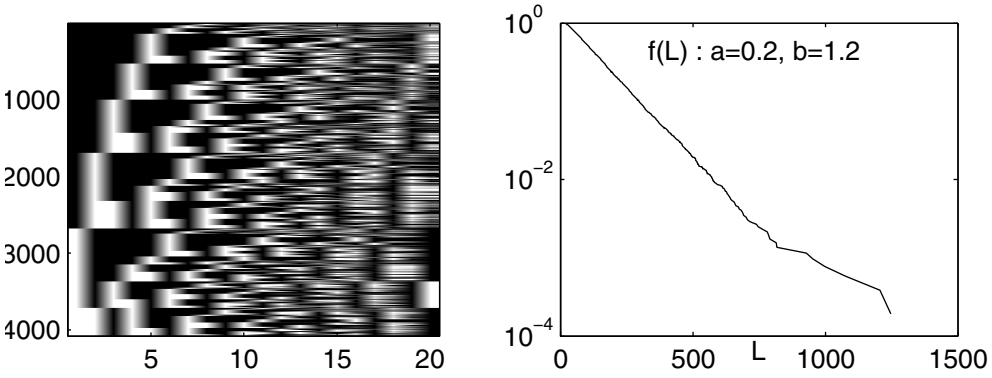

Figure 6.8: For the 4080 trajectories that ended at a special fixed point, the fixed point with components 0 and b are represented by white and black spaces respectively. The rows are shown in sorted order to illustrate the distribution of various fixed points.

Figure 6.9: A plot of $f(L)$, the fraction of sampled points whose lifetime exceeds L. The linear graph on the semilog plot indicates an exponential distribution of lifetimes.

Effectiveness of the lifetime computation. We repeated the above experiment with the same parameter value and method of selecting initial conditions, but using $n = 30$. The calculated mean lifetime increase to ≈ 290. Of the 1908 points included in the data run, all but 93 had converged to one of the special fixed points at the termination of the lifetime calculation (when using a search interval value of $T^* = 1000$. Further analysis of those 93 points indicated that the trajectories had entered a portion of phase space that appeared to be near the stable manifold of

an unstable periodic orbit. When recomputed using $T^* = 2000$, all had a longer lifetime, and at the termination of that lifetime calculation, all were converging to one of the special fixed points. The fact that we found no non-special attracting fixed points reflects our observation that we found such attractors only when n was divisible by 4.

As an example of the algorithms ability to detect periodic attractors, we provide the following example for $a = 0.1, b = 1.9, n = 30$. With randomly chosen initial conditions satisfying $a < x_i < a + 1$, we find that about 10 percent of the trajectories are attracted to periodic motion. Figure 6.10 shows a portion of the trajectory for such an initial condition $\boldsymbol{z}$. $L(\boldsymbol{z})$ was computed to be 322.8, (the vertical bar on the plot) which appears to match where the trajectory passes from chaotic to periodic motion.

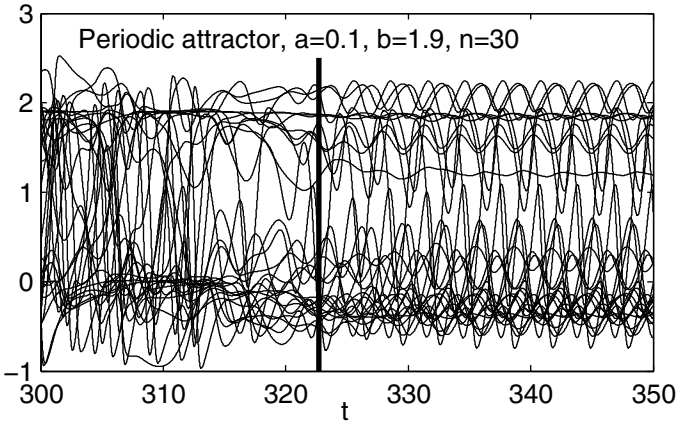

Figure 6.10: With $a = .1, b = 1.9, n = 30$, about 10 percent of the trajectories approach a periodic attractor. The computed lifetime for this trajectory was 322.8, which appears to mark the transition from chaotic to periodic motion.

Hyperchaotic saddle behavior. When $b - a < 1.125$, the fixed point $\boldsymbol{b}$, is unstable. Therefore, if the system is to settle into one of the special fixed points, at least 1/3 of the components must fall into its potential well near $x_i = 0$. Since a provides an upper bound for the size of that potential well, when a is small, the system spends significant time in the transient chaos region. We find that the increase in lifetime (with decreasing a) is matched by a gradual

growth in the number of positive Lyapunov exponents. Additionally, when $b - a$ is reduced, the potential well at b is reduced, which may further increases the hyperchaos of the saddle. We used the Step-and-stagger technique to find long numerical trajectories that were sufficient to approximate the Lyapunov spectrum. The smallest value for a that we examined was $a = .01$. We believe that additional increases in the number of positive Lyapunov exponents may be achieved by further decreases in a, but we did not examine those cases due to the additional computational time required to maintain accuracy of the algorithms. Despite the high dimensional problem and the hyperchaotic structure of the saddle, Step-and-Stagger efficiently computed long trajectories. We note, however, that the algorithm could not have been implemented on this problem without the new lifetime function defined above. Some select results are provided in Table 6.2.

Dimension	parameters	Leading Lyapunov exponents
$n = 20$	$a = .01, b = .3$	$.07 \quad .05 \quad .04 \quad .025 \quad .02 \quad .008 \quad .0015 \quad -.0013$
$n = 20$	$a = .01, b = .5$	$.12 \quad .11 \quad .07 \quad .05 \quad .03 \quad .013 \quad -.001 \quad -.01$
$n = 20$	$a = .01, b = .8$	$.20 \quad .16 \quad .11 \quad .07 \quad .01 \quad -.002 -.03$
$n = 10$	$a = .01, b = .8$	$.16 \quad .07 \quad .003 \quad -.03$
$n = 30$	$a = .01, b = .8$	$.21 \quad .19 \quad .14 \quad .12 \quad .08 \quad .06 \quad .03 \quad .001 \quad .0001 \quad -.02$
$n = 40$	$a = .01, b = .8$	$.20 \quad .19 \quad .17 \quad .14 \quad .11 \quad .10 \quad .08 \quad .06 \quad .03 \quad .026 \quad -.0045$

Table 6.2: Leading exponents calculated for the chaotic saddle.

Chapter 7

Future Work

The results of this thesis lay the groundwork for some fruitful areas of further research. The following paragraphs outline some of the research questions that would provide useful follow-on to the academic work of this thesis.

The edge in other flow models. We conjecture that the *edge* is not simply an artifact of the particular model studied in this problem, and should therefore be present in other models of these parallel shear flows, including full numerical simulations of both plane Couette flow and Pipe flow. The edge should play a significant role in controlling these transient turbulence systems. However, additional studies (on other models and in experiments) will be required to better understand this structure.

The edge in other systems. We conjecture that the edge should be a typical behavior observed in systems where transient chaos is developed by an underlying horseshoe structure. It is likely that the edge will have physical relevance in these systems. The techniques developed in this thesis need to be applied to other transient systems to test these ideas.

Smoothness of the edge. We conjectured that the edge should be smooth if the expansion rate away from the edge was greater than the expansion rate tangent to the edge. We expect that a rigorous proof can be developed for hyperbolic systems.

Can we target decay of turbulence? In Chapter 4, we illustrated some techniques to identify the *hole in the saddle,* typical paths followed by transient trajectories as they depart the vicinity of the saddle. Whereas the edge (Chapters 3 and 5) help to define regions of phase space that initiate long transients, the hole describes regions of phase space that tend to allow those transients to die. In a practical application, it might be possilbe to "target" these regions, hoping to make the system return to the laminar flow condition more quickly. Because the turbulent system is undergoing a chaotic transient, one should be able to implement this targeting control

with small perturbations. In the model setting, it is clear that given some state of the system, one can search for nearby points with short lifetime. However, the underlying concept is that one would want to be able to implement a real-time control strategy, which means that there is not time to test the lifetimes of the nearby points. As an alternative approach, we might look for a "nearby" perturbed system whose chaotic saddle has a natural measure that is more heavily weighted to the hole of the unperturbed system.

Lyapunov exponents of the edge and the saddle. In this system studied, when the edge was the manifold of a periodic orbit, it had only one positive Lyapunov exponent, while the saddle itself had two positivie exponents. Yet the edge is dense in the saddle. Understanding the relationship between these behaviors should lead to better understanding of transient chaos.

Improving Step-and-Stagger. The multistagger technique was a first attempt at improving the standard *Step-and-Stagger* algorithm. For the systems studies in this thesis, the algorithm was sufficiently robust to track the chaotic saddle. However, in systems where the dimension of the stable set of the saddle is small, the random search techniques may prove intractable. However, based on the improved understanding of how the *edge* creates structure to the basin of the attractor, it may be possible to develop better techniques to more appropriately choose a step size and search direction that will more efficiently yield psuedo-trajectories.

Step-and-Stagger in high dimensional systems We conjecture that the efficiency of *Step-and-Stagger* does not depend on the dimensionality of the system, but only upon the *defect* — the difference between the dimension of the system and the dimension of the stable set. It should be possible to establish rigourous results to that affect by following the implications of Appendix E.

Appendix A

Equations of motion for 9-variable model of plane Couette flow.

The general structure of the n dimensional Galerkin models of plane Couette flow is that of ordinary differential equations with linear damping, quadratic coupling and a constant forcing:

$$\dot{x}_i = -\frac{d_i}{Re}x_i + \sum_{j,k} a_{i;j,k}x_j x_k + f_i, \quad i = 1., \ldots, n. \tag{A.1}$$

Besides the Reynolds number, which controls the damping, there are two geometric parameters determining the widths and length of the flow domain. The laminar profile is a fixed point of the system. By linear change of coordinates, we translate the system to place the attracting laminar state at the origin. We denote this new system

$$\dot{\boldsymbol{y}} = Q(\boldsymbol{y}; Re), \tag{A.2}$$

indicating that the right hand side is quadratic in $\boldsymbol{y}$ and studied over the parameter Re. For a more detailed description of the derivation of the 9-variable model, the reader should refer to [10].

To simplify the expressions for the component equations (shown on the next page), we define $L = \sqrt{a^2 + b^2}$ with viscosity $\nu = \pi/Re$, where parameters a and b prescribing the streamwise and spanwise periodicity. The equations of motion as given retain the geometric parameters. However, the specific geometric parameters studied in this thesis used $a = 2/\pi$ and $b = 1/\pi$. One may verify from the equations of motion that the flow of (A.2) has a symmetry, given by the transformation

$$(y_1, y_2, y_3, y_4, y_5, y_6, y_7, y_8, y_9) \to (y_1, y_2, -y_3, y_4, -y_5, -y_6, y_7, -y_8, -y_9).$$

$$
\begin{aligned}
\dot{y}_1 = -\nu y_1 \quad & + \frac{4a}{\sqrt{L^2+1}} y_3 y_5 - \frac{2a}{\sqrt{1+a^2}} y_4 y_7 - \frac{12b}{\sqrt{L^2+1}\sqrt{L^2+4}} y_5 y_8 \\
& - \frac{4a}{\sqrt{L^2+1}} y_5 y_9 - \frac{4a}{\sqrt{L^2+4}} y_6 y_8 \\
\dot{y}_2 = -9\nu y_2 \quad & - \frac{6a}{\sqrt{1+a^2}} y_4 y_7 - \frac{12b}{\sqrt{L^2+1}\sqrt{L^2+4}} y_5 y_8 + \frac{12a}{\sqrt{L^2+1}} y_5 y_9 - \frac{12a}{\sqrt{L^2+4}} y_6 y_8 \\
\dot{y}_3 = -\nu L^2 y_3 \quad & - \frac{16a}{\pi^2\sqrt{L^2+1}} y_5 - \frac{16b}{\pi^2} y_6 - \frac{2a}{\sqrt{L^2+1}} y_1 y_5 - 2b y_1 y_6 + \frac{6b^2 a - 2a^3}{L^2\sqrt{L^2+1}} y_4 y_5 \\
& + \frac{6ba^2 - 2b^3}{L^2} y_4 y_6 + \frac{4b^3 - 12a^2 b}{L^2\sqrt{1+a^2}\sqrt{L^2+4}} y_7 y_8 + \frac{6b^2 a - 2a^3}{L^2\sqrt{1+a^2}} y_7 y_9 \\
\dot{y}_4 = -\nu(4a^2+1) y_4 \quad & + \frac{8a}{\pi^2\sqrt{1+a^2}} y_7 + \frac{a}{\sqrt{1+a^2}} y_1 y_7 + \frac{3a}{\sqrt{1+a^2}} y_2 y_7 + \frac{2a}{\sqrt{L^2+1}} y_3 y_5 \\
& + \frac{6b}{\sqrt{L^2+1}\sqrt{L^2+4}} y_5 y_8 + \frac{6a}{\sqrt{L^2+1}} y_5 y_9 - \frac{6a}{\sqrt{L^2+4}} y_6 y_8 \\
\dot{y}_5 = -\nu(L^2+1) y_5 \quad & + \frac{24b + 8bL^2}{\pi^2\sqrt{L^2+1}\sqrt{L^2+4}} y_8 + \frac{3b + bL^2}{\sqrt{L^2+1}\sqrt{L^2+4}} y_1 y_8 + \frac{5b - bL^2}{\sqrt{L^2+1}\sqrt{L^2+4}} y_2 y_8 \\
& - \frac{4ab^2}{L^2\sqrt{L^2+1}} y_3 y_4 + \frac{5a^2 b - 3b^3 - bL^4}{L^2\sqrt{L^2+1}\sqrt{L^2+4}} y_4 y_8 - \frac{4ab^2}{L^2\sqrt{L^2+1}} y_4 y_9 \\
& - \frac{2ab^2}{L^2\sqrt{1+a^2}} y_5 y_7 - \frac{2ab^2\sqrt{L^2+1}}{L^2\sqrt{1+a^2}} y_6 y_7 \\
\dot{y}_6 = -\nu(L^2+1) y_6 \quad & + \frac{8b}{\pi^2} y_3 + \frac{8a}{\pi^2\sqrt{L^2+4}} y_8 + \frac{8b}{\pi^2} y_9 + b y_1 y_3 + \frac{a}{\sqrt{L^2+4}} y_1 y_8 + b y_1 y_9 \\
& + \frac{3a}{\sqrt{L^2+4}} y_2 y_8 + b y_2 y_9 + \frac{b^3 - 3a^2 b}{L^2} y_3 y_4 + \frac{3a^3 - 5ab^2}{L^2\sqrt{L^2+4}} y_4 y_8 + \frac{b^3 - 3a^2 b}{L^2} y_4 y_9 \\
& + \frac{2b^3}{L^2\sqrt{L^2+1}\sqrt{1+a^2}} y_5 y_7 + \frac{2ab^2}{L^2\sqrt{1+a^2}} y_6 y_7 \\
\dot{y}_7 = -4\nu(1+a^2) y_7 \quad & + \frac{4a^2 bL^2 - 4bL^2 + 16a^2 b}{L^2\sqrt{1+a^2}\sqrt{L^2+4}} y_3 y_8 - \frac{8ab^2}{L^2\sqrt{1+a^2}} y_3 y_9 + \frac{4ab^2}{L^2\sqrt{1+a^2}} y_5^2 \\
& + \frac{4a^2 bL^2 - 4bL^2 + 8a^2 b}{L^2\sqrt{1+a^2}\sqrt{L^2+1}} y_5 y_6 - \frac{4ab^2}{L^2\sqrt{1+a^2}} y_6^2 \\
\dot{y}_8 = -\nu(L^2+4) y_8 \quad & - \frac{8bL^2}{\pi^2\sqrt{L^2+1}\sqrt{L^2+4}} y_5 - \frac{bL^2}{\sqrt{L^2+1}\sqrt{L^2+4}} y_1 y_5 + \frac{bL^2 - 8b}{\sqrt{L^2+1}\sqrt{L^2+4}} y_2 y_5 \\
& - \frac{2a^2 b}{\sqrt{1+a^2}\sqrt{L^2+4}} y_3 y_7 + \frac{bL^4 - 8a^2 b}{L^2\sqrt{L^2+1}\sqrt{L^2+4}} y_4 y_5 + \frac{8ab^2}{L^2\sqrt{L^2+4}} y_4 y_6 \\
\dot{y}_9 = -\nu(L^2+4) y_9 \quad & + \frac{8a}{\pi^2\sqrt{L^2+1}} y_5 - \frac{8b}{\pi^2} y_6 + \frac{a}{\sqrt{L^2+1}} y_1 y_5 - b y_1 y_6 - \frac{3a}{\sqrt{L^2+1}} y_2 y_5 \\
& - b y_2 y_6 + \frac{-3a^3 + ab^2}{L^2\sqrt{L^2+1}} y_4 y_5 + \frac{3a^2 b - b^3}{L^2} y_4 y_6 + \frac{a}{\sqrt{1+a^2}} y_3 y_7 .
\end{aligned}
$$

Appendix B

Multi-stagger approach to pseudo-trajectories

As a brief description, the Step-and-stagger [13] algorithm operates as follows: a trajectory $\boldsymbol{x}(t)$ is numerically integrated as long as $L(\boldsymbol{x}(t))$ remains above some threshold value T^*. This threshold is chosen such that $\boldsymbol{x}(t)$ remains near the invariant set. When necessary, the trajectory is perturbed by some small amount δ to increase the lifetime. By requiring $\|\delta\|$ to be small, the error introduced by the perturbation can be kept smaller than the error associated with the numerical integration. The resultant *pseudo-trajectory* can be continued in this fashion to arbitrary length (as illustrated in Fig B.1). The *Multi-stagger* technique provides some minor modification to the original algorithm of [13]. In this appendix, we explain how to execute the method, remark upon any differences from the standard Step-and- Stagger, and provide some justification for these modifications.

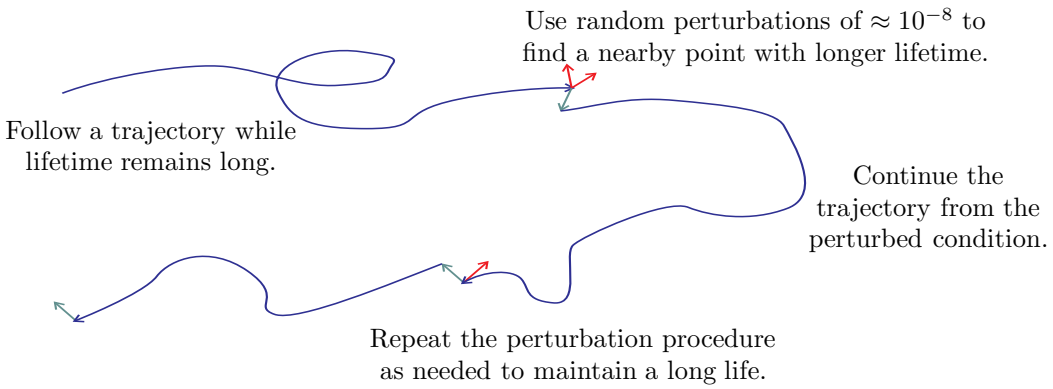

Figure B.1: **Schematic of a pseudo-trajectory.** A pseudo-trajectory is created by following system dynamics while the lifetime is above threshold. To keep a long lifetime, occasional perturbations are used to find nearby points with long life. An acceptable perturbation (green) is found by random search, rejecting perturbations that do not increase the lifetime (red).

B.1 Multi-stagger (with comparison to Step-and-Stagger)

Assume that we desire to generate a long trajectory near the chaotic saddle C of the system

$$\dot{\boldsymbol{x}} = F(\boldsymbol{x}), \tag{B.1}$$

with $\boldsymbol{x} \in \mathbb{R}^n$. Let S_C denote the stable set of the saddle, and assume that there is a suitable lifetime function L such that $L(\boldsymbol{x}) = \infty$ for all $\boldsymbol{x} \in S_C$. Let T^* be a *lifetime threshold*, such that if $L(\boldsymbol{x}) \geq T^*$ then $\boldsymbol{x}$ is assumed to be within some small distance ϵ of S_C.

A *pseudo-trajectory* $\Psi(t) \in$ will be defined on some time interval $[\alpha, \beta]$ such that on specified intervals (called *steps*), the pseudo-trajectory evolves in accordance with the flow of the system. Small adjustments (called *staggers*) are made between intervals as required to ensure that all points on the trajectory have a lifetime above threshold. Consequently, to store a pseudo-trajectory, it is sufficient to keep track of the initial condition and the time at the start of each step. Therefore, we associate $\Psi(t)$ with sequences $X = \{\boldsymbol{x}_i\}$ and $T = \{t_i\}$, composed of those initial conditions and times.

Assume that through some search technique we find an initial condition $\boldsymbol{x}_*$ with a lifetime greater than threshold. Since we want to use this point as the start of the step, we require

$$L(\boldsymbol{x}_*) \geq T^s := T^* + \Delta T, \tag{B.2}$$

where ΔT will prescribe a minimal length for the step.

Choosing ΔT. If we assume that a stagger will be of maximum size δ, then we can think of a stagger as creating a numerical error of bounded size. However, this error will be inserted at intervals not shorter than ΔT. If we assume that our numerical integration is accomplished with step size h, then the stagger error e_s is can be treated as an additional source of local truncation error, with

$$e_s \leq \frac{h\delta}{\Delta T}.$$

By choosing ΔT sufficiently large, we can ensure that e_s is not unacceptably large in comparison to the local truncation error from the numerical integration. [Note: [13] was written in the setting

of discrete time maps, and assumed $h = 1$. The algorithm did not address the concept of ΔT, but simply required that $L(\boldsymbol{x}_*) > T^*$ which is equivalent to assuming $\Delta T = 1$. For flows, there is no such natural assumption, and ΔT must be specifically chosen.]

Initiate the pseudo-trajectory. Assign $i = 1; \boldsymbol{x}_i := \boldsymbol{x}_*, t_1 = a$, creating the first entries in our sequences X and T.

Compute the step. Define ϕ^t to be the flow of the differential equation, and denote $L(\boldsymbol{x}_i) =: L_i$. We compute the step by evolving the trajectory of $\boldsymbol{x}_i$., assigning

$$t_{i+1} = t_i + (L_i - T^s),$$

and

$$\Psi(t) := \phi^t \boldsymbol{x}_i, \qquad t_i \leq t < t_{i+1}.$$

Finding a stagger. At time t_{i+1}, we want to start the next step from a point that is near where the last step ended, but with a lifetime that exceeds T^s. To find this initial condition, we conduct a random search as follows:

1. Assign $\boldsymbol{x}_b := \lim_{t \to t_{i+1}} \Psi(t)$, the base point, and $L_b := T*$, the lifetime at the basepoint.

2. Choose a random unit vector $\boldsymbol{v}$ that lies in the $n-1$ dimensional hyperplane perpendicular to the flow of (B.1) at $\boldsymbol{x}_b$. [Note: Because [13] dealt with maps, it place no restriction on the direction. However, perturbing the system along the direction of flow does not usefully extend the lifetime of the trajectory, since such a perturbation would be equivalent to integrating backward in time.]

3. Choose a perturbation magnitude μ from the *exponential stagger distribution,* described in [13] as follows: for $0 < \delta_m \ll \delta$, where δ was the previously defined maximum stagger size. Let a be such that $10^{-a} = \delta_m$, and choose random number s from a uniform distribution on the interval $[a, 15]$, (where 15 is chosen under the assumption that we are computing with 15-digit precision). Then assign $\mu := 10^s$ as the perturbation magnitude.

4. Compute $L(\boldsymbol{x}_b + \mu \boldsymbol{v}) = L_s$.

5. If $L_s \geq T^s$, then we have found a successful stagger; increment i, assign $\boldsymbol{x}_i := \boldsymbol{x}_b + \mu \boldsymbol{v}$, $L_i = L_s$, and compute the next step.

6. If $L_s \leq L_b$, then the perturbation showed no improvement in lifetime, so it is rejected. We search for new perturbation be returning to step 2.

7. If $L_s > L_b$, then lifetime has improved, but does not meet the threshold. However, we have moved in a direction of increasing lifetime, so we take advantage of that improvement by revising the basepoint for our search: $\boldsymbol{x}_b + \mu \boldsymbol{v} \mapsto \boldsymbol{x}_b$, and $L_b := L_s$. Continue the search by returning to step 2.

Figure B.2 illustrates the search technique

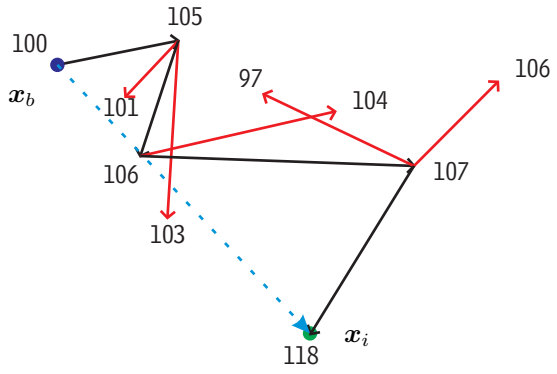

Figure B.2: **Multi-stagger**. From the initial basepoint (blue) with $L_s = 100$, we perturb the system to search for a point whose lifetime exceeds 110. Each perturbation is labeled with its lifetime. The black perturbations are accepted, while the red are rejected. The dashed arrow represents the resultant stagger.

The above algorithm captures the key new feature of *multistagger*. Step-and-Stagger follows a slightly different algorithm in that the perturbation is either accepted or rejected. In *multistagger*, by updating the basepoint whenever the lifetime is improved, we achieve some improvements on the performance. In application to the 9-variable model of plane Couette flow, the average stagger size was an order of magnitude smaller than when using Step-and-Stagger, while the number of test perturbations required was essentially unchanged. The smaller step size is the result of choosing

$\delta_1 = .01 * \delta$. If a stagger must be achieved in a single step, then δ must be chosen large enough to ensure that S_C can be reached. However, the exponential stagger distribution is specifically designed to favor small stagger sizes, because S_C is likely very close. Because *Multistagger* allows the search to take more than one step to reach S_C, we may place a smaller bound on the individual step size distribution. We note that the cumulative length of the step grows like $\sqrt{p}$, where p is the number of perturbations that increase lifetime but do not achieve the threshold value T^s. Consequently, although the total stagger size can grow arbitrarily large, it is not likely, in practice, to exceed δ until the area of small perturbations has been thoroughly searched.

In [18], a gradient ascent technique was used to determine an appropriate search direction. However, for higher dimensional systems with robust transient behavior, the computational cost of computing the gradient might easily exceed the cost associated with unsuccessful staggers. Additionally, the highly fractal structure that may exist even at machine precision scales may preclude an accurate estimate of a gradient. In application to the 9-variable model, we generally required approximately ten perturbation before achieving a successful stagger, whereas the gradient would require 18 lifetime evaluations before any searches are conducted. We note (to the disadvantage of both techniques) that a gradient ascent and the random search of *Mutlistagger* may become trapped in local maxima of lifetime function.

Appendix C

Relationship between methods for computing the dimension of the stable set

In [15], the authors consider an N-dimensional system with a chaotic saddle. If the transient behavior is sufficiently robust that a general line through phase space intersects the saddle set, then D_s, the dimension of the stable set, can be computed from the relationship

$$N - D_s = (\tau \lambda_1)^{-1}, \tag{C.1}$$

where τ is the decay time and λ_1 is the largest Lyapunov exponent. This formulation is numerically very easy to implement, because the leading Lyapunov exponent is easily estimated by computing the divergence rate of two nearby, transient trajectories. In [14], the authors use a different

approach to develop a procedure for determining the dimension of the saddle and its stable and unstable sets using a formulation that is similar to the Kaplan-Yorke dimension for chaotic attractors. The technique requires the full spectrum of Lyapunov exponents (and is therefore, more difficult) but it provides the additional information of the dimension of the saddle and its unstable set. In this appendix, we show the algebraic equivalence of the two methods in computing D_s, under the condition that a line generically intersects the stable set.

First, we start with a brief overview of how the D_s is computed from the spectrum of Lyapunov exponents, which we will refer to as the *KY method.* Because this equivalence of the formulations is algebraic, it is not dependent upon an explanation of the derivations. Therefore, the steps below outline only the required computations to *apply* the KY method.

- Assume the a saddle trajectory has U Lyapunov exponents that are positive, and $S = N - U$ exponents that are non-negative. Then order and label the positive exponents as

$$h_U \geq h_{U-1} \geq \cdots \geq h_1 > 0.$$

- Compute a metric entropy on the invariant set,

$$H := -1/\tau + \sum_{i}^{U} h_i,$$

  where τ is the decay time for the saddle.

- Compute the index J such that

$$h_1 + \cdots + h_{J+1} \geq H \geq h_1 + \cdots + h_J. \tag{C.2}$$

- Then compute D_s by

$$D_s = S + J + \frac{H - h_1 + \cdots + h_J}{h_{J+1}}. \tag{C.3}$$

Demonstrating equivalence. The formulation of (C.1) is based on the assumption that a line through phase space intersects the saddle set, from which we infer that $N > D_s > N - 1$. Consequently, $N - D_s < 1$, which implies from (C.1) that

$$1/\tau < \lambda_1, \tag{C.4}$$

where $\lambda_1 \equiv h_U$ is the largest Lyapunov exponent. From (C.4), we infer that $J = U - 1$ as follows: To satisfy (C.2), we see trivially that $H < \sum_i^U h_i$, but we also require

$$H \geq h_1 + \cdots + h_J,$$

or equivalently,

$$H - h_1 - \cdots - h_J \geq 0.$$

If $J = U - 1$, then

$$H - h_1 - \cdots - h_{U-1} = -1/\tau + h_U > 0,$$

where the right side inequality is given by (C.4). Applying $J = U - 1$ to (C.3) yields

$$D_s = S + U - 1 + \frac{-1/\tau + h_U}{h_U}.$$

Recalling that $S + U = N$ and applying simple algebraic rearrangement, we see that

$$N - D_s = \frac{1}{\tau h_U} \equiv (\tau \lambda_1)^{-1}. \qquad \square$$

Appendix D

Proof that the stable set is unbounded.

Theorem D.1. *Given a dynamical system $\dot{\boldsymbol{x}} = F(\boldsymbol{x})$, with a chaotic saddle C. If the system is dissipative then C^s, the stable set of C is unbounded.*

Proof: Let L be a suitable lifetime function for C. For any $t > 0$, define a one parameter family of sets C^t defined by

$$C^t := \{\boldsymbol{x} | L(\boldsymbol{x}) \geq t\}.$$

C^t is the set of points whose lifetime exceeds t. As we increase t, there will be fewer points that meet that threshold value of lifetime, so the set should get smaller:

Take $t_1 > t_2 > 0$. Then $C^{t_1} \subset C^{t_2}$, and

$$m(C^{t_1}) \leq m(C^{t_2}), \tag{D.1}$$

where $m(A)$ is the Lebesgue measure of set A.

Let ϕ^t describe the flow of the dynamical system, parameterized over t. If we take the set of points whose lifetime exceeds t_1, and evolve if forward in time by some amount ΔT, we reduce the lifetime of all those points, and we will end up with a set of points, all of which have a lifetime that exceeds $t_1 - \Delta T$. Therefore

$$\phi^{t_1 - t_2}[C^{t_1}] = C^{t_2}.$$

Because the system is dissipative, as we evolve a set forward in time, its volume is decreasing, so

$$m(C^{t_2}) \leq m(C^{t_1}), \tag{D.2}$$

with equality only if both sets are measure 0 or both sets have infinite measure. From (D.1) and (D.2), we conclude that

$$m(C^{t_2}) = m(C^{t_1}).$$

By continuity of the lifetime function, we know that C^t must have positive measure, so the only way to satisfy the above equality is if $m(C^{t_2}) = m(C^{t_1}) = \infty$. But t_2 is arbitrary, so C^t must have infinite measure for all t, and is therefore unbounded. Since $\lim_{t\to\infty} C^t = C^s$, we see that C_s must also be unbounded. □

Appendix E

Proof that the decay constant τ is independent of the random sampling distribution.

For systems with a chaotic transients (and chaotic saddles), the transient lifetime of initial conditions typically have an exponential distribution [32]. The usual description of this behavior is that if initial conditions are sampled uniformly on some set, then lifetimes will be exponentially distributed. We show that the sample measure need not be uniform, but can be relaxed to absolutely continuous. Consequently, almost any random sampling routine will yield the same asymptotic value for decay rate.

E.1 Background

In the literature, the standard description for the exponential decay of lifetimes in a chaotic saddle proceeds as follows:

> Sprinkle $N(0)$ initial conditions uniformly on a compact region W of phase space, where W contains the non-attracting set. Let $N(t)$ be the number of initial conditions whose lifetime exceeds t. Then $N(t) \sim \exp(-t/\tau)$ for large t.

τ is sometimes called the "average lifetime." However, one would expect τ to be the average lifetime only when the distribution of lifetimes is a true exponential, which generally is not the case. A more appropriate term, such as is used in [14], is that τ is the "decay time," which more closely fits the more formal definition of τ :

$$\frac{1}{\tau} = \lim_{t\to\infty} \lim_{N(0)\to\infty} \frac{-\ln(N(t)/N(0))}{t}, \tag{E.1}$$

with the definition clearly indicating that the exponential decay is an asymptotic behavior. We will show that with some mild constraints, (E.1) does not depend upon either the particular distribution used to sample or upon the sampled set.

E.2 The lifetime function

Throughout this Appendix, assume that we are using a lifetime function $L(x)$ that is suitable for measuring the chaotic transients. By "suitable," we mean that the lifetime function should satisfy:

1. $L : X \to \mathbb{R}$, where the dynamical system is defined on X.
2. $L(x) = \infty$ iff x is on the stable set of the saddle, denoted C.
3. For every $y \in C$, $\lim_{x\to y} L(x) = \infty$.
4. Let ϕ^t be the flow operator of the system, then $L(\phi^t x) = \max(L(x) - t, 0)$.
5. $L(x)$ should be semi-continuous at each x for which $L(x)$ is finite. [Note: This particular proof requires only the L be measurable. However, it seems reasonable to require that nearby

points should have approximately the same lifetime. Although it might be nice if L were continuous, much of the literature does not yield a continuous lifetime function. Consider the following simple example: Place an epsilon ball as the lifetime boundary around an asymptotically stable fixed point. Assume that the system is such that $V(x) = \|x\|^2$ is not a Lyapunov function. Then there will be a trajectory that is tangent to the epsilon ball at time $t*$, but lies outside the ball for some time $t_1 < t*$ and for some $t_2 > t*$. Call this a grazing trajectory. Then in any neighborhood $N(t)$ of the grazing trajectory, there will be a finite separation between the lifetime of nearby points that enter the epsilon ball at approximately time $t*$, and those that enter the ball at some time later in the trajectory's decay. Because the ϵ-*ball* definition of lifetime is so often used in the literature, we desire not to exclude it from our definition.]

6. $L(x) \geq 0$.

7. $L(x) = 0$ on any attractor of the system.

E.3 Definitions

This list of definitions is to provide some common terminology and symbology for the discussion.

Saddle set: The set of all points whose trajectories asymptotically approach the chaotic saddle, denoted by C.

Test Set: W is a *test set* if (a) it is compact set amd (b) for some point $x \in C$, there is a neighborhood $N(x)$ of positive Lebesgue measure with $N(x) \subset W$.

Lifetime function: Denoted by L. Assume that it is suitable.

^{t} notation: For a test set W, define $W^t = \{x \in W | L(x) \geq t\}$. We remark that (a) $\overline{W^t}$ is also a test set, and (b) W^t must contain an open neighborhood of each point in $C \cap W$. Figure E.1 provides an illustration of this family of sets.

Exponential distribution of lifetimes (EDL_μ) : Let $M_\mu(t) := \int_{B^t} \mu(x)\mathrm{d}x$, where μ is a measure that is absolutely continuous with respect to Lebesgue measure. Given a test set W, if there is a positive constant τ such that

$$\lim_{t\to\infty} \frac{\frac{\mathrm{d}}{\mathrm{d}t}\left(M_\mu(t)\right)}{M_\mu(t)} = -1/\tau, \tag{E.2}$$

for all test sets $B \subset W$, then we say that the saddle set is EDL_μ on W.

m notation: $m(A) = \int_A \mathrm{d}x$ denotes the normal Lebesgue measure in $\mathbb{R}^n$.

Diameter of set A: The diameter of a set A [notation $d(A)$] is defined by

$$d(A) := \max_{\substack{x\in A\\ y\in A}} \|x - y\|.$$

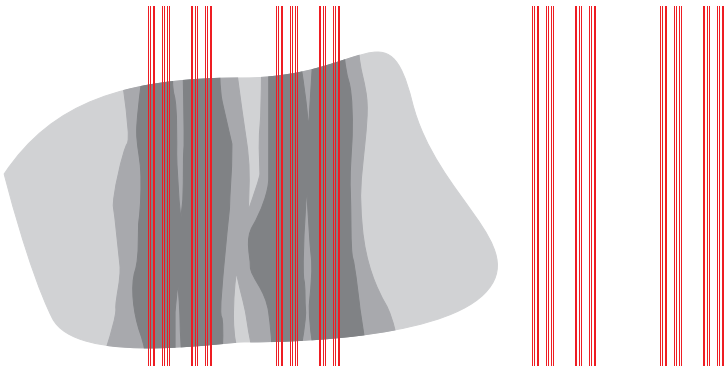

Figure E.1: **Illustration of W^t.** The measure 0 set C is colored in red. The light gray indicates a test set W. The graduated gray colorings indicate W^t for increasing t. W^t converges to the stable set of the saddle as $t \to \infty$.

E.4 The proof

Claim: If saddle set C is EDL_μ on W when $\mu(x) \equiv 1$, then it is EDL_μ on W for $\mu(x)$ satisfying:

- $\mu(x)$ absolutely continuous,
- $0 < b \leq \mu(x) \leq M \quad \forall x \in W$.

Moreover, τ defined by (E.2) does not depend on μ. We call the invariant constant τ the *decay time.*

Outline of Proof:

1. (Lemma 1) Show that the claim holds for any sufficiently small test set $B \subset W$.
2. (Lemma 2) Show that for arbitrary test set A, there is a T such that the set A^T can be partitioned into a finite union of test sets that are sufficiently small to satisfy step 1 above.
3. Show that Lemma 1 and 2 imply the claim.

Lemma 1: There exists $\epsilon > 0$ such that if test set B satisfies $d(B) \leq \epsilon$, then C is EDL_μ on B, and τ does not depend on μ.

Proof of Lemma 1. Denote set $B_\Delta := B^t - B^{t+\Delta t}$. Then we can rewrite the definition of EDL as

$$\lim_{t\to\infty}\lim_{\Delta t\to 0}\frac{\int_{B_\Delta}\mu(x)\mathrm{d}x}{\Delta t\int_{B^t}\mu(x)\mathrm{d}x} = 1/\tau, \tag{E.3}$$

which by the main hypothesis, holds for $\mu(x) \equiv 1$. So given any $\gamma > 0$, there exist $t_B, \Delta t_B$, such that

$$1/\tau - \gamma \leq \frac{m(B_\Delta)}{\Delta t m(B^t)} \leq 1/\tau + \gamma \quad \forall t > t_B, \Delta t < \Delta t_B. \tag{E.4}$$

Now consider some arbitrary measure μ (satisfying the main hypothesis). Denote

$$\mu_{max} = \max_{x\in B}\mu(x); \quad \mu_{min} = \min_{x\in B}\mu(x).$$

Then

$$\mu_{min}m(B_\Delta) \leq \int_{B_\Delta}\mu(x)\mathrm{d}x \leq \mu_{max}m(B_\Delta),$$

and

$$\mu_{min}m(B^t) \leq \int_{B^t}\mu(x)\mathrm{d}x \leq \mu_{max}m(B^t).$$

By using extreme values for the numerator and denominator of the left hand side of (E.3) and the inequality of (E.4), we have

$$\frac{\mu_{min}}{\mu_{max}}(1/\tau-\gamma) \leq \frac{\mu_{min}}{\mu_{max}}\frac{m(B_\Delta)}{\Delta t m(B^t)} \leq \frac{\int_{B_\Delta}\mu(x)\mathrm{d}x}{\Delta t\int_{B^t}\mu(x)\mathrm{d}x} \leq \frac{\mu_{max}}{\mu_{min}}\frac{m(B_\Delta)}{\Delta t m(B^t)} \leq \frac{\mu_{max}}{\mu_{min}}(1/\tau+\gamma). \tag{E.5}$$

WLOG, if we assume $\mu(x) > \mu(y)$, we note that

$$\frac{\mu(x)}{\mu(y)} = \frac{\mu(y) + \mu(x) - \mu(y)}{\mu(y)} = 1 + \frac{\mu(x) - \mu(y)}{\mu(y)} \leq 1 + \frac{\mu(x) - \mu(y)}{b}$$

Because absolute continuity implies uniform continuity of μ, we can choose an ϵ such that $\mu(x) - \mu(y)$ is arbitrarily small whenever $|x - y| \leq \epsilon$ for all x and y in W. So we can choose an ϵ that does not depend on B such that the ratio $\frac{\mu_{max}}{\mu_{min}}$ is arbitrarily close to 1 : in other words, for arbitrarily small r, we can find an ϵ such that

$$1 - r \leq \frac{\mu(y)}{\mu(x)} \leq \frac{\mu(x)}{\mu(y)} < 1 + r.$$

Then

$$(1 - r)(1/\tau - \gamma) \leq \frac{\int_{B_\Delta} \mu(x) \mathrm{d}x}{\Delta t \int_{B^t} \mu(x) \mathrm{d}x} \leq (1 + r)(1/\tau + \gamma). \tag{E.6}$$

Since γ and r can be chosen arbitrarily small, the above inequality proves lemma 1.□

Lemma 2: For any test set A, there exists T such that A^T can be partitioned into sets α_i, where

$$A^T = \bigcup_{i=1}^{n} \alpha_i,$$

and for each i, $\overline{\alpha_i}$ is a test set with $d(\overline{\alpha_i}) \leq \epsilon$.

Proof of Lemma 2. Consider the set $C_A := C \cap A$; place an open ball of diameter $\epsilon/2$ around each point in C_A. Denote the union of these balls by $C_{\epsilon/2}$. Then the set $A - C_{\epsilon/2}$ is compact and contains no points from the saddle set. Therefore the lifetime is bounded on that set, with a least upper bound which we denote T. The closure of A^T must lie in the closure of $C_{\epsilon/2}$, If we place an open ball of diameter ϵ around each point of C_A, we have an open covering of $\overline{A^T}$. (See Fig E.2.) Because $\overline{A^T}$ is compact, we can extract a finite subcover, which we denote by $\{B(b_i)\}_{i=1}^n$. We now partition

$$A^T = \bigcup_{i=1}^{n} \alpha_i,$$

by requiring (a) each α_i contain a positive measure neighborhood of b_i, and (b) α_i can contain only those points in A^T that are in $B(b_i)$. By construction, $d(\overline{\alpha_i}) \leq \epsilon$ and is also a test set, which completes the proof of Lemma 2. □

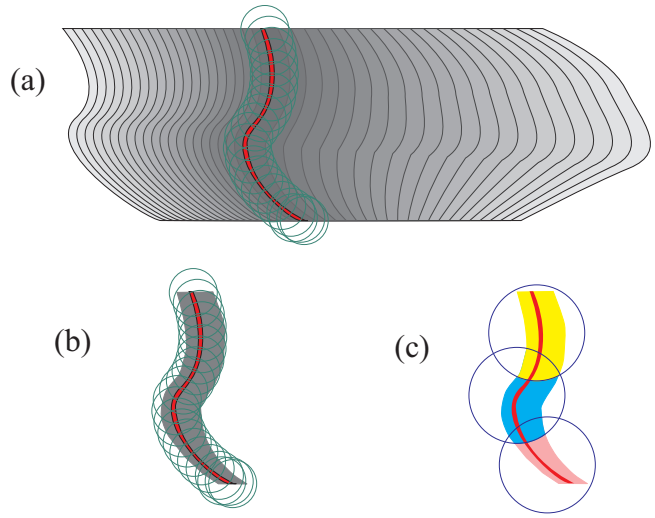

Figure E.2: **Lemma 2: constructing a partition** (a) The test set A (gray) is colored with increasing lifetime. By covering C (red) with balls of diameter $\epsilon/2$, (b) we can determine a value T such that $\overline{A^T}$ is inside the closure of the union of balls. (c) We use a finite covering of open balls of diameter ϵ to construct a partition of A^T.

Step 3 — Completing the main proof. From Lemma 1, we know that there is an ϵ such that any test set in W with diameter less than ϵ has decay time τ independent of the choice of μ. Consequently, each α_i has an exponential decay rate $1/\tau$ which is independent of μ :

$$\lim_{t\to\infty} \frac{\frac{\mathrm{d}}{\mathrm{d}t}\int_{\alpha_i^t}\mu(x)\mathrm{d}x}{\int_{\alpha_i^t}\mu(x)\mathrm{d}x} = -1/\tau \qquad \forall i.$$

Then given and small $\beta > 0$, there is a N such that for all i and all $t > N > T$,

$$(-1/\tau-\beta)\int_{\alpha_i^t}\mu(x)\mathrm{d}x \le \frac{\mathrm{d}}{\mathrm{d}t}\int_{\alpha_i^t}\mu(x)\mathrm{d}x \le (-1/\tau+\beta)\int_{\alpha_i^t}\mu(x)\mathrm{d}x.$$

Taking the finite sum over i (passing through the derivative in the middle term) gives

$$(-1/\tau-\beta)\int_{(A^T)^t}\mu(x)\mathrm{d}x \le \frac{\mathrm{d}}{\mathrm{d}t}\int_{(A^T)^t}\mu(x)\mathrm{d}x \le (-1/\tau+\beta)\int_{(A^T)^t}\mu(x)\mathrm{d}x.$$

Dividing through by $\int_{(A^T)^t}\mu(x)\mathrm{d}x$, we can conclude that

$$\lim_{t\to\infty} \frac{\frac{\mathrm{d}}{\mathrm{d}t}\int_{(A^T)^t}\mu(x)\mathrm{d}x}{\int_{(A^T)^t}\mu(x)\mathrm{d}x} = -1/\tau.$$

We note that for $t > T$, $A^t \equiv (A^T)^t$, which completes the proof. □

BIBLIOGRAPHY

[1] O Reynolds. An experimental investigation of the circumstances which determine whether the motion of water shall be direct or sinuous and the law of resistance in parallel channels. *Phil. Trans. R. Soc.*, 174:935–982, 1883.

[2] P. J. Schmid and D. S. Henningson. *Stability and transition in shear flows.* Springer-Verlag, New York, 2000.

[3] Bruno Eckhardt and H. Faisst. Dynamical systems and transition to turbulence. In R.R. Kerswell and T. Mullin, editors, *Proceedings IUTAM Symposium Bristol 2004*. Kluwer, 2005. In press.

[4] Armin Schmiegel and Bruno Eckhardt. Fractal stability border in plane Couette flow. *Phys. Rev. Let.*, 79:5250–5253, 2000.

[5] Bruno Eckhardt and A. Mersmann. Transition to turbulence in a shear flow. *Phys. Rev. E*, 60:509–517, 1999.

[6] J. Moehlis, H. Faisst, and Bruno Eckhardt. A low-dimensional model for turbulent shear flows. *New J. Phys.*, 6(1):56, 2004.

[7] H. Faisst and Bruno Eckhardt. Sensitive dependence on initial conditions in transition to turbulence in pipe flow. *J. Fluid. Mech.*, 504:343–352, 2004.

[8] S. Bottin and H. Chaté. Statistical analysis of the transition to turbulence in plane Couette flow. *Eur. Phys J. B.*, 6:143–155, 1998.

[9] S. Bottin, F. Daviaud, P. Manneville, and O. Dauchot. Discontinuous transition to spatiotemporal intermittency in plane Couette flow. *Europhys. Lett.*, 43(2):171–176, 1998.

[10] Armin Schmiegel. *Transition to turbulence in linearly stable shear flows.* PhD dissertation, Philipps-Universität Marburg, Marburg, Germany, 1999.

[11] J. Moehlis, T. Smith, P. Holmes, and H. Faisst. Models for turbulent plane couette flow using the proper orthogonal decomposition. *Phys Fluids*, 14:7, 2002.

[12] O. Dauchot and N. Vioujard. Phase space analysis of a dynamical model for the subcritical transition to turbulence in plane Couette flow. *Eur. Phys. J. B*, 14, 2000.

[13] D. Sweet, Helena E. Nusse, and James A. Yorke. Stagger-and-Step method: Detecting and computing chaotic saddles in higher dimensions. *Phys. Rev. Let.*, 86(11):2261–2264, 2001.

[14] Brian R. Hunt, Edward Ott, and James A. Yorke. Fractal dimension of chaotic saddles of dynamical systems. *Phys. Rev. E*, 54(5):4819–4823, 1996.

[15] Y. Lai and R. L. Winslow. Geometric properties of the chaotic saddle for supertransients in spatiotemporal chaotic systems. *Phys. Rev. Let.*, 74(26):5208–5211, 1995.

[16] Joseph D. Skufca, James A. Yorke, and Bruno Eckhardt. The chaotic saddle in a model of plane Couette flow. unpublished, 2005.

[17] C. Grebogi, Edward Ott, and James A. Yorke. Metamorphoses of basin boundaries in nonlinear dynamical systems. *Phys. Rev. Let.*, 56:1011–1014, 1986.

[18] Erik Bollt. The path towards a longer life: On invariant sets and the escape time landscape. *Int J. Bif Chaos*, 15(5), 2005. To appear.

[19] Helena E. Nusse and James A. Yorke. A procedure for finding numerical trajectories on chaotic saddles. *Physica D*, 36:137–156, 1989.

[20] J. S. Baggett and L. N. Trefethen. Low-dimensional models of subcritical transition to turbulence. *Phys Fluids*, 9(4):1043–1053, 1997.

[21] C. David Andereck, S. S. Liu, and Harry L. Swinney. Flow regimes in a circular Couette system with independently rotating cylinders. *J. Fluid Mech.*, 164:155–183, 1986.

[22] H. Kantz and P. Grassberger. Repellers, semi-attractors, and long-lived chaotic transients. *Physica D*, 17(1):75–86, 1985.

[23] S. M. Hammel, James A. Yorke, and C. Grebogi. Do numerical orbits of chaotic dynamical processes represent true orbits? *J. Complexity*, 3(36):136–145, 1987.

[24] J.-P. Eckmann and D. Ruelle. Ergodic theory of chaos and strange attractors. *Rev. Mod. Phys.*, 57(3):617–656, 1985.

[25] Pablo Moresco and Silvina Ponce Dawson. The PIM-simplex method: an extension of the PIM-triple method to saddles with an arbitrary number of expanding directions. *Physica D*, 126:33–48, 1999.

[26] Silvina Dawson, Celso Grebogi, Tim Sauer, and James A. Yorke. Obstructions to shadowing when a lyapunov exponent fluctuates about zero. *Phys. Rev. Lett.*, 73(14):1927–1930, 1994.

[27] Tim Sauer, Celso Grebogi, and James A. Yorke. How long do numerical chaotic solutions remain valid? *Phys. Rev. Lett.*, 79(1):59–62, 1997.

[28] J. Moehlis, H. Faisst, and Bruno Eckhardt. Periodic orbits and chaotic sets in a low-dimensional model for shear flows. *SIAM J. of Applied Dynamical Systems*, 5(2):352–376, 2005.

[29] Mukeshwar Dhamala and Ying-Chen Lai. The natural measure of nonattracting chaotic sets and its representation by unstable periodic orbits. *Int. J. Bif. and Chaos*, 12(12):2991–3005, 2002.

[30] S. Smale. Differentiable dynamical systems. *Bull. Amer. Math. Soc.*, 73:747–817, 1967.

[31] C. Grebogi, Ed Ott, and James A. Yorke. Fractal basin boundaries, long-lived chaotic transients, and unstable-unstable pair bifurcations. *Phys. Rev. Lett.*, 50:935–938, 1983.

[32] Edward Ott. *Chaos in Dynamical Systems*. Cambridge University Press, Cambridge, UK, second edition, 2002.

[33] Steven W. McDonald, Celso Grebogi, Edward Ott, and James A. Yorke. Fractal basin boundaries. *Physica D*, 17(2):125–153, 1985.

[34] Edward N. Lorenz and K. A. Emanuel. Optimal sites for supplementary weather observations: Simulation with a small model. *J. of Atmos. Sci.*, 55(3):399–414, 1998.

[35] M. Behzad, G. Chartrand, and L. Lesniak-Foster. *Graphs and Digraphs.* Prindle, Weber & Schmidt, Boston, Massachusetts, second edition, 1979.